Interfacial Thermodynamics of Coexisting Aqueous Polymer Solutions

Cover: artist's impression of a phase-separated aqueous polymer mixture (back) close to and (front) far from the critical point.
Printed by: Gildeprint.
ISBN: 978-90-393-6438-3.

Interfacial Thermodynamics of Coexisting Aqueous Polymer Solutions

Thermodynamica van het Grensvlak tussen
Coëxisterende Waterige Polymeeroplossingen

(met een samenvatting in het Nederlands)

Proefschrift

ter verkrijging van de graad van doctor aan de Universiteit Utrecht op gezag van de rector magnificus, prof. dr. G. J. van der Zwaan, ingevolge het besluit van het college voor promoties in het openbaar te verdedigen op maandag 23 november 2015 des middags te 2.30 uur

door

Mark Vis

geboren op 28 juni 1988 te Zeist

Promotor:	Prof. dr. A. P. Philipse
Copromotoren:	Dr. B. H. Erné
	Dr. R. H. Tromp

Het in dit proefschrift beschreven onderzoek werd gefinancierd door het gebied chemische wetenschappen (CW) van de Nederlandse Organisatie voor Wetenschappelijk Onderzoek (NWO).

Contents

Preface

The first time I was introduced to the topic of phase separation in aqueous polymer mixtures was during a group meeting on Monday, October 18 in 2010. I was at the Van 't Hoff Laboratory for Physical and Colloid Chemistry (FCC) at Utrecht University, working as a master student with Dzina Kleshchanok and Henk Lekkerkerker. This particular group meeting featured a presentation by Ben Erné, in which he described a grant proposal for a PhD project by Hans Tromp and himself to study the physics of water-in-water Pickering emulsions. I found the little physics I understood about water–water interfaces quite fascinating, but doing PhD research still seemed very far away, and besides, it was not even certain whether the project would receive funding. Therefore, in the end, I did not discuss the project with him.

After finishing my master's thesis, I started an internship at the University of Gothenburg in Sweden in April 2011. A few weeks later, on May 10, I was surprised to receive an email from Ben, telling me he was recently awarded a grant for a PhD project and asking me whether I would be interested. This was, indeed, the grant he talked about in his presentation many months before. To convince myself that this was the most suitable PhD project for me, I spent a number of weeks looking for PhD projects that would be even more interesting, but quickly found this to be impossible. I started my PhD project with Ben as my daily supervisor, Hans as my co-supervisor, and Albert Philipse as my promotor on January 1, 2012. Nearly four years later, I am writing this preface.

I would like to take this opportunity to thank everyone who contributed in scientific and/or nonscientific ways to the realization of this thesis. Ben, thank you for the opportunity of doing my PhD work with you. I greatly appreciated our weekly meetings and impromptu discussions, and I learned a lot from your meticulous feedback on my manuscripts, (often lengthy) reports, abstracts, and presentations. Hans, thank you for co-supervising me. With your extensive experience with mixtures

of dextran and gelatin you provided many useful ideas. Albert, thank you for being my promotor and for valuable discussions.

Edgar, your introduction to the blob model sparked my theoretical investigations on water–water phase separation and resulted in substantial parts of this thesis. Thank you for all your help; it was a pleasure to collaborate with you. Henk, I enjoyed your continued interest and involvement in my PhD project. Your ideas contributed substantially to Chapter 4. Giuseppe, your numerical calculations on the adsorption of platelets and spheres at liquid–liquid interfaces constitute a major component of Chapter 5. Many thanks, also to René, for your effort and our discussions. Elleke, the large gibbsite platelets that you provided made the optical investigations of the emulsions in Chapter 5 a lot easier. Thank you!

I was fortunate to supervise many students during my PhD work. In their research project, Adriaan, Jarich, Joanna, and Joren together performed early measurements on the tension of the water–water interface and experimented with ways to measure phase diagrams and to prepare emulsions. Ingo prepared and studied a multitude of different types of particles to find optimal emulsion stabilization, while Joeri focused on the physics of the stabilization. Vincent put significant effort in systematic measurements of the interfacial tension and of phase diagrams. Explorative work of Stijn showed that effects predicted by theory and seen in aqueous mixtures of dextran and gelatin also occurred in other systems, although quantitative characterization in these other systems turned out to be not so straightforward. A completely different topic was investigated by Kristian, who performed electrical impedance spectroscopy on the oil–water interface; we learned that similar measurements on the water–water interface would be even more challenging. Thank you all!

There are many people at the lab who have contributed positively to my time here and provided an excellent atmosphere. Roel, I am grateful that you took the time to proofread my thesis and that I could always walk into your office to discuss a random typographical issue with you. I also enjoyed our visits to many concerts and hope that many more will follow; though next time maybe I should safeguard your car key. Jos, thanks for your help on various subjects, including Mathematica. Jasper, thanks for your feedback on what might have been the most difficult part of my PhD project: the selection of proper fonts for this thesis. I would like to thank Roel, Jos, and Jasper additionally for many discussions about LaTeX. I would also like to thank everyone else who was at FCC during my time, including Andrei, Anke, Antara, Bas, Bob, Burak, Chris, Dima, Dzina, Esther, Fuqiang, Gert Jan, Ivan, Jaakko, Jan Groenewold, Jan Hilhorst, Janne-Mieke, Joost, Julius, Laura, Mikal, Nina, Pepijn, Ping, Remco, Rob, Rocío, Samia, Sonja, Susanne, prof. Vrij, Willem, Yong, and of course all students for the cookies, cakes, drinks, and discussions. I would like to thank Bonny, Dominique,

Emile, Kanvaly, Marina, and Stephan for their technical and administrative support.

Many dear friends have supported me in the past years, some of whom I have already mentioned. Aldo & Thijs, thanks for being my paranymphs! Aldo, thanks for being my partner in crime in the Scheikundejongens. Although writing on our blog took a back seat lately, we still did quite some interesting things and I look forward to expanding our efforts in the future. Thijs, sharing a flat with you was great fun and I hope that we will encounter many more "frydays"! Frank, thanks for being a loyal friend already for such a long time, even while we were on opposite sites of the globe, and for taking the time to proofread my thesis. Freddy, thanks for correcting some "serious" errors in my thesis! Hedwich & Robbert, Paul & Erwin, Dominique, Inge, Nadine, and everyone else: thanks for being friends both in happy and slightly more unhappy times.

I would also like to thank my family and those who—strictly speaking—are not family, but definitely feel that way. In particular I would like to thank my parents for their encouragement throughout the years and for their interest in my work, even though it was sometimes hard to explain what I was actually doing. Hanneke & Stef, thanks for your support, always being so welcoming, and undertaking many fun activities together with the other members of "Hotel Parkzicht"; I'm already looking forward to our next camping trip! Maartje, thanks for your love, understanding, and support.

Mark Vis
October 7, 2015
Zeist

CHAPTER 1

Introduction

Martinus Willem Beijerinck noted in 1896 that mixing an aqueous solution of soluble starch with an aqueous solution of gelatin did not result in a homogeneous mixture [1]. Instead, an emulsion was formed, which consisted of aqueous droplets rich in gelatin suspended in an aqueous continuous phase rich in starch. The gelatin-rich droplets in turn contained a large quantity of starch-rich droplets, which were so small that Beijerinck could visualize them only through the addition of iodine, which forms a dark blue complex with starch. At increased gelatin concentrations, the gelatin-rich droplets became so big that they almost touched. Beijerinck, a microbiologist and botanist, found the structure to resemble "artificial cellular tissue," with starch-rich "walls" separating gelatin-rich "cells." At even higher gelatin concentrations, the situation was reversed: starch-rich droplets were suspended in a gelatin-rich continuous phase. Vigorous shaking or stirring was found to reduce the size of the emulsion droplets, whereas prolonged standing resulted in the formation of two macroscopic phases, one rich in starch and one rich in gelatin. Beijerinck stated that he did not observe phase separation in other mixtures, such as gelatin in combination with dextrin or with inulin, and concluded that the incompatibility of starch and gelatin originates from "a specific property of starch in relation to gelatin" [1].

In hindsight, the observations of Beijerinck are not due to a specific interaction between starch and gelatin, but they have to do with the macromolecular nature of both [2]. The high degree of polymerization of the (bio)polymers starch and gelatin leads to many solvent–polymer and polymer–polymer contacts per polymer chain.

While the contacts between polymer and solvent are favorable in case of a good solvent, the contacts between the two different polymers are generally unfavorable. As a result, the mixing enthalpy of two different polymers is often positive and cannot be compensated by the mixing entropy. As the number of polymer–polymer contacts and consequently the mixing enthalpy depends strongly on polymer concentration, phase separation is observed only above a critical demixing concentration.

The critical demixing concentration depends not only on the specific combination of two polymers, but also on their molar masses. Upon increase of the molar masses, the mixing entropy decreases with respect to the mixing enthalpy, so demixing occurs already at lower concentrations. The reason that Beijerinck did not observe phase separation in his additional experiments on gelatin with dextrin or inulin is because the last two biopolymers are polysaccharides with a low molar mass: high molar mass dextran is indeed well-known to phase separate from gelatin in aqueous solution [3–6].

The phase separation of two polymers in aqueous solution such as described by Beijerinck is now often called water–water phase separation and such systems are generally named aqueous two-phase systems (ATPS) or aqueous biphasic systems (ABS). Many of such systems exist, such as poly(ethylene oxide)–dextran [7–9], dextran–gelatin [3–6], alginate–caseinate [10], polystyrenesulfonate–poly(acrylic acid) [11], dextran–methylcellulose [12], and various (other) combinations of protein and polysaccharide [13–15]. In these examples, phase separation takes place when the total mass fraction of polymer is well below 10 %. Additionally, the phase separation is segregative: each phase is enriched in one of the polymers. Associative phase separation [16, 17], where one phase is enriched in both polymers, is often found under poor or marginal solvent conditions, or for attractive polymer–polymer interactions, as in the case of complex coacervation. This was already recognized by Bungenberg de Jong and Kruyt in 1929, who suggested that complex coacervation was driven by the attractive interactions between oppositely charged polyelectrolytes [18].

Aqueous two-phase systems have also received attention from an applied perspective. Albertsson rediscovered these systems in 1958 for the separation and purification of sensitive compounds such as proteins [12]. The relatively subtle differences in composition of the two phases allow, e.g., proteins to be separated on similarly subtle differences in their composition, hydrophobicity, and other properties. Another interesting potential application of aqueous two-phase systems is the preparation of water-in-water emulsions [19], which may potentially be used to replace traditional water-in-oil or oil-in-water emulsions commonly encountered in food or as a way to encapsulate sensitive material such as proteins or cells. Well-defined water-in-water droplets can be prepared using microfluidics [20–22], although the formation of the droplets is still not quite well understood [23] and they eventually coalesce, unless

stabilized by cross-linking [24]. Because the properties of the water–water interface are distinctly different from those of oil–water interfaces, it is necessary to study in detail the physics of the interface and of phase separation in order to understand fully how to stabilize water-in-water emulsions.

The peculiar properties of water–water interfaces originate from the fact that both phases typically consist for 90 % of water. These liquid–liquid interfaces have a width of the order of 10 nm [25, 26], have an ultralow tension—typically of the order of a μN/m [7, 27–32]—and are permeable to solvent and small ions. The width of the interface means that typical surfactant molecules are unable to stabilize water-in-water emulsions, simply because they are too small to span the interface. Another possibility for stabilizing emulsions is through the adsorption of colloidal particles at the liquid–liquid interface, known as Pickering stabilization [33, 34]. This too is difficult for water–water interfaces, because the ultralow interfacial tension makes the adsorption energies much smaller than for particles at oil–water interfaces. The adsorption energy can be increased by using larger colloidal particles, but this may have other unwanted effects, such as accelerated sedimentation of emulsion droplets.

The permeability of water–water interfaces to ions may lead to the formation of an interfacial electric potential difference, for instance when salts composed of cations and anions with different partitioning coefficients are introduced [35–38]. A similar effect is observed when one of the polymers carries a charge. In both phases, the condition of macroscopic electroneutrality needs to be fulfilled upon phase separation, spatially restricting the counterions of the charged polymer to part of the volume. Additionally, the condition of thermodynamic equilibrium between the phases needs to be fulfilled. This leads to an inhomogeneous distribution of ions over the two phases and causes an electric potential difference due to the Donnan equilibrium [39–41]. The inhomogeneous ion distribution is also entropically unfavorable and counteracts phase separation [42, 43].

The main focus of this thesis is the effect of charge on one of the polymers on the interfacial thermodynamics and the phase behavior of an aqueous solution of two polymers. Experiments are performed on a model system of aqueous mixtures of dextran and gelatin. Dextran is a neutral polysaccharide, whereas gelatin is derived from the protein collagen and has a pH-dependent charge. Nongelling coldwater fish gelatin is used to avoid gelation. Chapter 2 describes measurements of the interfacial electric potential difference and its correlation with the phase behavior. This Chapter also discusses basic experimental techniques applied throughout the thesis, such as the preparation of samples and the determination of the composition of coexisting phases. A theoretical model to understand the macroscopic effects of polymer charge is developed in Chapter 3, where the so-called blob model that describes mixtures

of neutral polymers in solution is extended to include the effects of ion entropy. The model is compared with experimental observations for various values of the polymer charge, with attention to the phase behavior, critical demixing concentration, distribution of solvent, and interfacial electric potential difference. Measurements of the tension of the water–water interface, also as a function of polymer charge, are presented in Chapter 4, and the observations are discussed in terms of a model based on Poisson–Boltzmann theory. Chapter 5 reports the use of thin plate-like particles for the preparation of water-in-water Pickering emulsions and compares stabilization of emulsions by plate-like and spherical colloidal particles from a theoretical point of view. Finally, the main results presented in Chapters 2 to 5 are summarized.

CHAPTER 2

Donnan Potentials in Phase-Separated Aqueous Mixtures of Polyelectrolyte and Neutral Polymer

Abstract

The phase separation of aqueous mixed polymer solutions is affected not only by chemical differences between the polymers but also by their electric charge. Direct electrochemical measurements are performed of the electric potential difference between two coexisting phases in aqueous solutions of the charged protein fish gelatin (nongelling) and the uncharged polysaccharide dextran. Charge counteracts demixing because of the entropic cost of unequal ion concentrations in the two phases, resulting in a strong shift of the critical point upon an increase of the charge on one of the polymers. Upon phase separation, the charged polymer is spatially confined, and an interfacial electric potential difference is developed: the Donnan potential. A direct proportionality is found between the Donnan potential and the difference in gelatin concentration between the two phases, for which we propose a theoretical explanation, showing that the measured electric potential difference is a Donnan potential.

2.1 Introduction

Effects that determine the phase behavior of mixed polymer solutions are the affinities of the polymers for the solvent, the nonideal mixing behavior, and differences in chain statistics. When one of the polymers is a polyelectrolyte, an additional factor that plays a role is electric charge. With one of the polymers charged, phase separation will restrict not only each polymer to its own phase, but also the counterions of the charged polymer will have to be confined to one phase in order to ensure macroscopic electroneutrality. This adds to the entropic cost of phase separation: the critical point of demixing is expected to shift to higher concentrations as the charge on one of the polymers is increased.

As the polyelectrolyte is spatially restricted, the phase-separated mixture is expected to exhibit an interfacial electric potential difference. This potential difference has the same origin as the membrane potential that develops when a salt reservoir is separated by a dialysis membrane from a dispersion of charged colloids or polyelectrolytes. It is due to the Donnan equilibrium [39–41] and the associated interfacial or membrane potential is called the Donnan potential. Donnan potentials in aqueous two-phase systems have been studied before and have even been applied to the separation of charged biomolecules [35, 37]. However, the Donnan potentials in these systems stem from the addition of salts composed of cations and anions with different partitioning coefficients rather than from charge on one of the polymers [36, 38]. The relationships between polymer charge, Donnan potential, and phase behavior of aqueous polymer mixtures have to our knowledge not been studied before.

Here, we present the quantitative effect of charge on the phase behavior of aqueous mixtures of dextran and gelatin, in terms of the Donnan potential. Dextran is an uncharged, branched polysaccharide, while gelatin is a partially hydrolyzed form of the protein collagen with a pH-dependent charge. We use acid-extracted nongelling gelatin from coldwater fish, with an isoelectric point at approximately pH 8 [44]. Below this pH, the gelatin is positively charged, whereas at higher pH it is negatively charged. Besides the possibility to vary the charge on one of the polymers, other reasons to choose this system are relevance in the food industry, absence of complexation, and well-defined phase separation, as water is a good solvent for both polymers.

Determining the electric potential difference between the two phases is a challenge because the Donnan potential cannot be measured directly. If one would insert an identical reversible electrode in each phase, the potential difference between the two electrodes must eventually be zero [45, 46], as a system in thermodynamic equilibrium cannot perform work. A common approach to circumvent this problem is to use reference electrodes, connected via a salt bridge to each phase. As will be explained later, this method measures a quantity related to the Donnan potential: the Donnan

electromotive force (emf). However, under our experimental conditions, it can be shown that the Donnan emf has approximately the same value as the Donnan potential [45, 46]. We did not measure the ζ-potential of droplets of one phase suspended in the other, since it is the Donnan potential that is directly related to the equilibrium phase behavior, whereas the ζ-potential can even have a different sign, depending on the position of the shear plane [36].

The presence of a Donnan potential in aqueous two-phase systems is expected to be important for the stability of water-in-water emulsions. This interfacial electric potential may have an impact on droplet coalescence, the interfacial tension, and the adsorption of charged colloidal particles for the preparation of water-in-water Pickering emulsions.

This Chapter is organized as follows. First, it presents our theory for the Donnan potential at the liquid–liquid interface of phase-separated polymer mixtures. Second, experimental details are given regarding the preparation of samples, the determination of phase compositions and construction of phase diagrams, and the measurement of the Donnan potential. Third, measured Donnan potentials, phase behavior, and their correlation are presented. The Chapter ends with a general discussion and concluding remarks.

2.2 Theory

The Donnan equilibrium [39–41] is often considered for a system that consists of a solution of a polyelectrolyte in equilibrium with a salt reservoir. The polyelectrolyte solution is in a compartment α with concentration c_α^{P} and number of charges z per polymer chain (sign included), a reservoir β contains a monovalent salt with concentration c_{s}, and the two solutions are separated from each other by a semipermeable membrane. The membrane is permeable to the small ions and solvent but impermeable to the polyelectrolyte, hence the salt reservoir does not contain any polyelectrolyte. For such systems, the Donnan potential $\psi_{\mathrm{D}} = \psi_\alpha - \psi_\beta$ is given by

$$\psi_{\mathrm{D}} = \frac{RT}{F} \operatorname{arcsinh}\left(\frac{zc_\alpha^{\mathrm{P}}}{2c_{\mathrm{s}}}\right) \tag{2.1}$$

$$\simeq \frac{RT}{F}\frac{zc_\alpha^{\mathrm{P}}}{2c_{\mathrm{s}}}, \tag{2.2}$$

with R the gas constant, T the absolute temperature, and F the Faraday constant. This model does not apply directly to our system, which consists of two phases that both contain the polyelectrolyte gelatin at different concentrations.

In the following, the Donnan equilibrium will be briefly revisited for our system, by assuming that the infinitely large salt reservoir β now also contains polyelectrolyte.

In our system, both phases in addition contain dextran to varying degree, but since this is an uncharged polymer it does not affect the Donnan equilibrium. In Chapter 3 we will reconsider the Donnan equilibrium for the situation without a salt reservoir, where the total number of ions in the system is conserved upon phase separation.

Suppose that phase α is still the richest in the polyelectrolyte and that the phases again have a potential difference $\psi_D = \psi_\alpha - \psi_\beta$. In equilibrium, the concentration of the monovalent cations and anions in phase i, $c_i^\pm$, will be given by

$$c_\alpha^+ = c_\beta^+ \exp\left(-\frac{\psi_D F}{RT}\right), \tag{2.3a}$$

$$c_\alpha^- = c_\beta^- \exp\left(+\frac{\psi_D F}{RT}\right). \tag{2.3b}$$

For simplicity, the reduced electric potential y is defined as $y \equiv \exp(+\psi_D F/RT) \equiv \exp(\Psi_D)$, with Ψ_D the dimensionless Donnan potential.

The concentration of polyelectrolyte in phase i is denoted as c_i^P. Let us assume that the polyelectrolyte has a number of positive charges z per polymer chain. Overall, each phase should be electrically neutral, thus $c_\alpha^+ + zc_\alpha^P = c_\alpha^-$ and $c_\beta^+ + zc_\beta^P = c_\beta^-$. This can be combined with Equation (2.3) to yield:

$$c_\beta^+ y^{-1} + zc_\alpha^P = (c_\beta^+ + zc_\beta^P)y. \tag{2.4}$$

Solving for y gives:

$$y = \frac{zc_\alpha^P}{2(c_\beta^+ + zc_\beta^P)} + \sqrt{\left[\frac{zc_\alpha^P}{2(c_\beta^+ + zc_\beta^P)}\right]^2 + \frac{c_\beta^+}{c_\beta^+ + zc_\beta^P}}. \tag{2.5}$$

When it is assumed that in both phases the charge density due to the polyelectrolyte is smaller than that of the other ions (i.e., $zc_\alpha^P \ll c_\beta^+$ and $zc_\beta^P \ll c_\beta^+$), Equation (2.5) can be simplified. The first term can be approximated to first order as

$$\frac{zc_\alpha^P}{2(c_\beta^+ + zc_\beta^P)} \simeq \frac{zc_\alpha^P}{2c_\beta^+}. \tag{2.6}$$

When approximating the square root term to first order, the term $\{zc_\alpha^P/[2(c_\beta^+ + zc_\beta^P)]\}^2$ gives zero, while $c_\beta^+/(c_\beta^+ + zc_\beta^P) \simeq 1 - zc_\beta^P/c_\beta^+$. Thus,

$$\sqrt{\left[\frac{zc_\alpha^P}{2(c_\beta^+ + zc_\beta^P)}\right]^2 + \frac{c_\beta^+}{c_\beta^+ + zc_\beta^P}} \simeq \sqrt{1 - \frac{zc_\beta^P}{c_\beta^+}} \tag{2.7}$$

$$\simeq 1 - \frac{zc_\beta^P}{2c_\beta^+}. \tag{2.8}$$

Combining the two approximations gives the following linearized expression for y:

$$y \simeq 1 + \frac{z(c_\alpha^{\mathrm{P}} - c_\beta^{\mathrm{P}})}{2c_\beta^+}. \tag{2.9}$$

However, as $\Psi_{\mathrm{D}} \equiv \ln y$:

$$\Psi_{\mathrm{D}} = \ln\left[1 + \frac{z(c_\alpha^{\mathrm{P}} - c_\beta^{\mathrm{P}})}{2c_\beta^+}\right], \tag{2.10}$$

which can be linearized again using the relation $\ln(1 + x) \simeq x$:

$$\Psi_{\mathrm{D}} \simeq \frac{z(c_\alpha^{\mathrm{P}} - c_\beta^{\mathrm{P}})}{2c_\beta^+}. \tag{2.11}$$

With $\Delta c^{\mathrm{P}} \equiv c_\alpha^{\mathrm{P}} - c_\beta^{\mathrm{P}}$ and the approximation $c_\beta^+ \approx c_\beta^- = c_{\mathrm{s}}$, the Donnan potential ψ_{D} can be expressed as

$$\psi_{\mathrm{D}} \simeq \frac{RT}{F}\frac{z\Delta c^{\mathrm{P}}}{2c_{\mathrm{s}}}. \tag{2.12}$$

This expression is remarkably similar to Equation (2.2). By plotting Equations (2.5) and (2.12) it can be shown that Equation (2.12) describes the Donnan potential within 1 mV even if the polyelectrolyte charge density in the polyelectrolyte-rich phase is as high as the salt concentration in the polyelectrolyte-poor phase, that is, $zc_\alpha^{\mathrm{P}} \approx c_\beta^+$, resulting in Donnan potentials of the order of 10 mV. Our experiments fall well within this limit.

From Equation (2.12) it can be concluded that if, for samples with increasing concentrations, both the Donnan potential and gelatin concentration difference were measured, a plot of ψ_{D} versus Δc^{P} should give a straight line through the origin, with a slope proportional to the charge of the gelatin. In addition, Equation (2.12) also predicts that the Donnan potential should carry the same sign as the charge z of the gelatin.

2.3 Experimental

2.3.1 Sample Preparation

Stock solutions of dextran (Dx) were prepared by weighing the desired amounts of dextran (Sigma-Aldrich, from *Leuconostoc* spp., 100 kDa) and Milli-Q water. The dextran was dissolved by shaking the mixture at room temperature. Stock solutions

of gelatin (Gt) were prepared similarly, except that the gelatin (Norland Products, fish gelatin type A, gelling temperature 8 to 10 °C, high molar mass grade, approximately 100 kDa, kindly provided by FIB Foods, Harderwijk, The Netherlands) was dissolved using a warm water bath of 60 °C under magnetic stirring for approximately 30 minutes. This resulted in a solution with a pH of 6.2. For experiments at a different pH, part of the Milli-Q water in the gelatin stock solution was replaced by a dilute solution of HCl or NaOH. No buffer was used, as the gelatin itself already acts as a buffer. No preservatives were added because an agent like sodium azide might affect the electrochemical measurements. For experiments at increased ionic strength, the dextran and gelatin were dissolved in a KCl solution instead of Milli-Q water. For samples without additional salt, the ionic strength was approximately 5 to 10 mM due to salt present in (mainly) the gelatin. The polymer content of solutions will be, unless otherwise mentioned, expressed as mass fractions. For instance, the mass fraction of dextran is defined as $w_{\mathrm{Dx}} = m_{\mathrm{Dx}} / \sum_i m_i$, with m_i the total mass of component i. Typically, stock solutions had a total polymer fraction of 10 to 20 %. The polydispersity $M_{\mathrm{w}}/M_{\mathrm{n}}$ is about 2.5 for both polymers, where M_{w} and M_{n} are the weight- and number-averaged molar masses, respectively.

Samples were prepared by adding weighed amounts of the stock solutions and diluting (if necessary) with Milli-Q water, followed by vortex mixing. The pH and conductivity of the freshly mixed samples, which were turbid due to the onset of phase separation, were measured using a double junction pH electrode (Hanna Instruments pH 210 pH meter, HI 1043B electrode) and a four-electrode conductivity probe (WTW inoLab Cond Level 1, TetraCon 325 electrode). The ionic strengths of the samples were then deduced from conductivities measured on KCl solutions of known concentrations. The samples were centrifuged overnight at 20 °C at 100–200g (with the higher speeds for the more concentrated, viscous samples) to obtain fully phase-separated samples. For each sample, the gelatin-rich phase was denoted as α and the dextran-rich phase as β. Which of the two was the top phase and which was the bottom phase depended on circumstances such as pH and salt concentration. The overall dextran and gelatin mass fractions were kept equal to each other in all samples within an absolute deviation of 0.05 %.

After a sample was phase-separated, part of each phase was collected. First, as much as possible of the top phase was isolated using a syringe with hypodermic needle. Afterward, a fresh syringe with hypodermic needle was carefully lowered through the interface into the bottom phase, avoiding mixing of the phases. After the interface had recovered to its equilibrium position, part of the bottom phase was collected as well.

Stock solutions and isolated phases were stored at 1 °C. Before reuse, they were

heated again in a water bath of 60 °C for 15 minutes and subsequently allowed to cool to room temperature, for the gelatin to lose its helical gel structure [47]. Stock solutions and isolated phases were kept for a maximum of one week.

2.3.2 Determination of Phase Composition and Phase Diagrams

Since dextran and gelatin are both optically active, polarimetry was used to measure the mass fractions of dextran and gelatin in each phase of a phase-separated sample. As the optical rotation was measured at more than one wavelength, the mass fractions of dextran and gelatin could be found simultaneously in the coexisting phases, thus enabling the construction of phase diagrams [6, 48].

Part of an isolated phase, obtained as described before, was diluted by a known factor with water to contain approximately 2 % polymer. The optical rotation was measured at four different wavelengths (365, 436, 546, and 589 nm) on an Anton Paar MCP 500 polarimeter thermostated at 20.00 °C in a sample cell with a length of 1.0000 dm. The angular accuracy of this instrument is better than ±0.002°.

The optical rotation α^{λ_i} measured at wavelength λ_i is the sum of the optical rotations contributed by both dextran and gelatin:

$$\alpha^{\lambda_i} = [\alpha]_{\mathrm{Dx}}^{\lambda_i} l\, w_{\mathrm{Dx}} + [\alpha]_{\mathrm{Gt}}^{\lambda_i} l\, w_{\mathrm{Gt}}, \tag{2.13}$$

where $[\alpha]_{\mathrm{Dx}}^{\lambda_i}$ and $[\alpha]_{\mathrm{Gt}}^{\lambda_i}$ are the specific rotations per mass fraction of dextran and gelatin with units of deg/dm at wavelength λ_i, w_{Dx} and w_{Gt} are the mass fractions of dextran and gelatin, and $l = 1\,\mathrm{dm}$ is the length of the sample cell.

Under the condition that the ratio between the specific rotations of dextran and gelatin changes sufficiently as a function of wavelength, the mass fractions of dextran and gelatin can be determined from the optical rotation measured at a pair of wavelengths (λ_i and λ_j with $i \neq j$) as follows:

$$w_{\mathrm{Dx}}(\lambda_i, \lambda_j) = \frac{1}{l}\left(\frac{\alpha^{\lambda_j}[\alpha]_{\mathrm{Gt}}^{\lambda_i} - \alpha^{\lambda_i}[\alpha]_{\mathrm{Gt}}^{\lambda_j}}{[\alpha]_{\mathrm{Dx}}^{\lambda_j}[\alpha]_{\mathrm{Gt}}^{\lambda_i} - [\alpha]_{\mathrm{Dx}}^{\lambda_i}[\alpha]_{\mathrm{Gt}}^{\lambda_j}}\right), \tag{2.14a}$$

$$w_{\mathrm{Gt}}(\lambda_i, \lambda_j) = \frac{1}{l}\left(\frac{\alpha^{\lambda_i}[\alpha]_{\mathrm{Dx}}^{\lambda_j} - \alpha^{\lambda_j}[\alpha]_{\mathrm{Dx}}^{\lambda_i}}{[\alpha]_{\mathrm{Dx}}^{\lambda_j}[\alpha]_{\mathrm{Gt}}^{\lambda_i} - [\alpha]_{\mathrm{Dx}}^{\lambda_j}[\alpha]_{\mathrm{Gt}}^{\lambda_j}}\right). \tag{2.14b}$$

As we have measured the optical rotation at four wavelengths, there are six sets of two different wavelengths. The mass fractions were computed for each pair, and the average and standard deviations were calculated for each phase, taking into account the dilution. The absolute standard deviations in the mass fractions were typically well below 0.1 %. In a few instances, the combination $\lambda_i = 546\,\mathrm{nm}$ with $\lambda_j = 589\,\mathrm{nm}$ deviated more than 0.15 % from the mean, in which case it was excluded from the

Table 2.1: The measured specific rotations $[\alpha]_j^{\lambda_i}$ of the aqueous dextran and gelatin used in this study and their ratio $[\alpha]_{\mathrm{Dx}}^{\lambda_i}/[\alpha]_{\mathrm{Gt}}^{\lambda_i}$ at various wavelengths λ_i.

	Specific rotation (deg/dm)		
λ_i (nm)	Dextran	Gelatin	Ratio
365	+544	−369	−1.47
436	+358	−226	−1.59
546	+216	−129	−1.68
589	+183	−108	−1.70

results. The difference in the mass fraction of gelatin between the two phases α and β of a sample is defined as $\Delta w_{\mathrm{Gt}} = w_{\mathrm{Gt}}^{\alpha} - w_{\mathrm{Gt}}^{\beta}$. Its standard deviation is given by $s(\Delta w_{\mathrm{Gt}}) = [s^2(w_{\mathrm{Gt}}^{\alpha}) + s^2(w_{\mathrm{Gt}}^{\beta})]^{1/2}$, where $s(w_{\mathrm{Gt}}^{\alpha})$ and $s(w_{\mathrm{Gt}}^{\beta})$ are the standard deviations of the gelatin mass fractions for phases α and β.

The specific rotations of dextran and gelatin were obtained by measuring the optical rotations of aqueous solutions containing only dextran or gelatin of various mass fractions and performing a least-squares fit to the equation $\alpha_j^{\lambda_i} = [\alpha]_j^{\lambda_i} l\, w_j$. The resulting specific rotations are given in Table 2.1. We verified that under our experimental conditions, the specific rotation is not affected by the addition of salt or a change in pH. Further, by measuring the mass fractions in dilute non-phase separating aqueous mixtures of dextran and gelatin of known composition at various pH values and ionic strengths, we verified that the mass fractions that we find in this way are indeed the actual mass fractions of dextran and gelatin, within the margin of error indicated by the standard deviation.

2.3.3 Donnan Potential Measurements

Donnan potential measurements were carried out in a U-shaped glass tube, which was filled with the bottom phase from one side and subsequently with the top phase from the other side, after having isolated the phases as described before. Two identical Ag/AgCl reference electrodes were used in order to measure the Donnan potential. The key aspect here is that reference electrodes have, in principle, a well-defined and fixed potential difference with their surrounding solution. The potential difference between the two phases could be found by immersing one reference electrode in each phase, as schematically shown in Figure 2.1a, and comparing the electric potential difference to a baseline recorded when both electrodes were immersed in the same 100 mM KCl solution.

Radiometer Analytical REF200 Ag/AgCl electrodes were used. These electrodes

consist of a silver wire coated with silver chloride, immersed in a saturated potassium chloride solution. The solution is kept saturated by the presence of solid potassium chloride. The electrochemical half-reaction is $Ag(s) + Cl^-(aq) \rightleftharpoons AgCl(s) + e^-$. Because the concentration of Cl^- is constant, the electrochemical potential of the electrons is fixed with respect to the KCl solution. This KCl solution, in turn, was in contact via a small porous plug with the phase in which the electrode was immersed and leaked at about 10 µL per hour. Because the transport numbers of K^+ and Cl^- are nearly equal [49], the liquid junction potential with the polymer solution is close to zero. Additionally, because the saturated KCl solution was much more concentrated than the sample solution, the liquid junction potential is dominated by the electrode solution and therefore nearly independent of the sample composition [50]. The effect of streaming potentials, caused by liquid flow through the porous plug, was minimized by keeping the flow rates of the two reference electrodes as similar as possible. This was accomplished by having both electrodes filled to the same height with the saturated KCl solution and having the electrodes immersed at the same depth in both phases. In order to check that the measured potential would be symmetric with respect to the baseline, during each measurement the electrodes were swapped between the two phases. An asymmetric response to swapping would point to a failure of the earlier discussed assumptions. Before the electrodes were immersed in a solution, they were cleaned by rinsing with plentiful amounts of Milli-Q water and dabbed dry with a tissue.

It should be noted that, strictly speaking, measurements performed in this way by definition only yield the Donnan emf, which includes for instance the contributions of the liquid junction potentials. However, it can be shown that for systems that behave ideally (e.g. low charge density of the polymer chain, not too low salt concentration in the system, high salt concentration in the reference electrodes, identical transport numbers for K^+ and Cl^-) the Donnan emf is the same as the Donnan potential [45, 46]. This method has been employed successfully before in the determination of Donnan potentials in a system of sedimenting charged silica spheres in ethanol [51]. An alternative approach would be to use two capillary reference electrodes, one of which would cross the liquid–liquid interface [35–37], but we found that puncturing the interface perturbs it and causes mixing in a way that can lead to lengthy equilibration times.

The electric potentials were recorded as a function of time at an interval of 0.2 s using a Metrohm Autolab PGSTAT100 setup. One reference electrode (A) was connected to both the working electrode (WE) and sense (S) leads, whereas the other reference electrode (B) was connected to the counter electrode (CE) and reference electrode (RE) leads. All measurements were carried out in a grounded Faraday

cage, connected to the ground of the instrument, which is crucial to obtain reliable measurements. The experimentally determined Donnan potentials will be reported with respect to the dextran-rich phase.

2.4 Results

In this section, first an example of a measurement of the Donnan potential will be described. Next, the influence of the pH and ionic strength on the phase behavior will be presented. Finally, measurements of the Donnan potential as a function of polymer concentration for three different pH values will be shown in order to illustrate the relation between the phase behavior and the Donnan potential.

An example of a Donnan potential measurement is shown in Figure 2.1b, for a system consisting of 7.5 % dextran and 7.5 % gelatin at pH 4.8 and a salt concentration of 9.4 mM. The electric potential is recorded as a function of the time t and the measurement consists of four parts:

- $t = 0$ s: The reference electrodes are immersed in the same 100 mM KCl solution to record the baseline potential $V_1 = \langle V_A - V_B \rangle = +0.0121 \pm 0.0018$ mV.
- $t \approx 275$ s: Electrode A is immersed in the gelatin-rich phase and electrode B in the dextran-rich phase to obtain $V_2 = \langle V_A - V_B \rangle = +7.31 \pm 0.04$ mV.
- $t \approx 480$ s: The electrodes are reversed, with electrode B now immersed in the gelatin-rich phase and A in the dextran-rich phase, which gives $V_3 = \langle V_A - V_B \rangle = -7.204 \pm 0.019$ mV.
- $t \approx 680$ s: A final baseline is recorded by immersing both electrodes in 100 mM KCl, $V_4 = \langle V_A - V_B \rangle = +0.019 \pm 0.018$ mV.

For each part of the measurement, the potential is first allowed to stabilize before it is averaged over at least one minute. Using the differences between the values of V_i, the Donnan potential can be computed in three different ways: $\psi_1 = V_2 - V_1$, $\psi_2 = (V_2 - V_3)/2$, and $\psi_3 = V_4 - V_3$. Ideally, these measurements should be identical, whereas a strong asymmetry would point to for instance unstable liquid junction potentials. In practice, nearly symmetrical behavior is observed in all our experiments. For the present example, $\psi_1 = +7.30$ mV, $\psi_2 = +7.26$ mV, and $\psi_3 = +7.22$ mV were found. The Donnan potential ψ_D and its uncertainty are calculated as the average and standard deviation of ψ_1, ψ_2, and ψ_3, so in this case $\psi_D = +7.26 \pm 0.04$ mV.

Phase diagrams for aqueous mixtures of dextran and gelatin were measured at pH 6.2 ($c_s = 4.5$ mM) and pH 4.8 ($c_s = 9.4$ mM and 50 mM) and are shown in Figure 2.2, together with a photograph of a homogeneous and phase-separated mixture.

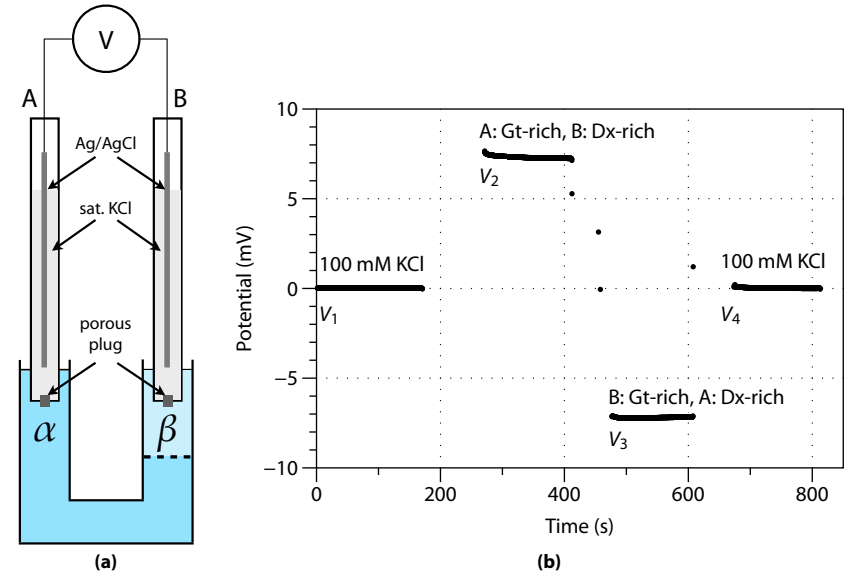

Figure 2.1: (a) Schematic representation of the setup for the measurement of the Donnan potential at the interface of demixed aqueous solutions of dextran and gelatin. A U-shaped tube is first filled with the heaviest phase (α), and then the lighter phase (β) is added. The Donnan potential is determined by inserting Ag/AgCl reference electrodes A and B at each end of the tube and measuring the potential difference $V_A - V_B$. (b) Example of a Donnan potential measurement on a phase-separated sample containing 7.5 % dextran and 7.5 % gelatin at pH 4.8 and a salt concentration of 9.4 mM. At $t = 0$ s, the two reference electrodes are immersed in a solution of 100 mM KCl; at $t \approx 275$ s, one reference electrode is immersed in each phase; at $t \approx 480$ s, the electrodes are reversed; and finally at $t \approx 680$ s, the electrodes are immersed again in 100 mM KCl. After each equilibration, the potential reaches a stable value, used for calculation of the Donnan potential.

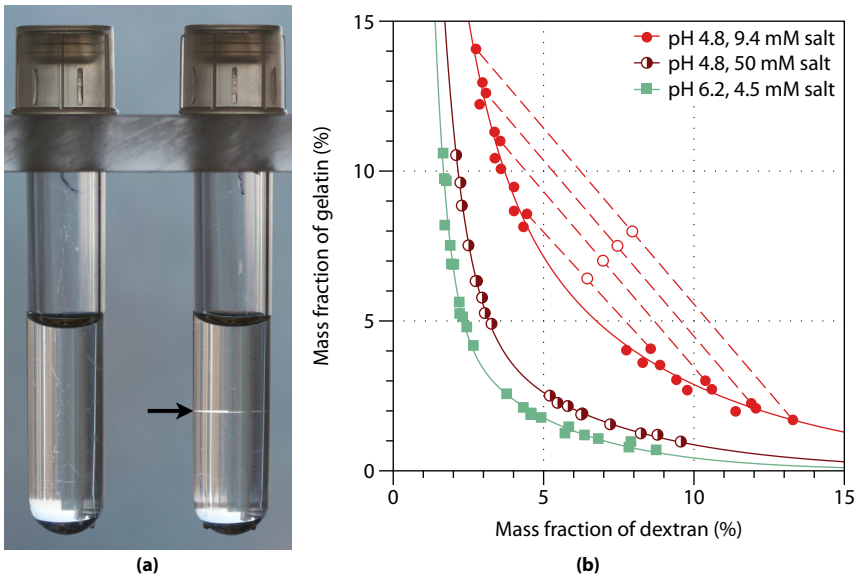

Figure 2.2: Phase behavior of aqueous mixtures of dextran and gelatin. The critical point depends strongly on pH and salt concentration. (a) Photograph of samples below and above the critical point, with dextran/gelatin mass fractions of (left) 6.0 / 5.9 % and (right) 6.5 / 6.4 % at pH 4.7 and a salt concentration of approximately 10 mM. The position of the water–water interface is indicated by an arrow. (b) Phase diagrams. At low salt concentrations (5 to 10 mM), the critical point shifts to higher concentrations when the charge of the gelatin is increased by lowering the pH. Addition of salt brings the critical point back to lower concentrations. For pH 4.8, the overall composition of some samples is shown (open circles) as well as the corresponding tie lines. The curves are a guide for the eye.

At pH 6.2, close to the isoelectric point of the gelatin (p$I \sim 8$), the gelatin is expected to be weakly positively charged. From the phase diagram, it can be found that the critical point is at a total polymer mass fraction of 6.3 %.

A large shift of the binodal is observed when the pH is decreased to 4.8, further away from the isoelectric point of gelatin. This is in line with expectations, as the gelatin is now more strongly positively charged, which makes phase separation more difficult due to the entropy of the ions. The critical demixing concentration is shifted to 12.3 %. When in addition the salt concentration is increased by an order of magnitude, the binodal shifts back close to the situation at pH 6.2 with low ionic strength. This is also reflected in the critical demixing concentration, now at 7.5 %.

Measurements of the Donnan potential were carried out as a function of the total polymer mass fraction at pH 4.8, 6.2, and 9.2 at salt concentrations of, on average, 9.4, 4.5, and 6.7 mM. The results are depicted in Figure 2.3, where the approximate

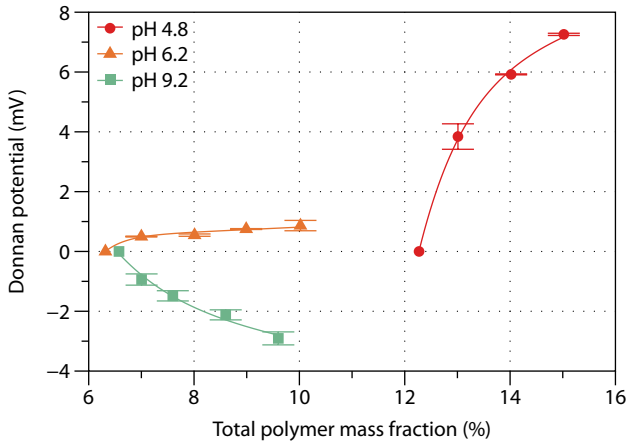

Figure 2.3: Measurements of the Donnan potential at low salt (5 to 10 mM) as a function of the total polymer fraction for various pH values. Below the isoelectric point (pI) of gelatin, a positive Donnan potential is observed, whereas above the pI, a negative Donnan potential is found. For each curve, the point at $\psi_D = 0$ mV indicates the critical demixing concentration. The lines are to guide the eye.

position of the critical point (determined from phase diagrams such as shown in Figure 2.2b) is indicated by the points at 0 mV. At pH 6.2, a positive Donnan potential that increases from 0.5 to 0.9 mV with increasing polymer content is found. When the gelatin becomes more strongly charged by changing the pH to 4.8, the Donnan potential increases by an order of magnitude. When the pH is increased above the isoelectric point of gelatin, a negative Donnan potential is observed, as expected from the change in sign of the charge of the gelatin. While the phase separation is "delayed" to much higher concentrations if the gelatin is more strongly charged, these measurements show that the Donnan potential actually increases much more rapidly as a function of concentration under these circumstances.

2.5 Discussion

The main premise of our study was that there should be an electric potential difference at the spontaneously formed interface of phase-separated aqueous solutions of dextran and gelatin. The charged polymer is spatially confined, so that an electric potential difference is expected on the basis of the Donnan equilibrium. Our measurements confirm that this is indeed the case. Here we discuss the relation with the observed phase behavior and the general implications for water–water interfaces and water-in-water emulsions.

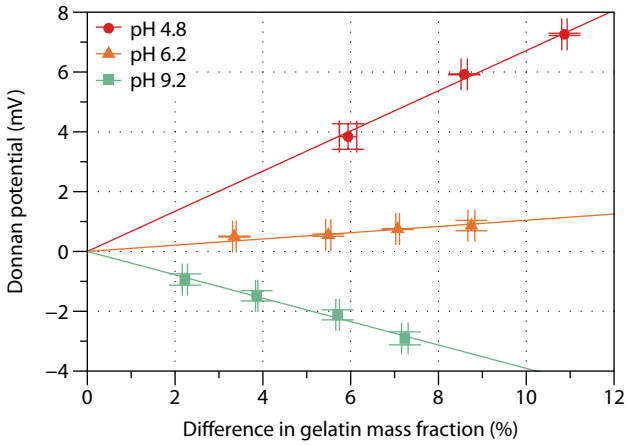

Figure 2.4: Measurements of the Donnan potential at low salt (5 to 10 mM) as a function of the difference in the mass fraction of gelatin between the two phases for various pH values. Below the pI, a positive Donnan potential is observed, whereas above the pI, a negative Donnan potential is found. The lines are linear fits through the origin.

According to Equation (2.12), the magnitude of the Donnan potential should be directly proportional to the difference in gelatin concentration Δc^{P} between the two phases. As the composition of the coexisting phases has been analyzed for each sample, a plot of the Donnan potential versus the difference in the gelatin mass fraction Δw_{Gt} can be constructed. As shown in Figure 2.4, the experimentally measured Donnan potential is indeed directly proportional to the difference in the gelatin mass fraction, in agreement with our theoretical prediction.

From Equation (2.12), the slopes $\partial\psi_{\mathrm{D}}/\partial\Delta w_{\mathrm{Gt}}$ in Figure 2.4 inform about the charge z of the gelatin. Taking into account the known salt concentration, the molar mass of gelatin (100 kDa), and a density of the solutions of approximately $1\,\mathrm{g/cm^3}$, the calculated charge of gelatin for the three pH values is given in Table 2.2. Qualitatively, the results conform well to measurements of the electrophoretic mobility of this type of gelatin known from literature [44]. Quantitative comparisons are much more difficult, because of the theoretical challenge of converting the electrophoretic mobility of a particle or (macro)molecule into its absolute charge.

Our measurements clearly show that the charge of gelatin has a strong influence on the phase behavior of aqueous mixtures of dextran and gelatin and that these effects largely disappear upon the addition of salt. It also leads to a measurable interfacial potential difference, and the magnitude of this Donnan potential evidently correlates to the critical demixing concentration. In order to understand the phase behavior, one can consider the role of the counterions. If a mixture phase separates, the counterions

Table 2.2: Charge of gelatin as calculated from Donnan potential measurements using Equation (2.12) at three pH values. The charge is calculated from the slope $\partial\psi_D/\partial\Delta w_{Gt}$ of the fit through the experimental data in Figure 2.4 and the average salt concentration $\langle c_s \rangle$ for each concentration series.

pH	$\frac{\partial\psi_D}{\partial\Delta w_{Gt}}$ (mV)	$\langle c_s \rangle$ (mM)	z
4.8	+67	9.4	+4.9
6.2	+10	4.5	+0.4
9.2	−39	6.7	−2.0

associated with the charged gelatin also have to be confined in one phase, which leads to an entropically unfavorable difference in concentration of ions between the two phases. For an increased salt concentration, the relative concentration difference is smaller and the influence of charge on the phase behavior is greatly reduced. Therefore, it is the concentration ratio of counterions to background salt that is important for the phase behavior. The effect of ion entropy will be treated in detail in Chapter 3.

The presence of a Donnan potential may also have other implications, for instance for the coalescence of droplets during phase separation. If droplets carry an interfacial electric potential due to the Donnan effect, their coalescence may be impeded. One may also speculate how the interfacial potential influences the interfacial tension, because of the energy stored in the interfacial electric double layer, which basically functions as a capacitor. This topic will be the focus of Chapter 4. Finally, the presence of an interfacial potential difference may affect the stiffness and preferential curvature of the interface [32] and consequently the droplet stability.

2.6 Conclusions

The phase separation of aqueous polymer mixtures depends not only on chemical differences between the polymers but also on charge. Important for the phase behavior is the concentration ratio of counterions to background salt. The influence of charge manifests itself through a spontaneous interfacial electric potential difference, which can be described on the basis of thermodynamic salt equilibrium. The measured Donnan potential scales as expected from theory with the difference in concentration of the charged polymer between the two phases.

CHAPTER 3

Ion Entropy in Phase-Separated Aqueous Mixtures of Polyelectrolyte and Neutral Polymer

Abstract

The macroscopic phase separation of aqueous mixtures of a neutral polymer and a polyelectrolyte is well described by a modified blob model, taking into account the entropy of ideal ions under the restriction of macroscopic charge neutrality. This is demonstrated by detailed measurements on aqueous mixtures of a neutral polymer (dextran) and a polymer whose charge is adjustable via the pH (nongelling fish gelatin). The critical point of the phase diagram of demixing, the asymmetric distribution of the solvent, and the interfacial electric potential difference all depend on polyelectrolyte charge and background salt concentration in a manner that is consistent with a dominant role for ion entropy.

3.1 Introduction

When a solution of a polyelectrolyte and a neutral polymer phase-separates, the counterions of the charged polymer are restricted to part of the volume because the condition of macroscopic electroneutrality needs to be fulfilled in both phases. Together with the requirement of thermodynamic stability, this leads to an inhomogeneous distribution of ions over the two phases, causing an electric potential difference. Chapter 2 showed that for aqueous mixtures of dextran (uncharged) and gelatin (pH-dependent charge) this electric potential difference—a Donnan potential [39–41]—follows the magnitude and sign of the charge on the gelatin [26, 52]. In addition, for gelatin that was more strongly charged, the critical point of demixing was shifted to higher concentrations, as seen before for other mixtures as well [42].

Much literature has been devoted to the theoretical understanding of the phase behavior of polymer mixtures in solution. Flory–Huggins type theory is very versatile in this regard and has been used to describe both associative and segregative phase separation [17]. For instance, Voorn and Overbeek [53, 54] described the complex coacervation observed by Bungenberg de Jong [18] by combining Flory–Huggins theory with Debye–Hückel theory to account for the electrostatic interactions. Since then, more elaborate models have been proposed as well [55]. However, while Flory–Huggins theory qualitatively describes the experimental trends and is useful to gain fundamental insights, it is not a quantitative theory. More quantitative models include the blob model for semidilute polymer solutions by Broseta and co-workers [25, 56, 57]. It describes segregative phase separation and shows quantitative agreement with experiments, for instance regarding the interfacial tension [25].

Here, we study both experimentally and theoretically the behavior of aqueous mixtures of a neutral polymer with a charged polymer, respectively dextran and (nongelling) fish gelatin. Dextran is a branched polysaccharide; gelatin is a partly hydrolyzed form of collagen, a linear protein, and a (weak) polyelectrolyte with a pH-dependent charge. Aqueous mixtures of dextran and gelatin separate into a dextran- and a gelatin-rich phase when their concentration is increased above the critical point of demixing, which lies typically below total polymer mass fractions of 10 %. Because of the requirements of macroscopic electroneutrality in each phase and thermodynamic equilibrium of the ions upon phase separation, the concentrations of the ions in the two phases are unequal. This not only leads to the formation of a Donnan potential [26, 52], but it is also entropically unfavorable, thereby favoring mixing. We expect the entropy of ions to have a major influence on the phase behavior of mixtures of charged and uncharged polymers in solution. We also presume that the addition of salt reduces the relative concentration differences, thereby lowering Donnan potentials and entropic penalties and favoring demixing.

This Chapter presents detailed and quantitative experimental measurements on the phase behavior, critical point, distribution of solvent, and Donnan potential as a function of the polyelectrolyte charge and background salt concentration. Our measurements will be compared to theory based on the blob model of mixed polymer solutions. Effects of charges are taken into account via analytical expressions for the ion entropy and the equilibrium salt distribution in the system, which are combined with the blob model to describe mixtures of polyelectrolyte and neutral polymer in solution.

The Chapter is organized as follows. First, the theoretical framework will be discussed: the blob model, the expressions for the ion entropy, the calculation of the equilibrium salt distribution, the calculation of the Donnan potential, and the expression for the total free energy of the system (blobs plus ions). Second, the experimental details will be discussed. Third, the results obtained from theory and experiment will be given, which will be discussed subsequently. Finally, the main conclusions will be summarized. Appendices to this Chapter give additional data and expressions.

3.2 Theory

In this section, the theoretical framework describing the experimental system is established. First, the blob model is discussed, which describes mixtures of two different polymers in solution. Then, in order to capture the effect of charges on one of the polymers, an expression for the entropy of the ions in the system is derived for an arbitrary distribution of ions. Using this expression, the equilibrium ion distribution is found by maximizing the ion entropy. This resulting ion distribution is used to calculate the Donnan potential. Finally, the blob model is combined with the model of the ion entropy in order to account for the phase behavior of aqueous mixtures of a neutral and a charged polymer. A list of symbols starts on Page 117.

3.2.1 Blob Model

The blob model is a convenient way to describe a mixture of two polymers in solution, as it reduces a three-component system to an effective two-component system. In the blob model [25, 26, 32, 56, 57], a polymer of N segments forms blobs with typical size ξ and consists of N_b blobs. The blobs form an ideal chain, whereas the excluded volume effects are restricted to the volume inside one blob. We assume that our polyelectrolyte and uncharged polymer have the same number of segments, blob size, and interaction with the solvent. The two have an interaction with each other characterized by $u(c)$, a concentration dependent interaction parameter. The blobs of the polyelectrolyte (at

volume fraction ϕ) and uncharged polymer (at volume fraction $1-\phi$) together fill the whole volume. The solvent is taken into account implicitly.

The parameters ξ, N_b, and u all depend on the total monomer concentration c (number of monomers per unit volume). The free energy density f^{blob} is given by [25, 26, 32, 56, 57]

$$f^{\text{blob}}(c,\phi) \equiv \frac{F^{\text{blob}}(c,\phi)}{VkT} \tag{3.1}$$

$$= \frac{1}{\xi^3(c)}\left[\frac{\phi}{N_b(c)}\ln\phi + \frac{1-\phi}{N_b(c)}\ln(1-\phi) + u(c)\phi(1-\phi) + K\right], \tag{3.2}$$

where $F^{\text{blob}}(c,\phi)$ is the free energy, V is the volume, k is the Boltzmann constant, T is the absolute temperature, and $K = 0.024$ is an additional constant related to the free energy of mixing of monomers within a blob [56].

The following scaling relations apply [26, 32, 56]:

$$\xi(c) \simeq 0.43 R_g \left(\frac{c}{c^*}\right)^{-\frac{\nu}{3\nu-1}}, \tag{3.3}$$

$$N_b(c) = \frac{N}{c\xi^3(c)}, \tag{3.4}$$

$$u(c) \simeq u_{\text{crit}}\left(\frac{c}{c_{\text{crit}}}\right)^{\frac{\chi}{3\nu-1}}, \tag{3.5}$$

where R_g is the radius of gyration and the scaling exponents are $\nu = 3/5$ and $\chi = 0.22$ for a good solvent. The overlap concentration c^* is defined as

$$c^* = \frac{N}{\frac{4}{3}\pi R_g^3}, \tag{3.6}$$

with the number of segments N defined by the ratio of molar mass of the polymer and the segments:

$$N = \frac{M_{w,\text{polymer}}}{M_{w,\text{monomer}}}. \tag{3.7}$$

Furthermore, we define the interaction energy $u(c) = u_{\text{crit}}$ at $c = c_{\text{crit}}$. In order to make the connection to the experimental system, we take c_{crit} as the monomer concentration where experimentally phase separation is just observed close to the isoelectric point (p*I*) of the polyelectrolyte. Similarly, u_{crit} is chosen such that the total polymer mass fraction at the critical point found from the theory matches that found from experiments close to the p*I*. For comparison with experiments, the monomer concentration c is converted to the mass fraction w using the equations in Appendix C. Other parameters are either found from experiments or obtained from theory. An overview is given in Table 3.1.

Table 3.1: Values of the parameters used in the calculations.

parameter	value	description
ν	$3/5$	scaling parameter [56]
χ	0.22	scaling parameter [56]
K	0.024	constant related to free energy of mixing within blob [56]
R_g	9.3 nm	radius of gyration, taken to be R_g of dextran [58]
$M_{w,polymer}$	100 kg/mol	average molar mass of dextran and gelatin
$M_{w,monomer}$	0.1 kg/mol	approximate molar mass of a monomer
$\rho_{polymer}$	1496 kg/m^3	average densities of dextran and gelatin in solution, see Appendix B
$\rho_{solvent}$	998 kg/m^3	density of water at 20 °C [59]
w_{crit}	0.063	experimental mass fraction of phase separation
c_{crit}	3.9×10^{26} m^{-3}	calculated from w_{crit} using Equation (C.1)
u_{crit}	0.03	interaction at c_{crit}; fit parameter

Knowing the free energy density of mixing, one can write down the change in the blob free energy upon demixing, $\Delta f^{blob}(c_0, \phi_0)$, where c_0 is the global monomer concentration and ϕ_0 the global volume fraction of polyelectrolyte blobs (therefore, the global volume fraction of neutral polymer blobs is $1 - \phi_0$). With monomer concentrations and polyelectrolyte blob volume fractions (c_α, ϕ_α) and (c_β, ϕ_β) in phases α and β, respectively, one obtains:

$$\Delta f^{blob}(c_0, \phi_0) = \theta f^{blob}(c_\alpha, \phi_\alpha) + (1 - \theta) f^{blob}(c_\beta, \phi_\beta) - f^{blob}(c_0, \phi_0), \tag{3.8}$$

where $\theta \equiv V_\alpha / V$, the relative volume of phase α, for which an expression will be derived in Section 3.2.5, under the conditions that the total amounts of polyelectrolyte and neutral polymer in the system are conserved.

3.2.2 Entropy of the Ions

The change in entropy of the ions when the system phase separates, assuming ideal behavior, is given by

$$\Delta S^{ions} = N_\alpha^+ k \ln\left(\frac{c_0^+}{c_\alpha^+}\right) + N_\beta^+ k \ln\left(\frac{c_0^+}{c_\beta^+}\right) + N_\alpha^- k \ln\left(\frac{c_0^-}{c_\alpha^-}\right) + N_\beta^- k \ln\left(\frac{c_0^-}{c_\beta^-}\right). \tag{3.9}$$

Here N_j^i is the number of ions of type i in phase j, and $c_j^i = N_j^i/V_j$, with V_j the volume of phase j. The subscript 0 again refers to the global concentrations, i.e., before phase separation.

If a polyelectrolyte with a number of positive charges z is present at a global number of *chains* per unit volume c_0^{p}, the ion concentrations before phase separation are given by

$$c_0^+ \equiv c_{\mathrm{s}}, \tag{3.10}$$

$$c_0^- = c_{\mathrm{s}} + zc_0^{\mathrm{p}}, \tag{3.11}$$

taking into account electroneutrality and using c_{s} to denote the background salt concentration.

The concentrations after phase separation for phase α are:

$$c_\alpha^+ = c_{\mathrm{s}} - \frac{N_{\mathrm{ex}}}{V_\alpha} \tag{3.12}$$

$$= c_{\mathrm{s}} - \frac{c_{\mathrm{ex}}}{\theta}, \tag{3.13}$$

$$c_\alpha^- = c_{\mathrm{s}} + zc_\alpha^{\mathrm{p}} - \frac{c_{\mathrm{ex}}}{\theta}, \tag{3.14}$$

where the system has the freedom to move N_{ex} ions from phase α to β. The expelled salt concentration c_{ex} is defined as the number of transferred ions divided by the total volume, i.e.,

$$c_{\mathrm{ex}} \equiv N_{\mathrm{ex}}/V, \tag{3.15}$$

θ is the relative volume of phase α:

$$\theta \equiv V_\alpha/V, \tag{3.16}$$

and c_α^{p} is the number of polyelectrolyte chains per unit volume in phase α. Similarly, for phase β:

$$c_\beta^+ = c_{\mathrm{s}} + \frac{c_{\mathrm{ex}}}{1-\theta}, \tag{3.17}$$

$$c_\beta^- = c_{\mathrm{s}} + zc_\beta^{\mathrm{p}} + \frac{c_{\mathrm{ex}}}{1-\theta}. \tag{3.18}$$

Defining $\Delta s^{\mathrm{ions}} \equiv \Delta S^{\mathrm{ions}}/(Vk)$, inserting the expressions for $c_j^\pm$ into Equation (3.9),

and using $c_0^{\mathrm{P}} = c_\alpha^{\mathrm{P}}\theta + c_\beta^{\mathrm{P}}(1-\theta)$, one finds

$$\begin{aligned}\Delta s^{\mathrm{ions}} = {} & (c_{\mathrm{s}}\theta - c_{\mathrm{ex}})\ln\left(\frac{c_{\mathrm{s}}}{c_{\mathrm{s}} - \frac{c_{\mathrm{ex}}}{\theta}}\right) \\ & + [(c_{\mathrm{s}} + zc_\alpha^{\mathrm{P}})\theta - c_{\mathrm{ex}}]\ln\left[\frac{c_{\mathrm{s}} + zc_\alpha^{\mathrm{P}}\theta + zc_\beta^{\mathrm{P}}(1-\theta)}{c_{\mathrm{s}} + zc_\alpha^{\mathrm{P}} - \frac{c_{\mathrm{ex}}}{\theta}}\right] \\ & + [c_{\mathrm{s}}(1-\theta) + c_{\mathrm{ex}}]\ln\left(\frac{c_{\mathrm{s}}}{c_{\mathrm{s}} + \frac{c_{\mathrm{ex}}}{1-\theta}}\right) \\ & + [(c_{\mathrm{s}} + zc_\beta^{\mathrm{P}})(1-\theta) + c_{\mathrm{ex}}]\ln\left[\frac{c_{\mathrm{s}} + zc_\alpha^{\mathrm{P}}\theta + zc_\beta^{\mathrm{P}}(1-\theta)}{c_{\mathrm{s}} + zc_\beta^{\mathrm{P}} + \frac{c_{\mathrm{ex}}}{1-\theta}}\right].\end{aligned} \tag{3.19}$$

Note that, since we are assuming ideal behavior, the free energy change per VkT is just given by

$$\Delta f^{\mathrm{ions}} \equiv \frac{\Delta F^{\mathrm{ions}}}{VkT} = -\frac{\Delta S^{\mathrm{ions}}}{Vk} = -\Delta s^{\mathrm{ions}}. \tag{3.20}$$

A different form of Equation (3.19) can be found by replacing the concentrations c_j^{P} by the fraction of the total amount of polyelectrolyte that resides in phase α, defined as $\eta^{\mathrm{P}} \equiv n_\alpha^{\mathrm{P}}/(n_\alpha^{\mathrm{P}} + n_\beta^{\mathrm{P}}) = c_\alpha^{\mathrm{P}}\theta/c_0^{\mathrm{P}}$, with n_j^{P} the number of moles of polyelectrolyte in phase j. This form and its usage to obtain the approximations given in the following are described in Appendix D.

3.2.3 Calculation of Equilibrium Salt Distribution

In order to find the equilibrium salt distribution in the system, we need to minimize the free energy of the ions with respect to c_{ex}. As ideal behavior is assumed, this is equivalent to maximizing the entropy of the ions. Taking the derivative of Equation (3.19) to c_{ex}, equating the resulting expression to zero, and solving for c_{ex} results in:

$$\begin{aligned}c_{\mathrm{ex}} = c_{\mathrm{s}}\theta\frac{1-\theta}{1-2\theta}\Bigg(1 + {} & \frac{z[c_\alpha^{\mathrm{P}}(1-\theta) + c_\beta^{\mathrm{P}}\theta]}{2c_{\mathrm{s}}} \\ & - \sqrt{1 + \frac{z[c_\alpha^{\mathrm{P}}\theta + c_\beta^{\mathrm{P}}(1-\theta)]}{c_{\mathrm{s}}} + \left\{\frac{z[c_\alpha^{\mathrm{P}}(1-\theta) + c_\beta^{\mathrm{P}}\theta]}{2c_{\mathrm{s}}}\right\}^2}\Bigg),\end{aligned} \tag{3.21}$$

where we have discarded the unphysical root that follows from solving the quadratic equation (using the condition that for $c_\alpha^{\mathrm{P}} = c_\beta^{\mathrm{P}}$, c_{ex} must be zero). It should be noted

that Equation (3.21) is indeterminate for $\theta = ½$, although this point does not have a special physical meaning. Instead, the following solution is valid for $\theta = ½$:

$$c_{\mathrm{ex}} = \frac{z(c_\alpha^{\mathrm{P}} - c_\beta^{\mathrm{P}})}{4} \frac{1}{2 + \frac{z(c_\alpha^{\mathrm{P}} + c_\beta^{\mathrm{P}})}{2c_{\mathrm{s}}}}. \tag{3.22}$$

Thus, by inserting the appropriate expression for c_{ex} into Δs^{ions}, one obtains a complicated but analytic expression for the entropy change of the ions upon phase separation. The resulting expressions are given in Appendix D. A compact approximation for the change in ion entropy is given by

$$\Delta s^{\mathrm{ions}} \simeq -\frac{\theta(1-\theta)}{2} \frac{(zc_\alpha^{\mathrm{P}} - zc_\beta^{\mathrm{P}})^2}{2c_{\mathrm{s}} + z[c_\alpha^{\mathrm{P}}\theta + c_\beta^{\mathrm{P}}(1-\theta)]}, \tag{3.23}$$

which is valid until the polyelectrolyte charge density is comparable to the salt concentration.

3.2.4 Donnan Potential

As we saw in Chapter 2, the classical Donnan equilibrium [39, 40, 46] describes a solution of polyelectrolyte (phase α) in equilibrium with an infinitely large salt reservoir (β). The salt reservoir is separated from the polyelectrolyte solution by a membrane which is permeable to small ions, but not to polyelectrolyte, so that the salt reservoir does not contain any polyelectrolyte. In that situation, the potential difference between the two phases is given by Equation (2.1) on Page 7.

With Equation (2.5), we addressed the issue that in our system both phases contain polyelectrolyte to some degree, but we did not take into account that phase β is of a size comparable to phase α. In the following, we will concentrate on the latter issue, by reconsidering the Donnan effect for a conserved number of ions in the system using the equilibrium distribution of ions between the two phases from Section 3.2.3. Assuming a Boltzmann (i.e., ideal) distribution of the ions over the two phases with potential difference $\psi_{\mathrm{D}} = \psi_\alpha - \psi_\beta$, one can find a general expression for the Donnan potential:

$$\psi_{\mathrm{D}} = \frac{RT}{F} \ln\left(\frac{c_\beta^+}{c_\alpha^+}\right) \tag{3.24}$$

$$= \frac{RT}{F} \ln\left(\frac{c_{\mathrm{s}} + \frac{c_{\mathrm{ex}}}{1-\theta}}{c_{\mathrm{s}} - \frac{c_{\mathrm{ex}}}{\theta}}\right). \tag{3.25}$$

using the definitions from Equations (3.13) and (3.17).

In the following, this expression will be evaluated for two situations, where the volumes of the phases are either equal or unequal.

Equal Phase Volumes

For the situation where $\theta = ½$, the expression for c_{ex} is relatively simple and given by Equation (3.22). After some algebra, one finds:

$$\psi_D = \frac{RT}{F} \ln\left(\frac{1 + \frac{zc_\alpha^P}{2c_s}}{1 + \frac{zc_\beta^P}{2c_s}} \right). \tag{3.26}$$

It is worth noting that, upon exchanging the concentrations of the polyelectrolyte between the two phases, the sign of ψ_D reverses, but its magnitude remains the same, as expected.

A good approximation (for $|\psi_D| \lesssim 20\,\text{mV}$) is found to be:

$$\psi_D \simeq \frac{RT}{F} \frac{z(c_\alpha^P - c_\beta^P)}{2c_s + \frac{1}{2}z(c_\alpha^P + c_\beta^P)}. \tag{3.27}$$

Comparing Equation (3.27) with the classic expression, Equation (2.1), one sees that the absence of an infinitely large salt reservoir leads to a reduction of the Donnan potential, even if there is no polyelectrolyte in phase β.

Unequal Phase Volumes

In the situation where the volumes of the two phases are not equal, the Donnan potential is found by inserting Equation (3.21) into Equation (3.25):

$$\begin{aligned} \psi_D = \frac{RT}{F} \ln\Bigg[\frac{c_s}{c_s + zc_\beta^P(1-\theta)} \Bigg(& \frac{z[c_\alpha^P(1-\theta) - c_\beta^P\theta]}{2c_s} \\ & + \sqrt{1 + \frac{z[c_\alpha^P\theta + c_\beta^P(1-\theta)]}{c_s} + \left\{ \frac{z[c_\alpha^P(1-\theta) + c_\beta^P\theta]}{2c_s} \right\}^2} \Bigg) \Bigg]. \end{aligned} \tag{3.28}$$

In the limit of $\theta \to 0$, this expression becomes equivalent to Equation (2.5).

An approximation of Equation (3.28) can be found for low ψ_D:

$$\psi_D \simeq \frac{RT}{F} \frac{z(c_\alpha^P - c_\beta^P)}{2c_s + z[c_\alpha^P\theta + c_\beta^P(1-\theta)]} \tag{3.29}$$

$$= \frac{RT}{F} \frac{z\Delta c^P}{2c_s + zc_0^P}, \tag{3.30}$$

where $\Delta c^P \equiv c_\alpha^P - c_\beta^P$ and c_0^P is the global polyelectrolyte concentration. Therefore, to first order, the reduction of the Donnan potential due to the absence of a salt reservoir

is equivalent to an increase of the salt concentration by $\frac{1}{2} z c_0^{\mathrm{p}}$ in the classic Donnan equilibrium. Additionally, it is not the absolute concentration of polyelectrolyte in one of the phases that is important, but rather the concentration difference between the two phases.

If $z c_0^{\mathrm{p}}$ is negligible with respect to c_{s}, Equation (3.30) further approximates to

$$\psi_{\mathrm{D}} \simeq \frac{RT}{F} \frac{z \Delta c^{\mathrm{p}}}{2 c_{\mathrm{s}}}. \tag{3.31}$$

This expression closely resembles the approximation of the classical expression, Equation (2.2): the concentration difference of the polyelectrolyte now replaces the absolute polyelectrolyte concentration. It is also identical to Equation (2.12), which shows that for sufficiently high salt concentration, the relative volumes of the phases do not matter.

Equation (3.28) can be shown to reduce to the classic Donnan equilibrium, if one takes the limit where phase β is infinitely large. To do so, one takes $\theta \to 0$ and assumes $c_\beta^{\mathrm{p}} = 0$, in order to find that

$$\psi_{\mathrm{D}} = \frac{RT}{F} \ln \left[\frac{z c_\alpha^{\mathrm{p}}}{2 c_{\mathrm{s}}} + \sqrt{1 + \left(\frac{z c_\alpha^{\mathrm{p}}}{2 c_{\mathrm{s}}} \right)^2} \right], \tag{3.32}$$

which is indeed identical to Equation (2.1), because $\ln(x + \sqrt{1 + x^2})$ is equal to $\operatorname{arcsinh} x$.

3.2.5 Total Free Energy

Since we now know both the free energy change upon demixing for the blobs and for the ions, we write the total free energy change (scaled to VkT) of the system as follows:

$$\Delta f(c_0, \phi_0) = \Delta f^{\mathrm{blob}}(c_0, \phi_0) - \Delta s^{\mathrm{ions}}(c_\alpha^{\mathrm{p}}, c_\beta^{\mathrm{p}}, \theta) \tag{3.33}$$

$$\begin{aligned} &= \theta f^{\mathrm{blob}}(c_\alpha, \phi_\alpha) + (1 - \theta) f^{\mathrm{blob}}(c_\beta, \phi_\beta) - f^{\mathrm{blob}}(c_0, \phi_0) \\ &\quad - \Delta s^{\mathrm{ions}}(c_\alpha^{\mathrm{p}}, c_\beta^{\mathrm{p}}, \theta). \end{aligned} \tag{3.34}$$

An expression for $\theta \equiv V_\alpha / V$ can be found from the conservation of mass. Suppose that the system is composed of n^{p} moles of polyelectrolyte and n^{u} moles of uncharged polymer. $x_0 = n^{\mathrm{p}} / (n^{\mathrm{p}} + n^{\mathrm{u}})$ is the global mole fraction of polyelectrolyte with respect to the total amount of polymer, x_α and x_β similarly are the mole fractions of polyelectrolyte in each phase. The amounts of polyelectrolyte and uncharged polymer in the total system are given by $n^{\mathrm{p}} = n_\alpha^{\mathrm{p}} + n_\beta^{\mathrm{p}}$ and $n^{\mathrm{u}} = n_\alpha^{\mathrm{u}} + n_\beta^{\mathrm{u}}$, respectively.

For the polyelectrolyte with degree of polymerization N^{p}, the total amount of polyelectrolyte can be expressed as $n^{\mathrm{p}} = (c_0 / N^{\mathrm{p}}) x_0 V$. Likewise, $n_\alpha^{\mathrm{p}} = (c_\alpha / N^{\mathrm{p}}) x_\alpha V_\alpha$

and $n_\beta^{\mathrm{p}} = (c_\beta / N^{\mathrm{p}}) x_\beta V_\beta$. From this, the following expression for θ can be found:

$$\theta = \frac{c_0 x_0 - c_\beta x_\beta}{c_\alpha x_\alpha - c_\beta x_\beta}. \tag{3.35}$$

Similarly, for the uncharged polymer,

$$\theta = \frac{c_0 (1 - x_0) - c_\beta (1 - x_\beta)}{c_\alpha (1 - x_\alpha) - c_\beta (1 - x_\beta)}. \tag{3.36}$$

For θ to be uniquely defined, Equations (3.35) and (3.36) need to be equated and solved, which we choose to do for c_β, yielding

$$c_\beta = \frac{c_0 c_\alpha (x_0 - x_\alpha)}{c_0 (x_0 - x_\beta) + c_\alpha (x_\beta - x_\alpha)}. \tag{3.37}$$

In other words, from the three concentrations c_0, c_α, and c_β, we can freely choose only two, due to the coupling of the conservation of mass of the two polymers via the volume of the phases. In the following, we will therefore only keep c_0 and c_α as independent variables. Inserting Equation (3.37) into Equation (3.35) or (3.36) gives

$$\theta = \frac{c_0 (x_0 - x_\beta)}{c_\alpha (x_\alpha - x_\beta)}. \tag{3.38}$$

The question now is how the mole fraction x relates to the volume fraction of polyelectrolyte blobs ϕ. The volume fraction ϕ_j in phase j ($j = 0, \alpha, \beta$) is given by the volume occupied by blobs of polyelectrolyte, divided by the volume occupied by blobs of polyelectrolyte and uncharged polymer:

$$\phi_j = \frac{N_{\mathrm{b},j}^{\mathrm{p}} n_j^{\mathrm{p}} (\xi_j^{\mathrm{p}})^3}{N_{\mathrm{b},j}^{\mathrm{p}} n_j^{\mathrm{p}} (\xi_j^{\mathrm{p}})^3 + N_{\mathrm{b},j}^{\mathrm{u}} n_j^{\mathrm{u}} (\xi_j^{\mathrm{u}})^3}. \tag{3.39}$$

For generality, it is assumed that the number of blobs per polymer chain $N_{\mathrm{b},j}^k$ and blob size ξ_j^k depend on both the type of polymer ($k = \mathrm{p}, \mathrm{u}$) and the phase j. According to Equation (3.4), $N_{\mathrm{b},j}^k$ is given by

$$N_{\mathrm{b},j}^k = \frac{N^k}{c_j (\xi_j^k)^3}, \tag{3.40}$$

for a degree of polymerization N^k. Additionally,

$$n_j^{\mathrm{p}} = n_j x_j, \tag{3.41}$$

$$n_j^{\mathrm{u}} = n_j (1 - x_j), \tag{3.42}$$

so that the volume fraction ϕ_j can be written as

$$\phi_j = \frac{N^{\mathrm{p}} x_j}{N^{\mathrm{p}} x_j + N^{\mathrm{u}}(1 - x_j)}. \tag{3.43}$$

We assume that the degree of polymerization of the two polymers is the same, so

$$\phi_j = x_j. \tag{3.44}$$

Therefore, $\theta = \theta(c_0, c_\alpha, \phi_0, \phi_\alpha, \phi_\beta)$ and it is given by

$$\theta = \frac{c_0(\phi_0 - \phi_\beta)}{c_\alpha(\phi_\alpha - \phi_\beta)}. \tag{3.45}$$

The polyelectrolyte chain concentrations c_α^{p} and c_β^{p}, needed for the calculation of Δs^{ions}, can be found as follows:

$$c_\alpha^{\mathrm{p}} = c_\alpha \phi_\alpha / N, \tag{3.46}$$

$$c_\beta^{\mathrm{p}} = c_\beta \phi_\beta / N, \tag{3.47}$$

with c_β given by Equation (3.37).

Now including the dependence on the variables explicitly, the free energy of demixing can be expressed as

$$\begin{aligned}
&\Delta f(c_0, c_\alpha, \phi_0, \phi_\alpha, \phi_\beta) = \\
&\quad \theta(c_0, c_\alpha, \phi_0, \phi_\alpha, \phi_\beta) f^{\mathrm{blob}}(c_\alpha, \phi_\alpha) \\
&\qquad + [1 - \theta(c_0, c_\alpha, \phi_0, \phi_\alpha, \phi_\beta)] f^{\mathrm{blob}}[c_\beta(c_0, c_\alpha, \phi_0, \phi_\alpha, \phi_\beta), \phi_\beta] \\
&\qquad - f^{\mathrm{blob}}(c_0, \phi_0) \\
&\qquad - \Delta s^{\mathrm{ions}}\{c_\alpha^{\mathrm{p}}(c_\alpha, \phi_\alpha), c_\beta^{\mathrm{p}}[c_\beta(c_0, c_\alpha, \phi_0, \phi_\alpha, \phi_\beta), \phi_\beta], \theta(c_0, c_\alpha, \phi_0, \phi_\alpha, \phi_\beta)\}.
\end{aligned} \tag{3.48}$$

For a given global concentration c_0 and blob volume fraction ϕ_0, the coexisting phases can be found by numerically minimizing Equation (3.48) with respect to c_α, ϕ_α, and ϕ_β. Doing this for various concentrations enables the calculation of phase diagrams, while the application of Equation (3.28) allows calculation of the Donnan potential. In our calculations, the global blob volume fraction will be kept constant at $\phi_0 = 0.5$, which represents a 1:1 ratio of polyelectrolyte and uncharged polymer. Changing ϕ_0 to different values would (for $z > 0$) shift the calculated binodal, because this would change θ, which in turn changes the salt expulsion and the associated entropy penalty. The background salt concentration c_{s} is taken to be either 10 mM, which will be named "low" ionic strength, or 50 mM, which will be called "high" or "increased" ionic strength.

3.3 Experimental

The preparation of samples, construction of phase diagrams, and measurement of Donnan potentials [52] were discussed extensively in Chapter 2 and will be briefly recapitulated here.

Samples were prepared by mixing aqueous stock solutions of the uncharged polymer dextran (100 kDa) and the polyelectrolyte gelatin (gelling temperature 8 to 10 °C, 100 kDa) and diluting with Milli-Q water to reach the desired composition. The polymer content of the solutions will be reported as mass fractions. Dextran and gelatin were always mixed in a 1:1 mass ratio and are both polydisperse [60]. The pH was adjusted to vary the charge of gelatin using dilute hydrochloric acid or sodium hydroxide. Potassium chloride was added to a concentration of 50 mM to explore increased ionic strengths. Without the additional salt, the ionic strength of the samples was of the order of 5 to 10 mM as deduced from conductivity measurements. The situation with added KCl will be referred to as "high" or "increased" ionic strength, while the situation without added KCl will be named "low" ionic strength.

Fully phase-separated samples were obtained by centrifuging vortex-mixed solutions overnight at 100–200g. Phase-separating samples typically contained in total 10 to 20 % polymer (by mass). The composition of each phase was determined by measuring the optical rotation at multiple wavelengths using an Anton Paar MCP 500 polarimeter [6, 52], as described in Section 2.3.2. The gelatin-rich phase is denoted α, the dextran-rich phase β. The Donnan potential was measured electrochemically using reference electrodes [51, 52].

The charge of the gelatin was deduced from a titration. For this titration, 1 to 2 g of gelatin was dissolved in approximately 80 mL Milli-Q water and, while modestly stirring, slowly titrated with dilute hydrochloric acid or sodium hydroxide from a buret while measuring the pH (Hanna Instruments pH 210 pH meter, HI 1043B electrode). The precise concentrations of the hydrochloric acid and sodium hydroxide solutions were determined by titration of the primary standards sodium carbonate and potassium hydrogen phthalate, respectively. Blank titrations of pure solvent were subtracted and, assuming a molar mass of 100 kDa, the number of H^+ or OH^- entities added per polymer chain were calculated. Each added H^+ or OH^- is assumed to change the number of charges per chain z by +1 or −1, respectively. As the isoelectric point (pI) of acid-extracted gelatins typically lies in the pH-range 7–9 [44, 61], we assume $z \approx 0$ at pH 7.5, the inflection point of the obtained titration curve. This allows for the calculation of the absolute number of charges as a function of pH. While this approach may neglect effects such as ion condensation, it does provide an upper bound to the charge of gelatin.

3.4 Results

In this section, first the results of the titration of the polyelectrolyte gelatin will be described. Then, experimentally measured phase diagrams will be compared with calculated phase diagrams. From the phase diagrams, the total polymer mass fraction at the critical point and the distribution of water between the phases as a function of polyelectrolyte charge will be deduced. Finally, the experimentally measured Donnan potentials from Chapter 2 will be compared to the calculated Donnan potentials.

The charge of the polyelectrolyte gelatin as a function of pH, as deduced from titration, is shown in Figure 3.1, where it is assumed that the pI of gelatin is located at pH 7.5. The titration curve is fairly flat in the region of pH 6.5 to 8.5, thus the number of charges z obtained from the titration is not very sensitive to the precise choice of the pI. Additionally, this indicates that not many of the chargeable groups have a pK_a of around 7.5, in line with the amino acid composition of gelatin [62]. Outside this region, the number of charges increases more rapidly. However, given the degree of polymerization $N \approx 1000$, even for $z = +20$ (pH 4.8) only roughly 2 % of the monomers are charged, which still is a low charge density. The pH values at which the phase behavior of our system was studied experimentally are given in Table 3.2, together with the number of charges per gelatin chain derived from titration.

Measured and calculated phase diagrams are shown in Figure 3.2 for various values of z. It is evident from both that, the larger the absolute number of charges $|z|$ is, the further the coexistence line is shifted away from the origin. For small z, only

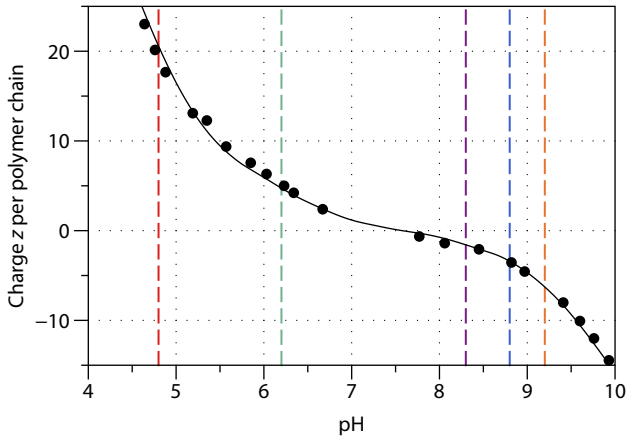

Figure 3.1: Charge of gelatin as derived from titration. The number of charges per polymer chain z was taken to be zero at pH 7.5. The solid line is a guide for the eye. The dashed vertical lines indicate the experimentally studied pH values, for which the charges are listed in Table 3.2.

Table 3.2: Charge of gelatin as derived from titration at the experimentally studied pH values.

pH	charge z
4.8	+20
6.2	+5
8.3	−1.6
8.8	−3.5
9.2	−6

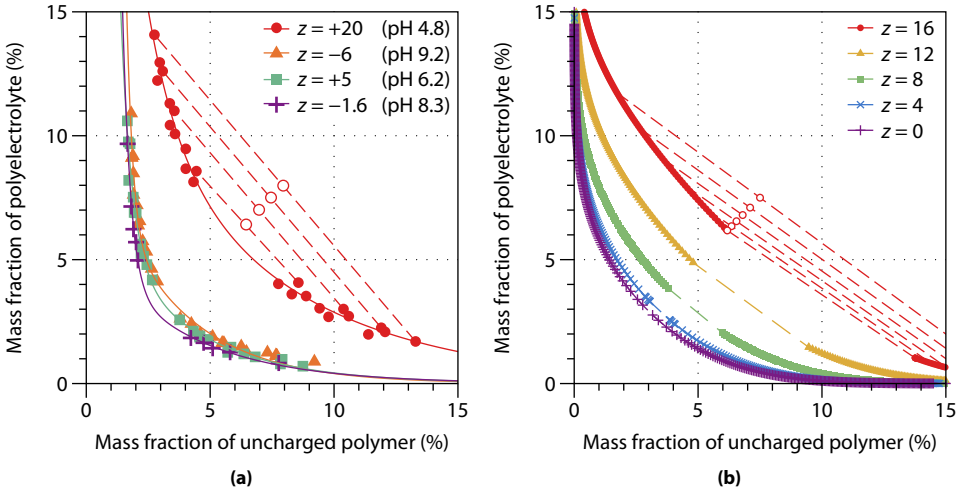

Figure 3.2: (a) Experimentally and (b) theoretically ($\phi_0 = 0.5$) determined phase diagrams at low ionic strength (5 to 10 mM for experiments, 10 mM for calculations). The solid lines are a guide to the eye. The open circles denote a few initial compositions, with the tie lines drawn as dashed lines.

a minor shift in the binodal is observed, whereas for $z \gtrsim 8$ the shift becomes much more pronounced. In the calculations, the shift of the binodal with z is solely due to the effects of ion entropy. The calculations also show a strong asymmetry in the phase diagram for higher z, but this is not seen as clearly in the experiments. Additionally, for higher z, the calculations show a "gap" in the binodal, which is not seen in the experiments. The gap originates from the fact that at higher z, the critical value ϕ_{crit} of the polyelectrolyte blob volume fraction is no longer equal to the global value $\phi_0 = 0.5$. Since changing ϕ_0 leads to a significant shift in the binodal for higher z, we choose to maintain $\phi_0 = 0.5$ in our calculations. (See Appendix A for calculations with different values of ϕ_0.) This will be addressed in more detail in the discussion.

On the basis of the phase diagrams, the total polymer mass fraction at the critical point can be obtained. For experimental phase diagrams, a straight line is fitted through the midpoints of the tie lines and a smooth curve (using the sum of two exponentials) is fitted through the coexisting points forming the binodal. Finally, the total mass fraction at the critical point is given by the intersection of the two. For the theory, the total mass fraction at the critical point is defined as the lowest total mass fraction where demixing into two phases decreased the free energy given the set values of z, c_s, and ϕ_0. The resulting critical mass fractions are plotted in Figure 3.3 as a function of $|z|$ for low and high ionic strength. The experiments and theory show very similar trends: at low ionic strength, the critical point depends strongly on $|z|$, whereas at increased ionic strength this dependence is suppressed.

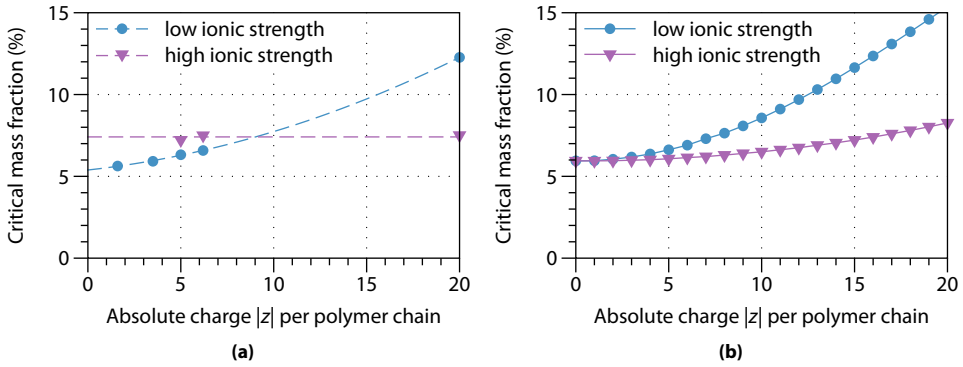

Figure 3.3: Total mass fraction at the critical point of demixing at low ionic strength (5 to 10 mM for experiments, 10 mM for calculations) and high ionic strength (50 mM additional KCl for experiments, 50 mM salt for calculations) as a function of the absolute charge $|z|$ as derived from (a) experimentally measured and (b) theoretically calculated phase diagrams. The dashed lines are a guide to the eye.

The phase diagrams also inform about the distribution of solvent between the two phases. In the calculations, for $z = 0$ the total concentration of polymer in phase α and β is the same, so that also the amount of solvent in the two phases is the same. For $z > 0$, the solvent starts to distribute unevenly across the two phases. In the experiments, the solvent content of the two phases is different close to the pI of the polyelectrolyte, owing to slightly different solvent affinities of the two polymers, and the solvent distribution changes when moving further away from the pI.

In order to quantify and compare this, we define the water uptake $\Delta_{\text{water}}(L, z)$ as the amount of water gained by the polyelectrolyte-rich phase at fixed tie-line length L with respect to a reference situation. The tie-line length, reported as a mass fraction,

is defined as

$$L \equiv \sqrt{(w_\alpha^{\mathrm{p}} - w_\beta^{\mathrm{p}})^2 + (w_\alpha^{\mathrm{u}} - w_\beta^{\mathrm{u}})^2}, \tag{3.49}$$

with w_j^k the mass fraction of polyelectrolyte (p) or uncharged polymer (u) in phase α or β.

First, the difference in the total polymer mass fractions between two phases is calculated using $\Delta w \equiv w_\alpha - w_\beta$, where w_α and w_β are the total polymer mass fractions in the two phases. The water uptake Δ_{water} is then defined as $\Delta_{\mathrm{water}} \equiv -[\Delta w(L, z) - \Delta w_{\mathrm{ref}}(L, z_{\mathrm{ref}})]$. Here, $\Delta w_{\mathrm{ref}}(L, z_{\mathrm{ref}})$ is a function given by a linear fit through the origin of $\Delta w(L, z_{\mathrm{ref}})$ versus L. For the theory, $z_{\mathrm{ref}} = 0$. As the theoretical phase behavior is perfectly symmetrical for $z = 0$, $\Delta w_{\mathrm{ref}}(L, z_{\mathrm{ref}}) = 0$. Experimentally, the phase behavior is not perfectly symmetrical close to the pI, but by taking $z_{\mathrm{ref}} = -1.6$ (pH 8.3, the lowest experimentally studied absolute charge), we correct for this and can still visualize the net effect of charge on the uptake of water.

The water uptake calculated in this way is shown in Figure 3.4 for a low ionic strength. Indeed, both in experiments and theory, the polyelectrolyte-rich phase takes up more water as the absolute charge on the polyelectrolyte is increased. At high ionic strength, this effect would disappear again (not shown).

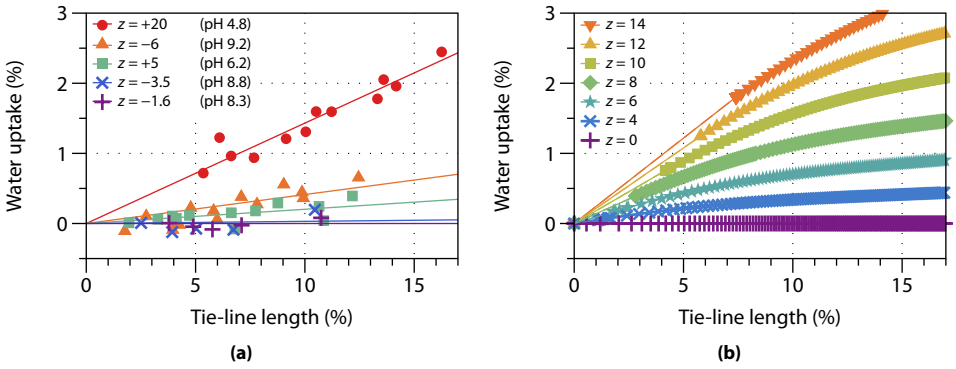

Figure 3.4: Mass fraction of water taken up by the gelatin-rich phase as a function of the tie-line length for various charges z at low ionic strength (5 to 10 mM for experiments, 10 mM for calculations). (a) Experimentally measured water uptake with respect to the situation at $z = -1.6$ (pH 8.3). (b) Theoretically calculated uptake of water.

Additionally, our theory also provides Donnan potentials, which can be compared with the experimentally measured Donnan potentials from Chapter 2 [52]. Experimental and theoretical Donnan potentials are shown in Figure 3.5. Again, experiment and theory follow the same trend, but the precise values are clearly different.

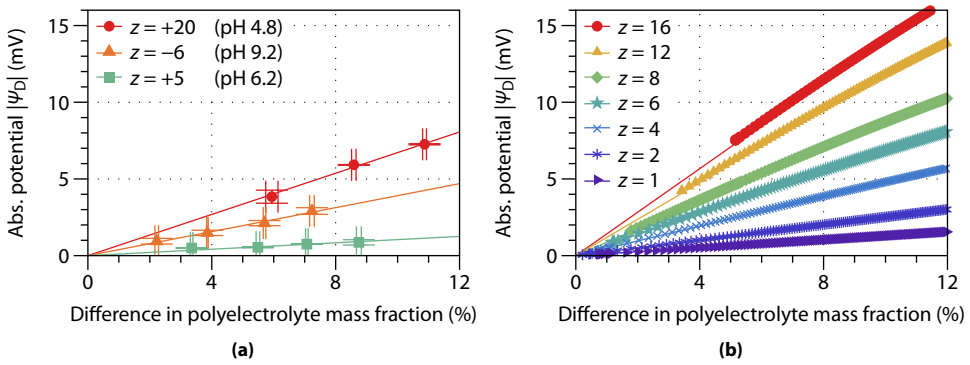

Figure 3.5: Absolute Donnan potential $|\psi_D|$ at low ionic strength (5 to 10 mM for experiments, 10 mM for calculations) as a function of the difference in the polyelectrolyte mass fraction for various polyelectrolyte charges z, (a) measured experimentally [52] and (b) calculated theoretically. The solid lines are a fit to Equation (3.31).

3.5 Discussion

The detailed measurements of the phase diagrams of our experimental system presented in the previous section allow us to pursue a quantitative comparison with our calculations, in order to gain a deeper fundamental insight into the effect of charge and salt on the behavior of mixtures of polyelectrolyte and neutral polymer in solution.

Our theoretical description consists of the blob model to describe the behavior of polymer mixtures in solution, which is combined with the entropy of ideally behaving ions under the restriction of charge neutrality. The latter results in an entropic penalty upon phase separation not for just the counterions, but for all small ions in the system. This entropic penalty can be calculated analytically together with the salt distribution in the system, accounting for the finite size of the system by conserving the number of ions in the system.

The theoretical model describes the trends seen experimentally rather well. The trends in the mass fraction at the critical point, the uptake of water by the polyelectrolyte-rich phase, and the Donnan potentials as a function of charge and ionic strength are certainly captured qualitatively, although there are quantitative differences.

In all cases, the effects predicted by theory are larger than observed in experiments. For instance, theory predicts a larger increase of the mass fraction at the critical point upon an increase in z than observed experimentally, which may in part be attributed to ion condensation at the polyelectrolyte, reducing its effective charge.

Another intriguing effect seen in the experiments is that, for low z, an increase in the *ionic strength* actually increases the total polymer mass fraction at the critical point,

as evident from Figure 3.3a. This can be attributed to a change in the solvent quality (e.g., polarity) for the polymers, leading ultimately to slightly different interactions between the polymers. Our theory supposes a charge- and salt-independent interaction between the polymers.

The redistribution of solvent between the two phases upon an increase of the polyelectrolyte charge can be regarded as a manifestation of the osmotic pressure due to the Donnan equilibrium [41]. The higher total concentration of ions in the polyelectrolyte-rich phase causes osmosis of water to this phase, decreasing the difference in the ion concentrations. However, this process causes a difference in the total polymer concentrations of the two phases and, in equilibrium, the Donnan pressure is balanced by an opposite osmotic pressure due to unequal polymer concentrations.

The theoretical phase diagram shows a "gap" in the binodal for higher values of z. An explanation for this is that the global ratio between polyelectrolyte and neutral polymer is not the same as their ratio in the critical point for set values of z, c_s, and ϕ_0. Therefore, the initial compositions do not intersect the binodal in the critical point and a gap in the binodal results. For $z = 0$, there is a 1:1 ratio of polyelectrolyte and neutral polymer (i.e., $\phi = ½$) in the critical point, which is equal to the global ratio used, enabling us to calculate the complete binodal. However, for $z > 0$, this ratio appears to be different at the critical point, so that we cannot calculate the complete binodal as we maintain a 1:1 ratio of polyelectrolyte and neutral polymer. The latter is important, because changing this ratio also changes the relative volumes of the phases. For $z > 0$, this change in volume would result in a change in the distribution and entropy of the ions, and therefore shift the complete binodal to different concentrations (see Appendix A). It is interesting to note that these effects of charge resemble those of polydispersity, which also results in a dependence of the binodal on the global ratio between the two polymers [63]. Experimentally, gaps in the binodal have not been observed directly and may even be masked by the polydispersity. However, it was observed experimentally that short tie-line lengths were inaccessible at high z. This is evidenced by Figure 3.4a, where the shortest tie-line lengths are around 2 % at low z and at 5 % for the highest z.

Our calculations assume that the blob size ξ depends only on concentration and not directly on charge, which is a simplification [64], especially because the Debye length κ^{-1} is similar to the blob size ξ and electrostatic interactions between blobs are therefore not screened. However, given the very low charge densities in our system, we expect our model to be relatively unaffected by this. Further assumptions in our theory include that the polymers are identical in their uncharged state, except for their interaction with one another, and that they are monodisperse, while in fact both dextran and gelatin are highly polydisperse. Polydispersity will affect at least the

shape of the phase diagram, because of the presence of low molar mass material that does not 'participate' in phase separation. Ions are assumed to behave ideally and ion condensation is neglected. It is also assumed that at the isoelectric point the gelatin is completely free of charges, while in fact there are just equal amounts of positive and negative charges, giving rise to counterions.

A relatively large difference is observed between the calculated and measured Donnan potentials. The experimental Donnan potentials may be affected by an unequal preference of the cations and anions from the background salt for the two phases. This does not mean that the measured Donnan potentials are wrong; rather, this specific effect is not taken into account theoretically. Part of these differences may also be attributed to the fundamental difficulties encountered in measuring Donnan potentials [52], such as due to the liquid junction and streaming potentials, and to uncertainties of the gelatin charge obtained from titration.

Yet, despite our assumptions and simplifications, the theory captures the essential features of the experiments quite well, illustrating the dominant effect of ion entropy on the behavior of mixtures of polyelectrolytes and neutral polymers in solution. Furthermore, both in theory and experiment, the pH-dependent critical point, water uptake, and Donnan potential all appear to be minimal near the isoelectric point of the polyelectrolyte, underlining their common origin.

3.6 Conclusions

The physical behavior of aqueous mixtures of charged and uncharged polymer not only depends on the chemistry of the polymers, but also on their charge. The Donnan equilibrium leads to an inhomogeneous distribution of salt over the two phases, which is entropically unfavorable for both co- and counterions. An increase in the polyelectrolyte charge leads therefore to an increased critical demixing concentration, an uptake of water by the polyelectrolyte-rich phase, and an electric potential difference at the interface. An increase in the ionic strength weakens the relative differences in the salt concentration, and therefore it diminishes the entropic penalty of ion redistribution upon phase separation and shifts behavior towards that of two uncharged polymers. Our combination of the blob model, to describe the interactions of polymers in solution, and maximized ion entropy of the phase-separated system, to take into account charge effects, works well in reproducing experiments.

APPENDIX A

Dependence of Phase Behavior on Concentration Ratio between Polyelectrolyte and Neutral Polymer

Phase diagrams as a function of the global polyelectrolyte blob volume fraction ϕ_0 are shown in Figure A.1 for $z = 0$ and $z = 16$. For $z = 0$, the binodals with $\phi_0 = 0.5$ and 0.1 overlap, whereas for $z = 16$, the binodals are clearly different for the various values of ϕ_0: for values of ϕ_0 closer to zero, the binodal shifts away from the origin.

For a given z, one can find which value of ϕ_0 corresponds to ϕ_{crit}. For $\phi_0 = \phi_{crit}$ the composition of both coexisting phases should approach the global composition near the critical point. For $z = 16$, this is the case for $\phi_0 = 0.2$ as is evident from Figure A.1b. Phase diagrams can be calculated for $\phi_0 = \phi_{crit}$ by repeating such calculations for various values of z. The resulting phase diagrams are given in Figure A.2.

Based on these phase diagrams, the total polymer mass fractions at the critical point can be extracted. These are given in Figure A.3. Because the binodal is shifted away from the origin upon a decrease of ϕ_0, taking $\phi_0 = \phi_{crit}$ instead of $\phi_0 = 0.5$ increases the total mass fraction at the critical point by an absolute amount of up to 5 % for $z = 20$. This underlines the importance of maintaining a 1:1 ratio of polyelectrolyte and neutral polymer in both our calculations and our experiments.

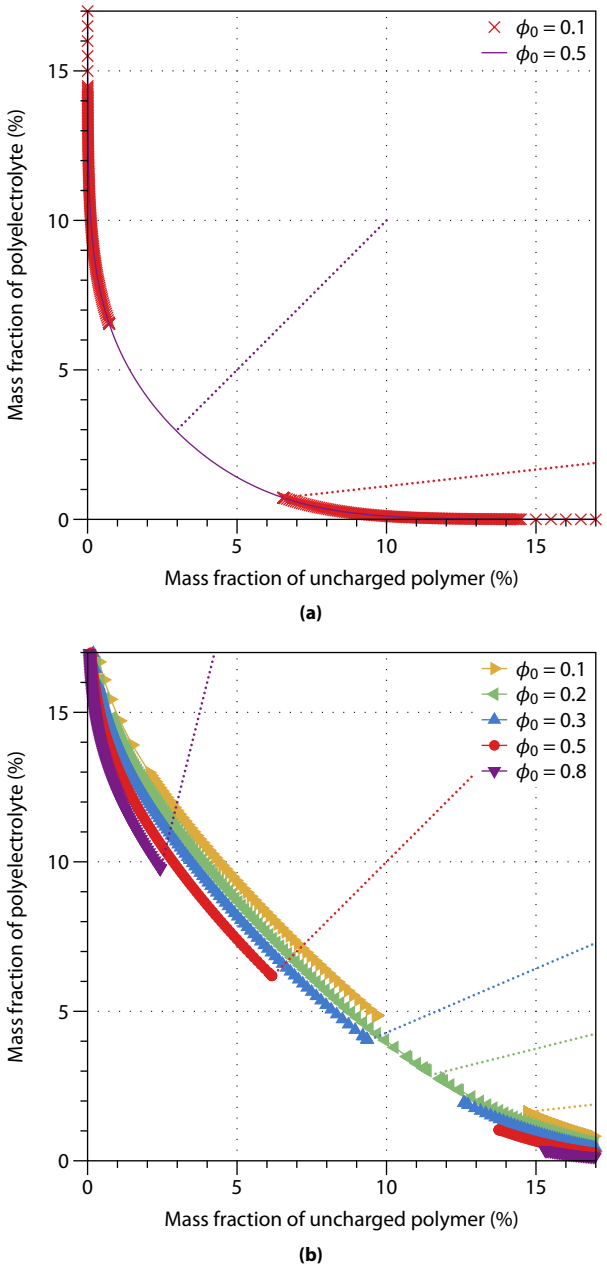

Figure A.1: Calculated phase diagrams for (a) $z = 0$ and (b) $z = 16$ with 10 mM salt, for various global fractions ϕ_0 of polyelectrolyte. The initial compositions lie on the dotted lines.

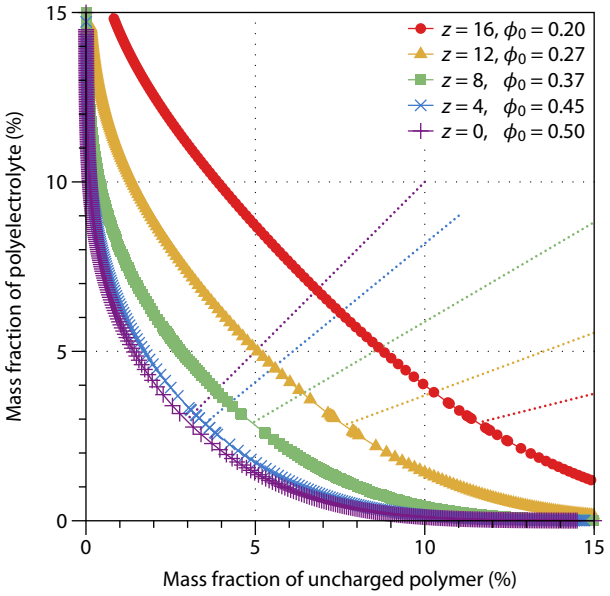

Figure A.2: Calculated phase diagram for various values of z with 10 mM salt. For each value of z the critical polyelectrolyte blob volume fraction ϕ_{crit} was used as the global ϕ_0. The initial compositions lie on the dotted lines.

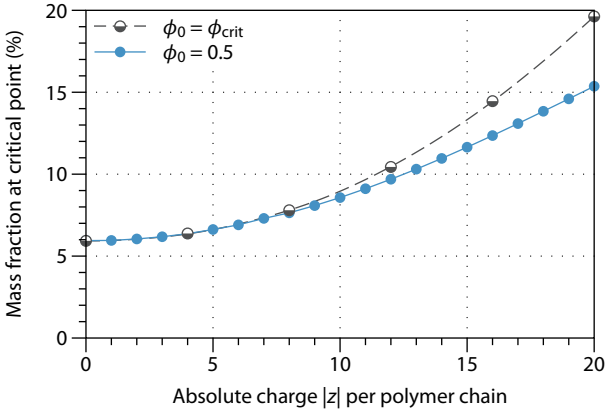

Figure A.3: Comparison between the critical demixing concentrations resulting from the phase diagram calculations with 10 mM salt for $\phi_0 = 0.5$ (Figure 3.2) and $\phi_0 = \phi_{\text{crit}}$ (Figure A.2).

APPENDIX B

Aqueous Densities of Dextran and Gelatin

The density ρ of a solution of a polymer is, assuming additivity of volume, given by

$$\rho = \frac{m_{\text{polymer}} + m_{\text{solvent}}}{V_{\text{polymer}} + V_{\text{solvent}}} \tag{B.1}$$

$$= \frac{m_{\text{polymer}} + m_{\text{solvent}}}{\frac{m_{\text{polymer}}}{\rho_{\text{polymer}}} + \frac{m_{\text{solvent}}}{\rho_{\text{solvent}}}} \tag{B.2}$$

$$= \frac{1}{\frac{w}{\rho_{\text{polymer}}} + \frac{1-w}{\rho_{\text{solvent}}}}, \tag{B.3}$$

where w is the mass fraction of the polymer. This can be rearranged to

$$\rho = \rho_{\text{solvent}} + w\rho\left(1 - \frac{\rho_{\text{solvent}}}{\rho_{\text{polymer}}}\right). \tag{B.4}$$

Thus, by measuring the densities of solutions of a polymer of known mass fraction, the density of the polymer can be extracted from a plot of ρ vs. $w\rho$. The slope of such a plot gives $1 - \rho_{\text{solvent}}/\rho_{\text{polymer}}$ and the y-intercept gives ρ_{solvent}.

Such measurements are shown in Figure B.1 for dextran and gelatin, with the results from the analysis displayed in Table B.1. The measurements show excellent linearity, even for mass fractions of 10 %.

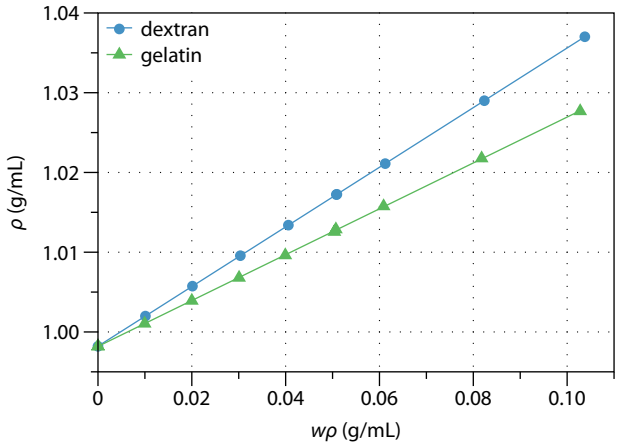

Figure B.1: Measured densities of aqueous solutions of dextran and gelatin. The solid lines are a fit to Equation (B.4) and the results of the fit are displayed in Table B.1.

Table B.1: Results from the fits in Figure B.1, showing the aqueous densities of dextran and gelatin.

	$\left(1-\frac{\rho_{\text{solvent}}}{\rho_{\text{polymer}}}\right)$	ρ_{solvent} (g/mL)	ρ_{polymer} (g/mL)
dextran	0.37397 ± 0.00008	0.998211 ± 0.000005	1.59451 ± 0.00021
gelatin	0.2876 ± 0.0007	0.99819 ± 0.00003	1.4011 ± 0.0013

APPENDIX C

Conversion between Mass Fraction and Monomer Concentration

Experimentally, a convenient measure for concentration is the polymer mass fraction w. For calculating back and forth between mass fractions and monomer concentrations (number per unit volume), additional expressions are needed. c is calculated from w as

$$c(w) = \frac{w\rho(w)N_A}{M_{w,monomer}}, \tag{C.1}$$

where N_A is Avogadro's number and $\rho(w)$ the mass density of a polymer solution of mass fraction w, given by Equation (B.3).

In order to convert back from monomer concentrations to mass fractions, the following expressions can be shown to hold:

$$w(c) = \frac{cM_{w,monomer}}{\rho(c)N_A}, \tag{C.2}$$

$$\rho(c) = \rho_{solvent}\left(1 - \frac{cM_{w,monomer}}{\rho_{polymer}N_A}\right) + \frac{cM_{w,monomer}}{N_A}. \tag{C.3}$$

It can be shown that $c[w(c)] = c$ and $w[c(w)] = w$. In other words, the expressions are self-consistent.

APPENDIX D

Additional Expressions regarding the Donnan Equilibrium

D.1 General Expression for Change in Ion Entropy

An alternative form for the change in ion entropy upon demixing is given by

$$\begin{aligned}\Delta s^{\text{ions}} = {} & (c_{\text{s}}\theta - c_{\text{ex}}) \ln\left(\frac{c_{\text{s}}}{c_{\text{s}} - \frac{c_{\text{ex}}}{\theta}} \right) \\ & + (c_{\text{s}}\theta + z c_0^{\text{P}} \eta^{\text{P}} - c_{\text{ex}}) \ln\left(\frac{c_{\text{s}} + z c_0^{\text{P}}}{c_{\text{s}} + \frac{z c_0^{\text{P}} \eta^{\text{P}} - c_{\text{ex}}}{\theta}} \right) \\ & + [c_{\text{s}}(1-\theta) + c_{\text{ex}}] \ln\left(\frac{c_{\text{s}}}{c_{\text{s}} + \frac{c_{\text{ex}}}{1-\theta}} \right) \\ & + [c_{\text{s}}(1-\theta) + z c_0^{\text{P}}(1-\eta^{\text{P}}) + c_{\text{ex}}] \ln\left[\frac{c_{\text{s}} + z c_0^{\text{P}}}{c_{\text{s}} + \frac{z c_0^{\text{P}}(1-\eta^{\text{P}}) + c_{\text{ex}}}{1-\theta}} \right],\end{aligned} \tag{D.1}$$

where $\eta^{\text{P}} \equiv n_\alpha^{\text{P}} / (n_\alpha^{\text{P}} + n_\beta^{\text{P}}) = c_\alpha^{\text{P}} \theta / c_0^{\text{P}}$, with n_j^{P} the number of moles of polyelectrolyte in j.

This form is particularly useful when making approximations under the condition that the total amount of polyelectrolyte remains constant. However, for simplicity, the expressions in Chapter 3 are given in terms of c_α^{P} and c_β^{P}.

D.2 Calculation of Equilibrium Salt Distribution

The equilibrium salt distribution can be found from the derivative of Equation (D.1) to c_{ex}:

$$\begin{aligned}\frac{\partial \Delta s^{\mathrm{ions}}}{\partial c_{\mathrm{ex}}} = &- \ln\left(\frac{c_{\mathrm{s}}}{c_{\mathrm{s}} - \frac{c_{\mathrm{ex}}}{\theta}}\right) - \ln\left(\frac{c_{\mathrm{s}} + z c_0^{\mathrm{P}}}{c_{\mathrm{s}} + \frac{z c_0^{\mathrm{P}} \eta^{\mathrm{P}} - c_{\mathrm{ex}}}{\theta}}\right) \\ &+ \ln\left(\frac{c_{\mathrm{s}}}{c_{\mathrm{s}} + \frac{c_{\mathrm{ex}}}{1-\theta}}\right) + \ln\left[\frac{c_{\mathrm{s}} + z c_0^{\mathrm{P}}}{c_{\mathrm{s}} + \frac{z c_0^{\mathrm{P}}(1-\eta^{\mathrm{P}}) + c_{\mathrm{ex}}}{1-\theta}}\right].\end{aligned} \tag{D.2}$$

This expression is equated to zero to find the equilibrium value for c_{ex}:

$$0 = \frac{\partial \Delta s^{\mathrm{ions}}}{\partial c_{\mathrm{ex}}} \tag{D.3}$$

$$= \ln\left[\frac{c_{\mathrm{s}} - \frac{c_{\mathrm{ex}}}{\theta}}{c_{\mathrm{s}} + \frac{c_{\mathrm{ex}}}{1-\theta}} \frac{c_{\mathrm{s}} + \frac{z c_0^{\mathrm{P}} \eta^{\mathrm{P}} - c_{\mathrm{ex}}}{\theta}}{c_{\mathrm{s}} + \frac{z c_0^{\mathrm{P}}(1-\eta^{\mathrm{P}}) + c_{\mathrm{ex}}}{1-\theta}}\right], \tag{D.4}$$

which, because of the definitions of c_j^i, is equivalent to the law of mass action, i.e., $(c_\alpha^+ c_\alpha^-)/(c_\beta^+ c_\beta^-) = 1$. Provided $\theta \neq ½$, this can be rearranged to an equation quadratic in c_{ex}:

$$\begin{aligned}c_{\mathrm{ex}}^2[(1-\theta)^2 - \theta^2] - c_{\mathrm{ex}}[&2c_{\mathrm{s}}\theta(1-\theta)^2 + z c_0^{\mathrm{P}} \eta^{\mathrm{P}}(1-\theta)^2 + 2c_{\mathrm{s}}\theta^2(1-\theta) \\ &+ z c_0^{\mathrm{P}}(1-\eta^{\mathrm{P}})\theta^2] + z c_0^{\mathrm{P}} c_{\mathrm{s}} \eta^{\mathrm{P}} \theta(1-\theta)^2 - z c_0^{\mathrm{P}} c_{\mathrm{s}}(1-\eta^{\mathrm{P}})\theta^2(1-\theta) = 0,\end{aligned} \tag{D.5}$$

which can be solved analytically:

$$\begin{aligned}c_{\mathrm{ex}} = c_{\mathrm{s}}\theta\frac{1-\theta}{1-2\theta}\Bigg\{&1 + \frac{z c_0^{\mathrm{P}}}{2c_{\mathrm{s}}}\frac{\eta^{\mathrm{P}} - 2\theta\eta^{\mathrm{P}} + \theta^2}{\theta(1-\theta)} \\ &- \sqrt{1 + \frac{z c_0^{\mathrm{P}}}{c_{\mathrm{s}}} + \left[\frac{z c_0^{\mathrm{P}}}{2c_{\mathrm{s}}}\frac{\eta^{\mathrm{P}} - 2\theta\eta^{\mathrm{P}} + \theta^2}{\theta(1-\theta)}\right]^2}\Bigg\},\end{aligned} \tag{D.6}$$

where we have discarded the unphysical root, as for $\eta^{\mathrm{P}} = \theta$ (that is, $c_\alpha^{\mathrm{P}} = c_\beta^{\mathrm{P}}$), c_{ex} must be zero.

There is a special solution for $\theta = ½$, as Equation (D.5) is no longer quadratic in this case. One finds

$$c_{\mathrm{ex}} = -\frac{z c_0^{\mathrm{P}}}{4}\frac{1-2\eta^{\mathrm{P}}}{1 + \frac{z c_0^{\mathrm{P}}}{2c_{\mathrm{s}}}}. \tag{D.7}$$

D.3 Equilibrium Change in Ion Entropy

By substitution of Equation (D.6) into Equation (D.1), one finds the change in ion entropy upon phase separation in terms of c_0^{P} and η^{P} for $\theta \neq ½$:

$$
\begin{aligned}
&\frac{\Delta s^{\mathrm{ions}}}{c_{\mathrm{s}}} = \\
&\theta\left(1-\frac{1-\theta}{1-2\theta}\left\{1+\frac{zc_0^{\mathrm{P}}}{2c_{\mathrm{s}}}\frac{\eta^{\mathrm{P}}-2\theta\eta^{\mathrm{P}}+\theta^2}{\theta(1-\theta)}-\sqrt{1+\frac{zc_0^{\mathrm{P}}}{c_{\mathrm{s}}}+\left[\frac{zc_0^{\mathrm{P}}}{2c_{\mathrm{s}}}\frac{\eta^{\mathrm{P}}-2\theta\eta^{\mathrm{P}}+\theta^2}{\theta(1-\theta)}\right]^2}\right\}\right)\\
&\quad\times\ln\left(\frac{1}{1-\frac{1-\theta}{1-2\theta}\left\{1+\frac{zc_0^{\mathrm{P}}}{2c_{\mathrm{s}}}\frac{\eta^{\mathrm{P}}-2\theta\eta^{\mathrm{P}}+\theta^2}{\theta(1-\theta)}-\sqrt{1+\frac{zc_0^{\mathrm{P}}}{c_{\mathrm{s}}}+\left[\frac{zc_0^{\mathrm{P}}}{2c_{\mathrm{s}}}\frac{\eta^{\mathrm{P}}-2\theta\eta^{\mathrm{P}}+\theta^2}{\theta(1-\theta)}\right]^2}\right\}}\right)\\
&+\theta\left(1+\frac{zc_0^{\mathrm{P}}}{c_{\mathrm{s}}}\frac{\eta^{\mathrm{P}}}{\theta}-\frac{1-\theta}{1-2\theta}\left\{1+\frac{zc_0^{\mathrm{P}}}{2c_{\mathrm{s}}}\frac{\eta^{\mathrm{P}}-2\theta\eta^{\mathrm{P}}+\theta^2}{\theta(1-\theta)}-\sqrt{1+\frac{zc_0^{\mathrm{P}}}{c_{\mathrm{s}}}+\left[\frac{zc_0^{\mathrm{P}}}{2c_{\mathrm{s}}}\frac{\eta^{\mathrm{P}}-2\theta\eta^{\mathrm{P}}+\theta^2}{\theta(1-\theta)}\right]^2}\right\}\right)\\
&\quad\times\ln\left(\frac{1+\frac{zc_0^{\mathrm{P}}}{c_{\mathrm{s}}}}{1+\frac{zc_0^{\mathrm{P}}}{c_{\mathrm{s}}}\frac{\eta^{\mathrm{P}}}{\theta}-\frac{1-\theta}{1-2\theta}\left\{1+\frac{zc_0^{\mathrm{P}}}{2c_{\mathrm{s}}}\frac{\eta^{\mathrm{P}}-2\theta\eta^{\mathrm{P}}+\theta^2}{\theta(1-\theta)}-\sqrt{1+\frac{zc_0^{\mathrm{P}}}{c_{\mathrm{s}}}+\left[\frac{zc_0^{\mathrm{P}}}{2c_{\mathrm{s}}}\frac{\eta^{\mathrm{P}}-2\theta\eta^{\mathrm{P}}+\theta^2}{\theta(1-\theta)}\right]^2}\right\}}\right)\\
&+(1-\theta)\left(1+\frac{\theta}{1-2\theta}\left\{1+\frac{zc_0^{\mathrm{P}}}{2c_{\mathrm{s}}}\frac{\eta^{\mathrm{P}}-2\theta\eta^{\mathrm{P}}+\theta^2}{\theta(1-\theta)}-\sqrt{1+\frac{zc_0^{\mathrm{P}}}{c_{\mathrm{s}}}+\left[\frac{zc_0^{\mathrm{P}}}{2c_{\mathrm{s}}}\frac{\eta^{\mathrm{P}}-2\theta\eta^{\mathrm{P}}+\theta^2}{\theta(1-\theta)}\right]^2}\right\}\right)\\
&\quad\times\ln\left(\frac{1}{1+\frac{\theta}{1-2\theta}\left\{1+\frac{zc_0^{\mathrm{P}}}{2c_{\mathrm{s}}}\frac{\eta^{\mathrm{P}}-2\theta\eta^{\mathrm{P}}+\theta^2}{\theta(1-\theta)}-\sqrt{1+\frac{zc_0^{\mathrm{P}}}{c_{\mathrm{s}}}+\left[\frac{zc_0^{\mathrm{P}}}{2c_{\mathrm{s}}}\frac{\eta^{\mathrm{P}}-2\theta\eta^{\mathrm{P}}+\theta^2}{\theta(1-\theta)}\right]^2}\right\}}\right)\\
&+(1-\theta)\left(1+\frac{zc_0^{\mathrm{P}}}{c_{\mathrm{s}}}\frac{1-\eta^{\mathrm{P}}}{1-\theta}+\frac{\theta}{1-2\theta}\left\{1+\frac{zc_0^{\mathrm{P}}}{2c_{\mathrm{s}}}\frac{\eta^{\mathrm{P}}-2\theta\eta^{\mathrm{P}}+\theta^2}{\theta(1-\theta)}-\sqrt{1+\frac{zc_0^{\mathrm{P}}}{c_{\mathrm{s}}}+\left[\frac{zc_0^{\mathrm{P}}}{2c_{\mathrm{s}}}\frac{\eta^{\mathrm{P}}-2\theta\eta^{\mathrm{P}}+\theta^2}{\theta(1-\theta)}\right]^2}\right\}\right)\\
&\quad\times\ln\left(\frac{1+\frac{zc_0^{\mathrm{P}}}{c_{\mathrm{s}}}}{1+\frac{zc_0^{\mathrm{P}}}{c_{\mathrm{s}}}\frac{1-\eta^{\mathrm{P}}}{1-\theta}+\frac{\theta}{1-2\theta}\left\{1+\frac{zc_0^{\mathrm{P}}}{2c_{\mathrm{s}}}\frac{\eta^{\mathrm{P}}-2\theta\eta^{\mathrm{P}}+\theta^2}{\theta(1-\theta)}-\sqrt{1+\frac{zc_0^{\mathrm{P}}}{c_{\mathrm{s}}}+\left[\frac{zc_0^{\mathrm{P}}}{2c_{\mathrm{s}}}\frac{\eta^{\mathrm{P}}-2\theta\eta^{\mathrm{P}}+\theta^2}{\theta(1-\theta)}\right]^2}\right\}}\right).
\end{aligned}
\tag{D.8}
$$

Using a Taylor approximation in η^{P} around θ,

$$
\Delta s^{\mathrm{ions}} \simeq -\frac{(\theta-\eta^{\mathrm{P}})^2}{2\theta(1-\theta)}\frac{(zc_0^{\mathrm{P}})^2}{2c_{\mathrm{s}}+zc_0^{\mathrm{P}}} \tag{D.9}
$$

$$
= -\frac{\theta(1-\theta)}{2}\frac{(zc_\alpha^{\mathrm{P}}-zc_\beta^{\mathrm{P}})^2}{2c_{\mathrm{s}}+z[c_\alpha^{\mathrm{P}}\theta+c_\beta^{\mathrm{P}}(1-\theta)]}. \tag{D.10}
$$

Equivalently, the change in ion entropy may be found in terms of c_α^{P} and c_β^{P} using Equations (3.19) and (3.21) from Chapter 3:

$$
\begin{aligned}
\frac{\Delta s^{\mathrm{ions}}}{c_{\mathrm{s}}} = \\
&\theta\left[1-\frac{1-\theta}{1-2\theta}\left(1+\frac{z[c_\alpha^{\mathrm{P}}(1-\theta)+c_\beta^{\mathrm{P}}\theta]}{2c_{\mathrm{s}}}-\sqrt{1+\frac{z[c_\alpha^{\mathrm{P}}\theta+c_\beta^{\mathrm{P}}(1-\theta)]}{c_{\mathrm{s}}}+\left\{\frac{z[c_\alpha^{\mathrm{P}}(1-\theta)+c_\beta^{\mathrm{P}}\theta]}{2c_{\mathrm{s}}}\right\}^2}\right)\right] \\
&\quad\times\ln\left[\frac{1}{1-\frac{1-\theta}{1-2\theta}\left(1+\frac{z[c_\alpha^{\mathrm{P}}(1-\theta)+c_\beta^{\mathrm{P}}\theta]}{2c_{\mathrm{s}}}-\sqrt{1+\frac{z[c_\alpha^{\mathrm{P}}\theta+c_\beta^{\mathrm{P}}(1-\theta)]}{c_{\mathrm{s}}}+\left\{\frac{z[c_\alpha^{\mathrm{P}}(1-\theta)+c_\beta^{\mathrm{P}}\theta]}{2c_{\mathrm{s}}}\right\}^2}\right)}\right] \\
&+\theta\left[1+\frac{zc_\alpha^{\mathrm{P}}}{c_{\mathrm{s}}}-\frac{1-\theta}{1-2\theta}\left(1+\frac{z[c_\alpha^{\mathrm{P}}(1-\theta)+c_\beta^{\mathrm{P}}\theta]}{2c_{\mathrm{s}}}-\sqrt{1+\frac{z[c_\alpha^{\mathrm{P}}\theta+c_\beta^{\mathrm{P}}(1-\theta)]}{c_{\mathrm{s}}}+\left\{\frac{z[c_\alpha^{\mathrm{P}}(1-\theta)+c_\beta^{\mathrm{P}}\theta]}{2c_{\mathrm{s}}}\right\}^2}\right)\right] \\
&\quad\times\ln\left[\frac{1+\frac{z[c_\alpha^{\mathrm{P}}\theta+c_\beta^{\mathrm{P}}(1-\theta)]}{c_{\mathrm{s}}}}{1+\frac{zc_\alpha^{\mathrm{P}}}{c_{\mathrm{s}}}-\frac{1-\theta}{1-2\theta}\left(1+\frac{z[c_\alpha^{\mathrm{P}}(1-\theta)+c_\beta^{\mathrm{P}}\theta]}{2c_{\mathrm{s}}}-\sqrt{1+\frac{z[c_\alpha^{\mathrm{P}}\theta+c_\beta^{\mathrm{P}}(1-\theta)]}{c_{\mathrm{s}}}+\left\{\frac{z[c_\alpha^{\mathrm{P}}(1-\theta)+c_\beta^{\mathrm{P}}\theta]}{2c_{\mathrm{s}}}\right\}^2}\right)}\right] \\
&+(1-\theta)\left[1+\frac{\theta}{1-2\theta}\left(1+\frac{z[c_\alpha^{\mathrm{P}}(1-\theta)+c_\beta^{\mathrm{P}}\theta]}{2c_{\mathrm{s}}}-\sqrt{1+\frac{z[c_\alpha^{\mathrm{P}}\theta+c_\beta^{\mathrm{P}}(1-\theta)]}{c_{\mathrm{s}}}+\left\{\frac{z[c_\alpha^{\mathrm{P}}(1-\theta)+c_\beta^{\mathrm{P}}\theta]}{2c_{\mathrm{s}}}\right\}^2}\right)\right] \\
&\quad\times\ln\left[\frac{1}{1+\frac{\theta}{1-2\theta}\left(1+\frac{z[c_\alpha^{\mathrm{P}}(1-\theta)+c_\beta^{\mathrm{P}}\theta]}{2c_{\mathrm{s}}}-\sqrt{1+\frac{z[c_\alpha^{\mathrm{P}}\theta+c_\beta^{\mathrm{P}}(1-\theta)]}{c_{\mathrm{s}}}+\left\{\frac{z[c_\alpha^{\mathrm{P}}(1-\theta)+c_\beta^{\mathrm{P}}\theta]}{2c_{\mathrm{s}}}\right\}^2}\right)}\right] \\
&+(1-\theta)\left[1+\frac{zc_\beta^{\mathrm{P}}}{c_{\mathrm{s}}}+\frac{\theta}{1-2\theta}\left(1+\frac{z[c_\alpha^{\mathrm{P}}(1-\theta)+c_\beta^{\mathrm{P}}\theta]}{2c_{\mathrm{s}}}-\sqrt{1+\frac{z[c_\alpha^{\mathrm{P}}\theta+c_\beta^{\mathrm{P}}(1-\theta)]}{c_{\mathrm{s}}}+\left\{\frac{z[c_\alpha^{\mathrm{P}}(1-\theta)+c_\beta^{\mathrm{P}}\theta]}{2c_{\mathrm{s}}}\right\}^2}\right)\right] \\
&\quad\times\ln\left[\frac{1+\frac{z[c_\alpha^{\mathrm{P}}\theta+c_\beta^{\mathrm{P}}(1-\theta)]}{c_{\mathrm{s}}}}{1+\frac{zc_\beta^{\mathrm{P}}}{c_{\mathrm{s}}}+\frac{\theta}{1-2\theta}\left(1+\frac{z[c_\alpha^{\mathrm{P}}(1-\theta)+c_\beta^{\mathrm{P}}\theta]}{2c_{\mathrm{s}}}-\sqrt{1+\frac{z[c_\alpha^{\mathrm{P}}\theta+c_\beta^{\mathrm{P}}(1-\theta)]}{c_{\mathrm{s}}}+\left\{\frac{z[c_\alpha^{\mathrm{P}}(1-\theta)+c_\beta^{\mathrm{P}}\theta]}{2c_{\mathrm{s}}}\right\}^2}\right)}\right].
\end{aligned}
\tag{D.11}
$$

The change in ion entropy may also be expressed in terms of the charge density ratios $y_\alpha \equiv z c_\alpha^{\mathrm{p}}/c_{\mathrm{s}}$ and $y_\beta \equiv z c_\beta^{\mathrm{p}}/c_{\mathrm{s}}$. The result is

$$
\begin{aligned}
&\frac{\Delta s^{\mathrm{ions}}}{c_{\mathrm{s}}} = \\
&\theta\left(1-\frac{1-\theta}{1-2\theta}\left\{1+\frac{y_\alpha}{2}(1-\theta)+\frac{y_\beta}{2}\theta-\sqrt{1+y_\alpha\theta+y_\beta(1-\theta)+\left[\frac{y_\alpha}{2}(1-\theta)+\frac{y_\beta}{2}\theta\right]^2}\right\}\right)\\
&\quad\times\ln\left(\frac{1}{1-\frac{1-\theta}{1-2\theta}\left\{1+\frac{y_\alpha}{2}(1-\theta)+\frac{y_\beta}{2}\theta-\sqrt{1+y_\alpha\theta+y_\beta(1-\theta)+\left[\frac{y_\alpha}{2}(1-\theta)+\frac{y_\beta}{2}\theta\right]^2}\right\}}\right)\\
&+\theta\left(1+y_\alpha-\frac{1-\theta}{1-2\theta}\left\{1+\frac{y_\alpha}{2}(1-\theta)+\frac{y_\beta}{2}\theta-\sqrt{1+y_\alpha\theta+y_\beta(1-\theta)+\left[\frac{y_\alpha}{2}(1-\theta)+\frac{y_\beta}{2}\theta\right]^2}\right\}\right)\\
&\quad\times\ln\left(\frac{1+y_\alpha\theta+y_\beta(1-\theta)}{1+y_\alpha-\frac{1-\theta}{1-2\theta}\left\{1+\frac{y_\alpha}{2}(1-\theta)+\frac{y_\beta}{2}\theta-\sqrt{1+y_\alpha\theta+y_\beta(1-\theta)+\left[\frac{y_\alpha}{2}(1-\theta)+\frac{y_\beta}{2}\theta\right]^2}\right\}}\right)\\
&+(1-\theta)\left(1+\frac{\theta}{1-2\theta}\left\{1+\frac{y_\alpha}{2}(1-\theta)+\frac{y_\beta}{2}\theta-\sqrt{1+y_\alpha\theta+y_\beta(1-\theta)+\left[\frac{y_\alpha}{2}(1-\theta)+\frac{y_\beta}{2}\theta\right]^2}\right\}\right)\\
&\quad\times\ln\left(\frac{1}{1+\frac{\theta}{1-2\theta}\left\{1+\frac{y_\alpha}{2}(1-\theta)+\frac{y_\beta}{2}\theta-\sqrt{1+y_\alpha\theta+y_\beta(1-\theta)+\left[\frac{y_\alpha}{2}(1-\theta)+\frac{y_\beta}{2}\theta\right]^2}\right\}}\right)\\
&+(1-\theta)\left(1+y_\beta+\frac{\theta}{1-2\theta}\left\{1+\frac{y_\alpha}{2}(1-\theta)+\frac{y_\beta}{2}\theta-\sqrt{1+y_\alpha\theta+y_\beta(1-\theta)+\left[\frac{y_\alpha}{2}(1-\theta)+\frac{y_\beta}{2}\theta\right]^2}\right\}\right)\\
&\quad\times\ln\left(\frac{1+y_\alpha\theta+y_\beta(1-\theta)}{1+y_\beta+\frac{\theta}{1-2\theta}\left\{1+\frac{y_\alpha}{2}(1-\theta)+\frac{y_\beta}{2}\theta-\sqrt{1+y_\alpha\theta+y_\beta(1-\theta)+\left[\frac{y_\alpha}{2}(1-\theta)+\frac{y_\beta}{2}\theta\right]^2}\right\}}\right),
\end{aligned}
\tag{D.12}
$$

which shows clearly that only the ratio between the concentration of counterions and background salt is relevant.

Equations (D.8) to (D.12) are only determinate for $\theta \neq ½$. For the situation where θ exactly equals ½, Equation (D.1) is combined with Equation (D.7) to yield the change in ion entropy in terms of c_0^{P} and η^{P}:

$$\begin{aligned}\frac{\Delta s^{\mathrm{ions}}}{c_{\mathrm{s}}} = &\frac{1}{2}\left(1+\frac{zc_0^{\mathrm{P}}}{2c_{\mathrm{s}}}\frac{1-2\eta^{\mathrm{P}}}{1+\frac{zc_0^{\mathrm{P}}}{2c_{\mathrm{s}}}}\right)\ln\left(\frac{1}{1+\frac{zc_0^{\mathrm{P}}}{2c_{\mathrm{s}}}\frac{1-2\eta^{\mathrm{P}}}{1+\frac{zc_0^{\mathrm{P}}}{2c_{\mathrm{s}}}}}\right)\\ &+\frac{1}{2}\left(1+\frac{zc_0^{\mathrm{P}}}{c_{\mathrm{s}}}2\eta^{\mathrm{P}}+\frac{zc_0^{\mathrm{P}}}{2c_{\mathrm{s}}}\frac{1-2\eta^{\mathrm{P}}}{1+\frac{zc_0^{\mathrm{P}}}{2c_{\mathrm{s}}}}\right)\ln\left(\frac{1+\frac{zc_0^{\mathrm{P}}}{c_{\mathrm{s}}}}{1+\frac{zc_0^{\mathrm{P}}}{c_{\mathrm{s}}}2\eta^{\mathrm{P}}+\frac{zc_0^{\mathrm{P}}}{2c_{\mathrm{s}}}\frac{1-2\eta^{\mathrm{P}}}{1+\frac{zc_0^{\mathrm{P}}}{2c_{\mathrm{s}}}}}\right)\\ &+\frac{1}{2}\left(1-\frac{zc_0^{\mathrm{P}}}{2c_{\mathrm{s}}}\frac{1-2\eta^{\mathrm{P}}}{1+\frac{zc_0^{\mathrm{P}}}{2c_{\mathrm{s}}}}\right)\ln\left(\frac{1}{1-\frac{zc_0^{\mathrm{P}}}{2c_{\mathrm{s}}}\frac{1-2\eta^{\mathrm{P}}}{1+\frac{zc_0^{\mathrm{P}}}{2c_{\mathrm{s}}}}}\right)\\ &+\frac{1}{2}\left[1+\frac{zc_0^{\mathrm{P}}}{c_{\mathrm{s}}}2(1-\eta^{\mathrm{P}})-\frac{zc_0^{\mathrm{P}}}{2c_{\mathrm{s}}}\frac{1-2\eta^{\mathrm{P}}}{1+\frac{zc_0^{\mathrm{P}}}{2c_{\mathrm{s}}}}\right]\ln\left[\frac{1+\frac{zc_0^{\mathrm{P}}}{c_{\mathrm{s}}}}{1+\frac{zc_0^{\mathrm{P}}}{c_{\mathrm{s}}}2(1-\eta^{\mathrm{P}})-\frac{zc_0^{\mathrm{P}}}{2c_{\mathrm{s}}}\frac{1-2\eta^{\mathrm{P}}}{1+\frac{zc_0^{\mathrm{P}}}{2c_{\mathrm{s}}}}}\right].\end{aligned} \tag{D.13}$$

Equivalently, the change in ion entropy may be expressed in terms of the explicit polyelectrolyte concentration in each phase, c_α^{P} and c_β^{P}. This form is obtained by combining Equations (3.19) and (3.22) from Chapter 3:

$$\begin{aligned}\frac{\Delta s^{\mathrm{ions}}}{c_{\mathrm{s}}} = &\frac{1}{2}\left[1-\frac{z(c_\alpha^{\mathrm{P}}-c_\beta^{\mathrm{P}})}{2c_{\mathrm{s}}}\frac{1}{2+\frac{z(c_\alpha^{\mathrm{P}}+c_\beta^{\mathrm{P}})}{2c_{\mathrm{s}}}}\right]\ln\left[\frac{1}{1-\frac{z(c_\alpha^{\mathrm{P}}-c_\beta^{\mathrm{P}})}{2c_{\mathrm{s}}}\frac{1}{2+\frac{z(c_\alpha^{\mathrm{P}}+c_\beta^{\mathrm{P}})}{2c_{\mathrm{s}}}}}\right]\\ &+\frac{1}{2}\left[1+\frac{zc_\alpha^{\mathrm{P}}}{c_{\mathrm{s}}}-\frac{z(c_\alpha^{\mathrm{P}}-c_\beta^{\mathrm{P}})}{2c_{\mathrm{s}}}\frac{1}{2+\frac{z(c_\alpha^{\mathrm{P}}+c_\beta^{\mathrm{P}})}{2c_{\mathrm{s}}}}\right]\ln\left[\frac{1+\frac{z(c_\alpha^{\mathrm{P}}+c_\beta^{\mathrm{P}})}{2c_{\mathrm{s}}}}{1+\frac{zc_\alpha^{\mathrm{P}}}{c_{\mathrm{s}}}-\frac{z(c_\alpha^{\mathrm{P}}-c_\beta^{\mathrm{P}})}{2c_{\mathrm{s}}}\frac{1}{2+\frac{z(c_\alpha^{\mathrm{P}}+c_\beta^{\mathrm{P}})}{2c_{\mathrm{s}}}}}\right]\\ &+\frac{1}{2}\left[1+\frac{z(c_\alpha^{\mathrm{P}}-c_\beta^{\mathrm{P}})}{2c_{\mathrm{s}}}\frac{1}{2+\frac{z(c_\alpha^{\mathrm{P}}+c_\beta^{\mathrm{P}})}{2c_{\mathrm{s}}}}\right]\ln\left[\frac{1}{1+\frac{z(c_\alpha^{\mathrm{P}}-c_\beta^{\mathrm{P}})}{2c_{\mathrm{s}}}\frac{1}{2+\frac{z(c_\alpha^{\mathrm{P}}+c_\beta^{\mathrm{P}})}{2c_{\mathrm{s}}}}}\right]\\ &+\frac{1}{2}\left[1+\frac{zc_\beta^{\mathrm{P}}}{c_{\mathrm{s}}}+\frac{z(c_\alpha^{\mathrm{P}}-c_\beta^{\mathrm{P}})}{2c_{\mathrm{s}}}\frac{1}{2+\frac{z(c_\alpha^{\mathrm{P}}+c_\beta^{\mathrm{P}})}{2c_{\mathrm{s}}}}\right]\ln\left[\frac{1+\frac{z(c_\alpha^{\mathrm{P}}+c_\beta^{\mathrm{P}})}{2c_{\mathrm{s}}}}{1+\frac{zc_\beta^{\mathrm{P}}}{c_{\mathrm{s}}}+\frac{z(c_\alpha^{\mathrm{P}}-c_\beta^{\mathrm{P}})}{2c_{\mathrm{s}}}\frac{1}{2+\frac{z(c_\alpha^{\mathrm{P}}+c_\beta^{\mathrm{P}})}{2c_{\mathrm{s}}}}}\right].\end{aligned} \tag{D.14}$$

Or, in terms of the charge density ratios y_α and y_β:

$$\begin{aligned}\frac{\Delta s^{\text{ions}}}{c_{\text{s}}} = &\frac{1}{2}\left(1 - \frac{y_\alpha - y_\beta}{2}\frac{1}{2+\frac{y_\alpha+y_\beta}{2}}\right)\ln\left(\frac{1}{1-\frac{y_\alpha-y_\beta}{2}\frac{1}{2+\frac{y_\alpha+y_\beta}{2}}}\right)\\ &+\frac{1}{2}\left(1 + y_\alpha - \frac{y_\alpha - y_\beta}{2}\frac{1}{2+\frac{y_\alpha+y_\beta}{2}}\right)\ln\left(\frac{1+\frac{y_\alpha+y_\beta}{2}}{1+y_\alpha-\frac{y_\alpha-y_\beta}{2}\frac{1}{2+\frac{y_\alpha+y_\beta}{2}}}\right)\\ &+\frac{1}{2}\left(1 + \frac{y_\alpha - y_\beta}{2}\frac{1}{2+\frac{y_\alpha+y_\beta}{2}}\right)\ln\left(\frac{1}{1+\frac{y_\alpha-y_\beta}{2}\frac{1}{2+\frac{y_\alpha+y_\beta}{2}}}\right)\\ &+\frac{1}{2}\left(1 + y_\beta + \frac{y_\alpha - y_\beta}{2}\frac{1}{2+\frac{y_\alpha+y_\beta}{2}}\right)\ln\left(\frac{1+\frac{y_\alpha+y_\beta}{2}}{1+y_\beta+\frac{y_\alpha-y_\beta}{2}\frac{1}{2+\frac{y_\alpha+y_\beta}{2}}}\right).\end{aligned} \tag{D.15}$$

D.4 Donnan Potential

An alternative expression for the Donnan potential ψ_D for $\theta = ½$ can be found by inserting Equation (D.7) into Equation (3.25) from Chapter 3:

$$\psi_D = \frac{RT}{F} \ln\left[\frac{1 + \frac{zc_0^P}{c_s}\eta^P}{1 + \frac{zc_0^P}{c_s}(1-\eta^P)} \right]. \tag{D.16}$$

This is in turn used to derive an approximation for $|\psi_D| \lesssim 20\,\mathrm{mV}$, by expanding Equation (D.16) around $\eta^P = 0.5$. This results in the following expression:

$$\psi_D \simeq \frac{RT}{F} \frac{zc_0^P}{c_s + \frac{1}{2}zc_0^P}(2\eta^P - 1) \tag{D.17}$$

$$= \frac{RT}{F} \frac{z(c_\alpha^P - c_\beta^P)}{2c_s + \frac{1}{2}z(c_\alpha^P + c_\beta^P)}. \tag{D.18}$$

In the situation where the volume of the two phases is not equal, the Donnan potential is alternatively found by inserting Equation (D.6) into Equation (3.25):

$$\psi_D = \frac{RT}{F} \ln\left(\frac{c_s}{c_s + zc_0^P(1-\eta^P)} \left\{ \frac{zc_0^P}{2c_s} \frac{\eta^P - 2\theta(1-\theta)\eta^P - \theta^2}{\theta(1-\theta)} + \sqrt{1 + \frac{zc_0^P}{c_s} + \left[\frac{zc_0^P}{2c_s} \frac{\eta^P - 2\theta\eta^P + \theta^2}{\theta(1-\theta)} \right]^2} \right\} \right). \tag{D.19}$$

Again, an approximation for low Donnan potentials is found using a Taylor expansion of Equation (D.19) in η^P around θ:

$$\psi_D \simeq \frac{RT}{F} \frac{zc_0^P}{2c_s + zc_0^P} \frac{\eta^P - \theta}{\theta(1-\theta)} \tag{D.20}$$

$$= \frac{RT}{F} \frac{z(c_\alpha^P - c_\beta^P)}{2c_s + z[c_\alpha^P\theta + c_\beta^P(1-\theta)]}. \tag{D.21}$$

CHAPTER 4

Interfacial Tension of Phase-Separated Aqueous Mixtures of Polyelectrolyte and Neutral Polymer

Abstract

Upon demixing, an aqueous solution of a polyelectrolyte with an incompatible neutral polymer yields two phases separated by an interface with an ultralow tension. Here, both in theory and experiment, this interfacial tension is studied in detail: how it scales with the concentrations of the polymers in the two phases and how it is affected by the interfacial difference in the electric potential. Experiments are performed on an aqueous model system of uncharged dextran and charged nongelling gelatin. The experimental tension scales to the power ~ 3 with the tie-line length in the phase diagram of demixing, in agreement with mean-field theory where space is filled with a binary mixture of polymer blobs. The interfacial electric potential difference is experimentally found to decrease the interfacial tension in a way that is consistent with Poisson–Boltzmann theory inspired from Frenkel and Verwey–Overbeek.

4.1 Introduction

The interface between the coexisting phases in a demixed solution of two polymers is not abrupt, but there are gradients in the relative composition and the total concentration of the polymers. A particularity of phase separating solutions—as opposed to phase-separated blends—results from the osmotic compressibility of the solutions: compared to the bulk phases, the interfacial region is diluted by uptake of solvent for fewer unfavorable contacts between the two polymers [25]. For a mixture of a charged polymer and an uncharged polymer, there is also an interfacial gradient in the electric charge density, corresponding to an interfacial electric potential step. As discussed in Chapters 2 and 3, this potential step is the so-called Donnan potential [39, 40], and its effect on the interfacial tension is the subject of this Chapter.

The Donnan potential originates from the accumulation of counterions in one of the phases—necessary for charge neutrality—in combination with the prerequisite of thermodynamic equilibrium. In order to increase entropy, the positive and negative ions spread across the interface to different extents; the buildup of charge separation halts the spreading. The accompanying electric potential difference is the Donnan potential. It has the same origin as the well-known membrane potential found in living cells and dialysis membranes. However, in our case, the charged interface is formed spontaneously and is in equilibrium with the bulk phases; moreover, the interfacial electric potential step is relatively small, typically less than 10 mV [52], as compared to 40 to 60 mV for the membranes of living cells.

The electric interfacial potential step contributes negatively to the interfacial tension due to the spontaneous formation of interfacial electric double layers. In certain scenarios the interfacial tension may become so low that it is favorable for the system to increase its interfacial area spontaneously and to form microdomain structures [65–67]. The question at the outset of the present work was whether the measured interfacial potential step can be quantitatively related to the measured interfacial tension and the phase diagram of demixing, with varying charge density and salt concentration.

The outline of this Chapter is as follows. In the first part of the theory section, expressions are given for the interfacial tension on the basis of the interfacial profiles of the relative composition and total concentration of polymers in solution. In the second part, the contribution to the interfacial tension from a charge density profile is calculated from the free energy density of two coupled electric double layers. Subsequently, the experimental procedures are described. Finally, the experimental results and the extent to which they agree with theory are discussed. Appendix E (starting on Page 77) explains the formula for the liquid–liquid interfacial profile near a vertical wall, which was used to determine the interfacial tension.

4.2 Theory

This section starts with the calculation of the interfacial tension of demixed solutions of neutral polymers, on the basis of the blob model. Next, the change in the tension of a liquid–liquid interface is calculated in the case that it carries an electric potential difference, using Poisson–Boltzmann theory. A list of symbols starts on Page 117.

4.2.1 Interfacial Tension of a Demixed Solution of Two Polymers

The blob model was introduced in Chapter 3 to describe the bulk behavior of a mixture of two polymers in solution. Here, the blob model is used to describe the interface between two coexisting phases formed by an aqueous mixture of two incompatible, uncharged polymers. Following Refs. 25, 26, 32, 56, and 57, we will first recapitulate the free energy resulting from the blob model for a single phase of a given relative composition and total polymer concentration. This will be extended subsequently in order to account for the presence of an interface, by allowing gradients in composition and concentration. The interfacial tension follows by finding gradients across the interface such that the excess grand free energy is minimized.

As discussed in Chapter 3, in the blob model, a polymer forms N_b solvent-filled blobs of characteristic size ξ. The blobs form an ideal chain. The volume fraction of blobs of polymer A and B are ϕ and $1-\phi$, respectively, and the total number of monomers (of A and B combined) per unit volume is c. The free energy per unit volume is given by [25, 26, 32, 56, 57]

$$\frac{F}{VkT} = \frac{1}{\xi^3(c)}\left[\frac{\phi}{N_\mathrm{b}(c)}\ln\phi + \frac{1-\phi}{N_\mathrm{b}(c)}\ln(1-\phi) + u(c)\phi(1-\phi) + K\right], \qquad (4.1)$$

where $u(c)$ represents the concentration-dependent repulsive interaction between the two polymers and $K = 0.024$ [56] represents the free energy of mixing within a blob. The blob size, the number of blobs per polymer chain, and the interaction potential are given by Equations (3.3) to (3.5). In the case that Equation (4.1) has two inflection points as a function of ϕ, the system can reduce its free energy by demixing into two phases, α and β, one rich in polymer A and one in B. The tie-line length L is used as a measure of the composition difference between the two phases, and it is given by Equation (3.49). The tie-line length serves as the order parameter to compare theory and experiments. The calculations employ the same parameters as in Chapter 3, listed in Table 3.1.

The interfacial tension can be calculated by allowing for ϕ and c to depend on position and adding the appropriate gradient terms to Equation (4.1). Following Broseta and co-workers [25, 56, 57] (see also Refs. 26 and 32), the free energy per unit

area with a planar interface between phases α and β is given by

$$\frac{F}{AkT} = \int_{-\infty}^{\infty} \mathrm{d}z \Bigg[\frac{\phi}{N_\mathrm{b}\xi^3} \ln(\phi) + \frac{1-\phi}{N_\mathrm{b}\xi^3} \ln(1-\phi) + \frac{u}{\xi^3}\phi(1-\phi) + \frac{K}{\xi^3} + \frac{\phi'^2}{24\xi\phi} + \frac{\phi'^2}{24\xi(1-\phi)} + \frac{c'^2}{24\xi c^2} \Bigg]. \tag{4.2}$$

Both ϕ and c are now functions of the distance z to the interface, and the primed symbols denote derivatives with respect to z. Note that since N_b, ξ, and u are functions of c, they are now also functions of z.

For convenience we define $\phi(z) \equiv [1+\eta(z)]/2$ and $c(z) \equiv \bar{c}[1+\bar{u}\epsilon(z)]$, where $\bar{c}$ and $\bar{u}$ represent the values of c and u in the bulk where gradients are absent. The deviation of $\phi(z)$ from ½ is expressed by $\eta(z)$, and the relative deviation of $c(z)$ from $\bar{c}$ is given by $\bar{u}\epsilon(z)$. Let us assume that $\bar{u}\epsilon(z)$ is small everywhere, so that we can approximate the concentration-dependent quantities to second order in $\bar{u}\epsilon(z)$, and that the gradients in composition are independent of the gradients in concentration. Further, $\omega \equiv \bar{N}_\mathrm{b}\bar{u}$ and $x \equiv z/D_\infty$ (with $D_\infty \equiv \bar{\xi}/(6\bar{u})^{1/2}$) are defined, where similarly $\bar{N}_\mathrm{b}$ and $\bar{\xi}$ represent bulk values. The excess grand free energy of the interface, per unit area, is then found by subtracting the free energies of each bulk phase given by Equation (4.1) from Equation (4.2):

$$\frac{\Omega}{AkT} = \frac{\sqrt{6\bar{u}}}{\bar{\xi}^2} \int_{-\infty}^{\infty} \mathrm{d}x \Bigg\{ \frac{1+\eta}{2\omega} \ln(1+\eta) + \frac{1-\eta}{2\omega} \ln(1-\eta) - \frac{\eta^2}{4} + \frac{\eta'^2}{4(1-\eta^2)} + \frac{1+\eta}{2\omega} \ln[\bar{u}\epsilon(1+\eta)] + \frac{1-\eta}{2\omega} \ln[\bar{u}\epsilon(1-\eta)] - \frac{3\nu+\chi}{4(3\nu-1)}\eta^2\bar{u}\epsilon + \frac{3\nu K}{2(3\nu-1)^2}\bar{u}\epsilon^2 + \frac{\bar{u}^2}{4}\epsilon'^2 - \mu_\eta\eta - \mu_\epsilon\bar{u}\epsilon + \bar{p} \Bigg\}, \tag{4.3}$$

where the bulk pressure and exchange chemical potential are given by

$$\bar{p} = -\frac{\bar{\eta}^2}{4} - \frac{1}{2\omega}\ln(1-\bar{\eta}^2), \tag{4.4}$$

$$\mu_\epsilon = \frac{1+\bar{\eta}}{2\omega}\ln(1+\bar{\eta}) + \frac{1-\bar{\eta}}{2\omega}\ln(1-\bar{\eta}) - \frac{3\nu+\chi}{4(3\nu-1)}\bar{\eta}^2, \tag{4.5}$$

and $\mu_\eta = 0$ because the phase separation is symmetric. The bulk composition $\bar{\eta}$ of the coexisting phases is found from the condition:

$$\frac{1}{\omega}\ln\left(\frac{1+\bar{\eta}}{1-\bar{\eta}}\right) - \bar{\eta} = 0, \tag{4.6}$$

where the compositions of phases α and β are given by $\eta_\alpha = \bar{\eta}$ and $\eta_\beta = -\bar{\eta}$.

The optimal composition profile $\eta(x)$ that minimizes the interfacial tension is denoted as $\eta_0(x)$. We assume no effect of the concentration profile on the composition

profile, so $\epsilon(x)$ can be set to zero. The composition profile is found by numerically solving the following differential equation, obtained by using the Euler–Lagrange equation:

$$\frac{\eta_0'(x)^2}{4[1-\eta_0(x)^2]} = \frac{1+\eta_0(x)}{2\omega}\ln[1+\eta_0(x)] + \frac{1-\eta_0(x)}{2\omega}\ln[1-\eta_0(x)] - \frac{\eta_0(x)^2}{4} + \bar{p}, \tag{4.7}$$

for which the boundary condition that $\eta_0(x) = 0$ at $x = 0$ is used. Once a solution for $\eta_0(x)$ is known, this can be used to find the optimal profile of $\epsilon(x)$, $\epsilon_0(x)$, by solving

$$\frac{\bar{u}}{2}\epsilon_0''(x) = \frac{1+\eta_0(x)}{2\omega}\ln[1+\eta_0(x)] + \frac{1-\eta_0(x)}{2\omega}\ln[1-\eta_0(x)] + \frac{3\nu K}{(3\nu-1)^2}\epsilon_0(x) - \frac{3\nu+\chi}{4(3\nu-1)}\eta_0(x)^2 - \mu_\epsilon. \tag{4.8}$$

This can be done efficiently numerically using the finite element method, with the boundary conditions that $\epsilon_0'(0) = 0$ and that $\epsilon_0(x)$ goes to zero for large x. Examples of profiles close to and far away from the critical point are given in Figure 4.1.

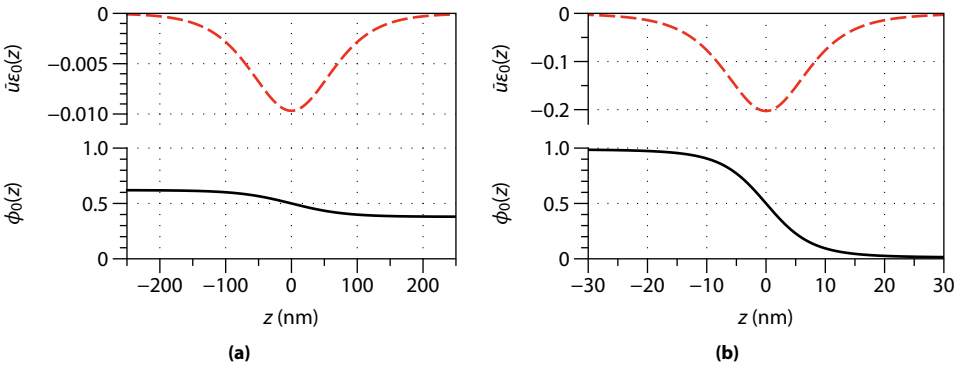

Figure 4.1: Equilibrium profiles of the concentration change $\bar{u}\epsilon_0(z)$ and the polymer composition $\phi_0(z) = [1 + \eta_0(z)]/2$ for (a) $w = 6\,\%$, where $\gamma = 0.06\,\mu N/m$, and (b) $w = 10\,\%$, where $\gamma = 25\,\mu N/m$. The interfacial region goes through a minimum in the total polymer concentration and extends over increasingly large distances as one nears the critical point of demixing. The blob sizes are (a) 3.4 nm and (b) 2.3 nm. The calculations were made on the basis of Equations (4.1) to (4.8) and Table 3.1.

The interfacial tension γ is then given by

$$\gamma = \frac{kT}{\bar{\xi}^2}\sqrt{\frac{\bar{u}}{6}} \times (1 - \Delta_1 - \bar{u}\Delta_2), \tag{4.9}$$

where

$$\Delta_1 = 1 - 2\int_0^{\bar{\eta}} \mathrm{d}\eta\,(1-\eta^2)^{-1/2} \times \left[\frac{1+\eta}{2\omega}\ln(1+\eta) + \frac{1-\eta}{2\omega}\ln(1-\eta) - \frac{\eta^2}{4} + \bar{p}\right]^{1/2}, \tag{4.10}$$

$$\Delta_2 = \int_{-\infty}^{\infty} \mathrm{d}x\,\epsilon_0(x) \times \left\{\frac{-\eta_0'(x)^2}{8[1-\eta_0(x)^2]} + \frac{1+\chi}{8(3\nu-1)}[\eta_0(x)^2 - \bar{\eta}^2]\right\}. \tag{4.11}$$

Here, Δ_1 represents the interfacial tension due to an optimal profile in the composition (i.e., the blob volume fraction $\phi(z)$) across the interface, at constant total monomer concentration c. Conform Van der Waals theory [68], this contribution may be calculated without prior knowledge of $\eta_0(x)$; instead, it follows directly from the integral above.

On the other hand, Δ_2 represents a reduction in γ by allowing the total monomer concentration c to vary across the interface, which requires knowledge of both $\eta_0(x)$ and $\epsilon_0(x)$. For parameters matching our experimental system, far away from the critical point, the total monomer concentration at the interface is roughly 20 % lower than in bulk and the interfacial zone has a typical width of 10 nm, as is evident from Figure 4.1b.

The effect of the reduction of the polymer concentration at the interface on the interfacial tension can be quantified by calculating the ratio

$$\Gamma \equiv \frac{1-\Delta_1-\bar{u}\Delta_2}{1-\Delta_1}. \tag{4.12}$$

This ratio is shown in Figure 4.2 as a function of the tie-line length L. Far from the critical point, γ is reduced by 15 %, but close to the critical point significantly more. Experimentally, L is in the range of 2 to 15 %, so the effect of solvent redistribution cannot be neglected and is certainly not constant when varying the tie-line length in this range.

4.2.2 Effect of Interfacial Electric Potential Difference

In order to capture the effects of an interfacial electric potential difference on the interfacial tension, the free energy of the electric double layers at the liquid–liquid interface will be calculated using Poisson–Boltzmann theory. This free energy represents a contribution to the interfacial tension and, as these double layers form spontaneously, it is negative. The following derivation closely resembles that found in the books by Verwey and Overbeek [69] and Frenkel [70] for a solid–liquid interface, somewhat adapted in order to account for the presence of two aqueous phases; similar theory has been applied to charged oil–water and water–air interfaces [71–73].

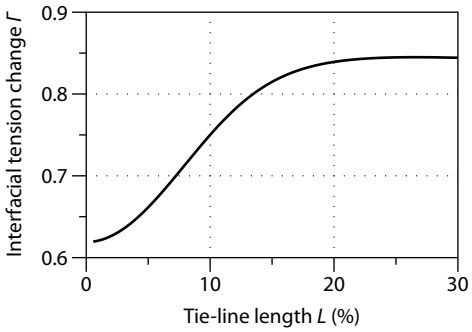

Figure 4.2: Relative change Γ of the interfacial tension due to solvent redistribution as a function of the tie-line length L, see Equation (4.12).

In general, the Poisson–Boltzmann equation reads as follows

$$\frac{\mathrm{d}^2\psi}{\mathrm{d}z^2} = \kappa^2 \frac{kT}{e} \sinh\left(\frac{e\psi}{kT}\right), \tag{4.13}$$

where $\psi(z)$ is the potential at a distance z from the interface, e is the elementary charge, k is the Boltzmann constant, and T is the absolute temperature. The Debye screening constant is defined as $\kappa = (8\pi\lambda_\mathrm{B} c_\mathrm{s})^{1/2}$, with c_s the concentration of salt far from the charged interface (where $\psi = 0$) and $\lambda_\mathrm{B} \equiv e^2/(4\pi\epsilon\epsilon_0 kT)$ the Bjerrum length. ϵ is the relative permittivity and ϵ_0 the permittivity of free space.

Using the dimensionless potential $\Psi \equiv e\psi/(kT)$ and dimensionless distance $Z \equiv \kappa z$, the Poisson–Boltzmann equation becomes

$$\frac{\mathrm{d}^2\Psi}{\mathrm{d}Z^2} = \sinh[\Psi(Z)]. \tag{4.14}$$

Starting from this, the interfacial charge density will be calculated, which subsequently can be used to calculate the free energy of electric double layers.

Charge Density of the Electric Double Layer

The water–water interface can be modeled similarly as a charged solid surface immersed in a liquid, except that we will model it as *two* coupled electric double layers, one in each phase. At this interface, the concentration $c^\mathrm{p}(Z)$ of polyelectrolyte will gradually change from c_α^p to c_β^p. We will examine the case that phase α is rich in the polyelectrolyte and that the polyelectrolyte itself carries a number of positive charges z (not to be confused with the spatial coordinate z).

Close to the interface, the concentration of polyelectrolyte is either lower (in phase α) or higher (in β) than in bulk. Let us assign to this a local polyelectrolyte excess

charge density, $ze[c^{\mathrm{p}}(Z) - c^{\mathrm{p}}_{\mathrm{bulk}}]$, which can be integrated over Z in order to obtain a surface charge density on each side of the interface. These surface charge densities will lead to the formation of a diffuse layer of oppositely charged ions on each side of the interface, thus creating two double layers.

Suppose that far from the interface, the phases have electric potentials given by Ψ^{∞}_{α} and Ψ^{∞}_{β}, and that the potential is $\Psi^{0}_{\alpha} = \Psi^{0}_{\beta}$ at the interface. The Poisson–Boltzmann equation takes the following form:

$$\frac{\mathrm{d}^2\Psi_{\alpha}}{\mathrm{d}Z^2} = \sinh(\Psi_{\alpha} - \Psi^{\infty}_{\alpha}) \qquad \text{for } Z < 0, \tag{4.15a}$$

$$\frac{\mathrm{d}^2\Psi_{\beta}}{\mathrm{d}Z^2} = \sinh(\Psi_{\beta} - \Psi^{\infty}_{\beta}) \qquad \text{for } Z > 0. \tag{4.15b}$$

The profile $\Psi(Z)$ of the electric potential obtained this way is depicted in Figure 4.3.

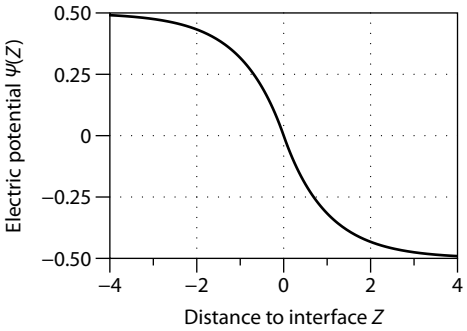

Figure 4.3: Profile of the dimensionless electric potential $\Psi \equiv e\psi/(kT)$ as a function of the dimensionless distance $Z \equiv \kappa z$ to the interface. The profile is obtained by solving Equation (4.15) for $\Psi^{\infty}_{\alpha} = -\Psi^{\infty}_{\beta} = ½$ and $\Psi^{0}_{\alpha} = \Psi^{0}_{\beta} = 0$.

The local concentrations of positive and negative ions are given by $c^{+}(Z) = c_{\mathrm{s}} \exp[-(\Psi - \Psi^{\infty})]$ and $c^{-}(Z) = c_{\mathrm{s}} \exp[+(\Psi - \Psi^{\infty})]$, where Ψ and Ψ^{∞} refer to the potentials of phase α for $Z < 0$ and of phase β for $Z > 0$. The local charge density $\rho(Z) \equiv e[c^{+}(Z) - c^{-}(Z)]$ is then

$$\rho(Z) = -2c_{\mathrm{s}}e \sinh(\Psi - \Psi^{\infty}). \tag{4.16}$$

Given Equations (4.15a) and (4.15b), we see that $\rho(Z) = -2c_{\mathrm{s}}e\,\mathrm{d}^2\Psi/\mathrm{d}Z^2$. The charge per unit area σ of the diffuse layer is found by integrating $\rho(Z)$ in the direction

perpendicular to the interface. We find for σ in phase α, denoted σ_α,

$$\sigma_\alpha = \int_{-\infty}^{0} \rho_\alpha(z)\,\mathrm{d}z \tag{4.17}$$

$$= \kappa_\alpha^{-1} \int_{-\infty}^{0} \rho_\alpha(Z)\,\mathrm{d}Z \tag{4.18}$$

$$= -\frac{e\kappa_\alpha}{2\pi\lambda_{\mathrm{B},\alpha}} \sinh\left(\frac{\Psi_\alpha^0 - \Psi_\alpha^\infty}{2}\right). \tag{4.19}$$

Here $\Psi_\alpha^0 = \Psi_\alpha(0)$ is the potential at the interface. Similarly, for σ_β:

$$\sigma_\beta = \kappa_\beta^{-1} \int_{0}^{\infty} \rho_\beta(Z)\,\mathrm{d}Z \tag{4.20}$$

$$= -\frac{e\kappa_\beta}{2\pi\lambda_{\mathrm{B},\beta}} \sinh\left(\frac{\Psi_\beta^0 - \Psi_\beta^\infty}{2}\right). \tag{4.21}$$

Note that we have allowed the dielectric constants and Debye lengths in the two phases to be unequal.

In order to maintain electroneutrality over the two double layers, we have to fulfill the requirement that $\sigma_\alpha + \sigma_\beta = 0$. Setting $\Psi_\alpha^0 = \Psi_\beta^0 = 0$, it follows that

$$\Psi_\alpha^\infty = \ln\left[\frac{\omega + \exp(\Psi_\mathrm{D}/2)}{\omega + \exp(-\Psi_\mathrm{D}/2)}\right], \tag{4.22}$$

$$\Psi_\beta^\infty = \ln\left[\frac{\omega\,\exp(-\Psi_\mathrm{D}/2) + 1}{\omega\,\exp(\Psi_\mathrm{D}/2) + 1}\right], \tag{4.23}$$

where

$$\omega \equiv \sqrt{\frac{c_{\mathrm{s},\alpha}\epsilon_\alpha}{c_{\mathrm{s},\beta}\epsilon_\beta}}. \tag{4.24}$$

As in the previous Chapters, Ψ_D represents the potential difference between the bulk phases, i.e., $\Psi_\mathrm{D} \equiv \Psi_\alpha^\infty - \Psi_\beta^\infty$. For low Ψ_D, Equations (4.22) and (4.23) can be approximated as $\Psi_\alpha^\infty \simeq +\Psi_\mathrm{D}\frac{1}{1+\omega}$ and $\Psi_\beta^\infty \simeq -\Psi_\mathrm{D}\frac{\omega}{1+\omega}$.

Free Energy of the Electric Double Layer

From the interfacial charge density, the free energy per unit area $f \equiv F/A$ of the double layer in each phase can be calculated. Following the arguments by Verwey and Overbeek [69] and Frenkel [70], f is in general found from

$$f = \frac{kT}{e} \int_0^\Psi \sigma(\Psi')\,\mathrm{d}\Psi', \tag{4.25}$$

where the prime symbols now denote a dummy variable. Performing the integration yields, for phase α,

$$f_\alpha = -\frac{kT\kappa_\alpha}{\pi\lambda_{\mathrm{B},\alpha}}\left[\cosh\left(\frac{\Psi_\alpha^\infty}{2}\right) - 1\right]. \tag{4.26}$$

It is convenient to define an *effective* salt concentration $c_\mathrm{s} \equiv \sqrt{c_{\mathrm{s},\alpha}c_{\mathrm{s},\beta}}$ and relative permittivity $\epsilon \equiv \sqrt{\epsilon_\alpha\epsilon_\beta}$ so that global values of the Bjerrum and Debye lengths are given by

$$\lambda_\mathrm{B}\kappa^{-1} = \sqrt{\omega}\,\lambda_{\mathrm{B},\alpha}\,\kappa_\alpha^{-1} \tag{4.27}$$

$$= \frac{1}{\sqrt{\omega}}\,\lambda_{\mathrm{B},\beta}\,\kappa_\beta^{-1}. \tag{4.28}$$

Thus, f_α can be written as

$$f_\alpha = -\frac{kT\kappa}{\pi\lambda_\mathrm{B}}\sqrt{\omega}\left[\cosh\left(\frac{\Psi_\alpha^\infty}{2}\right) - 1\right]. \tag{4.29}$$

Using $\cosh x \simeq 1 + \frac{1}{2}x^2$, we find the following approximation:

$$f_\alpha \simeq -\left(\frac{\Psi_\mathrm{D}}{2}\right)^2\left(\frac{1}{1+\omega}\right)^2\sqrt{\omega}\frac{kT\kappa}{2\pi\lambda_\mathrm{B}}, \tag{4.30}$$

which introduces an error of less than 2 % as long as the value of the argument of the hyperbolic cosine is less than 0.5.

A similar derivation can be performed for the double layer in phase β, which results in a free energy per unit area given by

$$f_\beta = -\frac{kT\kappa}{\pi\lambda_\mathrm{B}}\frac{1}{\sqrt{\omega}}\left[\cosh\left(\frac{\Psi_\beta^\infty}{2}\right) - 1\right] \tag{4.31}$$

$$\simeq -\left(\frac{\Psi_\mathrm{D}}{2}\right)^2\left(\frac{\omega}{1+\omega}\right)^2\frac{1}{\sqrt{\omega}}\frac{kT\kappa}{2\pi\lambda_\mathrm{B}}. \tag{4.32}$$

The sum of f_α and f_β represents the change $\Delta\gamma$ in the interfacial tension due to charge:

$$\Delta\gamma \equiv f_\alpha + f_\beta \tag{4.33}$$

$$\simeq -\left(\frac{\Psi_\mathrm{D}}{2}\right)^2\frac{\sqrt{\omega}}{1+\omega}\frac{kT\kappa}{2\pi\lambda_\mathrm{B}}. \tag{4.34}$$

We now turn our attention to the parameter ω, and in particular to the factor $\sqrt{\omega}/(1+\omega)$, in Equation (4.34). For a phase-separated aqueous polymer mixture, the dielectric constant of the two phases will be approximately the same. However, due to the electric potential difference between the phases, the ionic strengths of the

two phases will certainly not be the same, as determined by the Donnan equilibrium $\Psi_D = \ln(c_\beta^+/c_\alpha^+) = \ln(c_\alpha^-/c_\beta^-)$ (see, e.g., Equation (3.24)). If we suppose that the (positively charged) polyelectrolyte also contributes to the Debye length, then the concentration of anions in each phase is a good measure for the ionic strength of the phases. We find that ω is given by $\omega = (c_\alpha^-/c_\beta^-)^{1/2} = \exp(\Psi_D/2)$.

Regardless of the precise value of ω, as long as ω is in the neighborhood of 1, the factor $\sqrt{\omega}/(1+\omega) \simeq ½$. Even for $\Psi_D = 1$, where $\omega \simeq 1.65$, the factor $\sqrt{\omega}/(1+\omega)$ deviates only 3 % from ½. Thus, it seems reasonable to approximate Equation (4.34) as

$$\Delta\gamma \simeq -\left(\frac{\Psi_D}{4}\right)^2 \frac{kT\kappa}{\pi\lambda_B}. \tag{4.35}$$

Despite the approximations involved, Equation (4.35) describes the change in the interfacial tension very accurately up to $\Psi_D = 1$ ($\psi_D \simeq 25\,\mathrm{mV}$), where it deviates only a few percent from the exact expression, as shown in Figure 4.4.

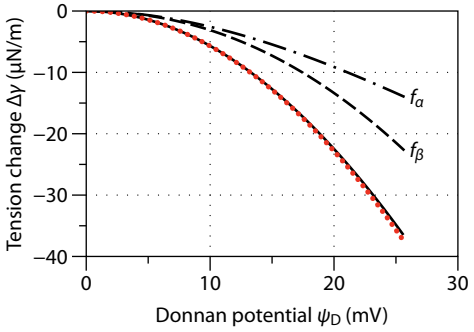

Figure 4.4: Electric contribution to the interfacial tension as a function of the Donnan potential ψ_D. The contributions per phase f_α and f_β are given by Equations (4.26) and (4.31). Their sum $\Delta\gamma = f_\alpha + f_\beta$ is denoted by the solid line and the approximated form, given by Equation (4.35), is the red dotted line. We have taken $c_s = \sqrt{c_{s,\alpha}c_{s,\beta}} = 10\,\mathrm{mM}$, $\epsilon_\alpha = \epsilon_\beta = 78$, and $c_{s,\alpha}/c_{s,\beta} = \exp(\Psi_D)$.

From a comparison of this result to that of a solid–liquid interface [69, 70], it is apparent that the resulting formulas are similar. The reduction in the interfacial tension predicted for the liquid–liquid interface is smaller, because the potential difference occurs over a wider region. As the liquid–liquid interface is viewed as two joined double layers, each double layer carries approximately half of the potential drop. The free energy of each double layer scales quadratically with the low potentials involved, so that their free energy is one-fourth that of a single double layer carrying the full potential drop in a solid–liquid interface. However, given that the description

of the liquid–liquid interface requires two joined double layers, the decrease in the interfacial tension has half the magnitude compared to the solid–liquid interface.

4.3 Experimental

In this section, the experimental techniques used to measure the interfacial tension of phase-separated aqueous dextran–gelatin mixtures are described. The interfacial tensions were obtained from the capillary length, which was in turn found from an analysis of the static profile of the interface near a vertical wall. This method has been applied before to demixed colloid–polymer mixtures with a similar ultralow interfacial tension [74]. We chose to use this method, as it has been observed that the shear in dynamic methods such as spinning drop could affect the equilibrium phase behavior [75, 76].

Details of the sample preparation were given in Section 2.3.1. Stock solutions of the uncharged polymer dextran (100 kDa) were mixed with stock solutions of the charged polymer gelatin (gelling temperature 8 to 10 °C, 100 kDa) in a 1:1 polymer mass ratio. The charge of gelatin was adjusted by changing the pH and was derived from the titration in Chapter 3. The samples had typical polymer mass fractions of 5 to 20 %. The salt concentration in the resulting samples was approximately 9, 5, and 7 mM at pH 4.8, 6.2, and 9.2, respectively, as deduced from conductivity measurements. In order to study the behavior at increased ionic strength, 50 mM KCl was added. After vortex mixing, samples were centrifuged overnight to achieve two clear macroscopic phases.

Part of the top phase of a sample was collected using a syringe with hypodermic needle. Then the interface was carefully punctured with a fresh needle and syringe, and part of the bottom phase was collected. Part of the isolated bottom phase was placed into a $1 \times 1\,\mathrm{cm}^2$ polystyrene cuvette, followed by part of the top phase. The cuvettes were centrifuged at 100–200g for one to two hours in order to remove possible droplets that might have formed during manipulation. A cuvette was mounted in a Nikon Eclipse LV100 Pol that was placed sideways to have a horizontal optical path. Objectives with two or ten times magnification were used, depending on the capillary length, and the images were captured using a QImaging MicroPublisher 5.0 RTV camera. Special attention was paid to ensure that cuvette, microscope, and camera were all level. An example of an image obtained in this way is shown in Figure 4.5a.

In order to extract the interfacial profiles, the resulting images were analyzed using edge and gradient detection algorithms provided with Mathematica. The profiles were fitted to the following equation, found e.g. in the book of Batchelor [77], yielding

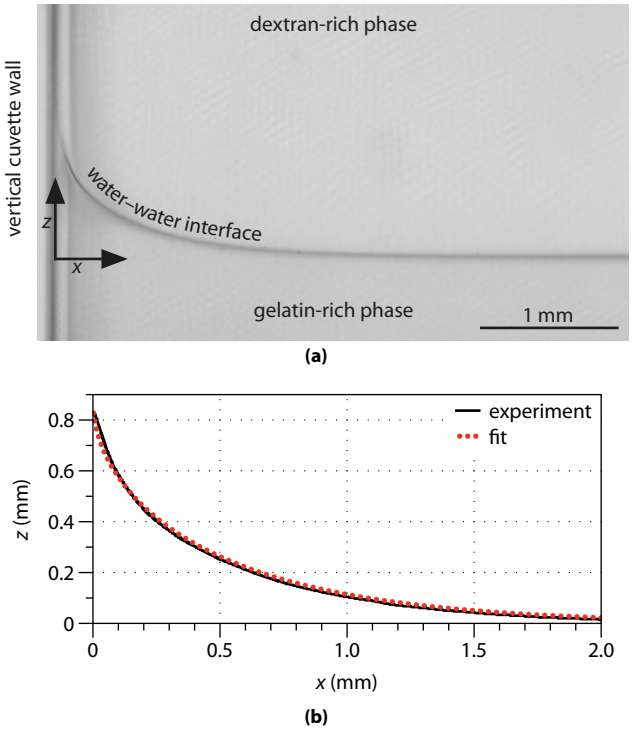

Figure 4.5: Determination of the interfacial tension. The profile of a water–water interface in a demixed solution of dextran and gelatin (total mass fraction 10 %, pH 9.2) is imaged near the wall of a polystyrene cuvette. (a) Micrograph and (b) profile obtained using image analysis together with a fit to Equation (4.36). The density difference is $\Delta\rho = 1.257 \times 10^{-3}\,\mathrm{g/cm^3}$, and the values resulting from this fit are $l_c = 0.619\,\mathrm{mm}$ and $\gamma = 4.72\,\mu\mathrm{N/m}$. The tie-line length in the phase diagram of demixing is 9.87 ± 0.07 %.

the capillary length:

$$\frac{x(z)}{l_c} = \operatorname{arccosh}\left(\frac{2l_c}{z}\right) - \operatorname{arccosh}\left(\frac{2l_c}{h}\right) - \sqrt{4 - \frac{z^2}{l_c^2}} + \sqrt{4 - \frac{h^2}{l_c^2}}, \tag{4.36}$$

where x is the horizontal distance to the vertical wall, z is the elevation of the interface above the level at large x, h is the contact height (i.e., the elevation of the interface at $x = 0$), and l_c is the capillary length. The capillary length is defined as

$$l_c \equiv \sqrt{\gamma/(\Delta\rho g)}, \tag{4.37}$$

where $\Delta\rho$ is the density difference between the two phases and g is the gravitational acceleration. The contact height h is related to the contact angle θ by

$$h^2 = 2l_c^2(1 - \sin\theta). \tag{4.38}$$

A detailed derivation of Equation (4.36) and more information on the fitting procedure is given in Appendix E. A comparison of an extracted profile and the resulting fit is given in Figure 4.5b, which shows excellent agreement.

Extracting the interfacial tension from the capillary length requires knowledge of the density difference between the two phases. The density of the isolated phases was measured using an Anton Paar DMA 5000 oscillating U-tube density meter, which is accurate to $10^{-6}\,\mathrm{g/cm^3}$. Such extreme accuracy is necessary, as the density difference between the coexisting phases is typically $10^{-3}\,\mathrm{g/cm^3}$ or lower.

The composition of the isolated phases was determined as described in Section 2.3.2, enabling the measurement of the interfacial tension as a function of the tie-line length as expressed by Equation (3.49). The analysis was performed for the profiles at both the left and right walls of the cuvette. For each side, multiple images were analyzed. The results were averaged per sample and the standard deviations computed.

4.4 Results

In this section, first the phase diagrams and the measurements of the interfacial electric potential difference from previous Chapters will be briefly revisited. Then, the measured interfacial tensions will be presented. Finally, the measured Donnan potentials and interfacial tensions will be combined in order to calculate the tension of the interface as if it were uncharged.

In Chapter 3, the composition of the coexisting phases for many samples is analyzed, and phase diagrams such as Figure 3.2a are obtained. Via the pH, the phase behavior depends strongly on the number of charges z on the polyelectrolyte gelatin:

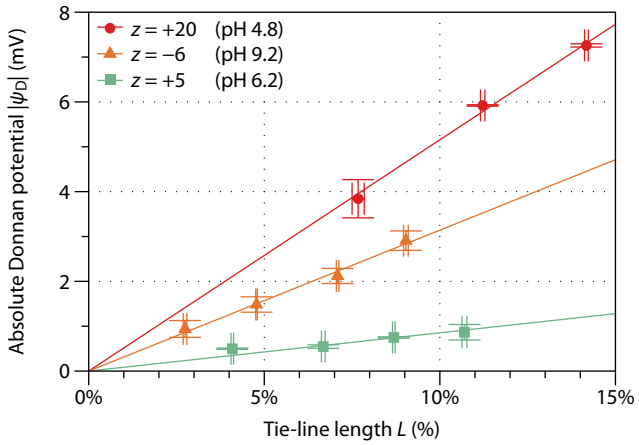

Figure 4.6: Absolute Donnan potential $|\psi_D|$ from Chapter 2 as a function of the tie-line length L. The solid lines represent a linear fit through the origin, used to calculate the effect of charge on the interfacial tension, $\Delta\gamma$, as a function of L using Equation (4.35).

the binodal is shifted away from the origin upon increasing z from, e.g., +5 to +20. This means that, at the different values of z, phase separation takes place at polymer concentrations that are roughly a factor of two different. In order to be able to compare the Donnan potentials and interfacial tensions at these different charges, we will report these as a function of the tie-line length. By analyzing samples of various charges at equal tie-line length, an equal degree of phase separation is implied, making for an apt comparison.

The measured Donnan potentials are shown in Figure 4.6. These are the same measurements as in Figure 2.4, except that they are now given as a function of the tie-line length, for the aforementioned reasons. A linear correlation of the electric potential difference is observed with the tie-line length. This is as expected, since the Donnan potential scales linearly with the difference in polyelectrolyte concentration according to Equation (2.12) and the tie-line length is a direct measure of the compositional difference between the two phases. For increased magnitudes of the polyelectrolyte charge z, the magnitude of the Donnan potential is also increased (at a fixed tie-line length), resulting in an increased slope of the plot of $|\psi_D|$ against the tie-line length. For $z = -6$, the measured Donnan potentials are actually negative, but here we report the absolute value.

Figure 4.7 shows the measured interfacial tension as a function of the tie-line length. The tensions vary over three orders of magnitude and show power-law scaling with the tie-line length, with an exponent of approximately 3.3 independent of the charge z and salt concentration. While the scaling exponent appears to be independent of z,

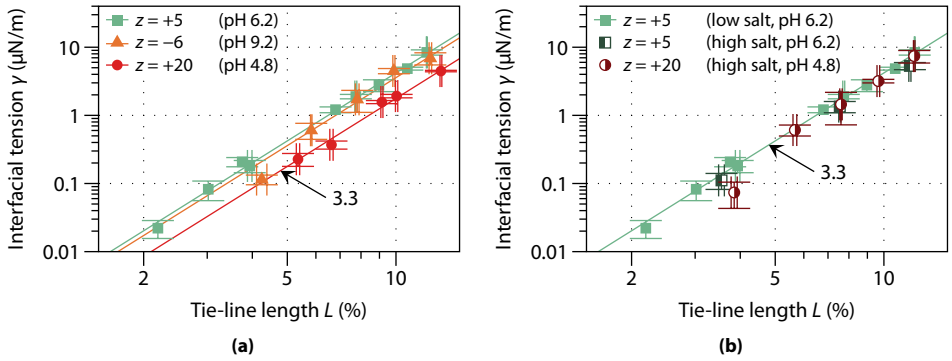

Figure 4.7: Measured interfacial tension γ as a function of the tie-line length L, showing the effect of (a) polyelectrolyte charge (low ionic strength, 5 to 10 mM) and (b) the addition of 50 mM KCl. The solid lines are power-law fits with a common exponent of 3.3.

the magnitude of the interfacial tension does depend on z at low ionic strength. Going from $z = +5$ to $z = -6$ we observe, if anything, a minute decrease of the interfacial tension. More strongly increasing the magnitude of the charge to $z = +20$ causes a pronounced decrease in the interfacial tension by, approximately, a factor of two. The interfacial tensions found in the presence of 50 mM KCl appear to be independent of charge and have about the same magnitude as for $z = +5$ at low ionic strength.

In order to elucidate the origin of the decrease in the interfacial tension, we used the measured Donnan potentials to calculate the change $\Delta\gamma$ in the interfacial tension as predicted by Poisson–Boltzmann theory. As the fits in Figure 4.6 give us the Donnan potential ψ_D as a function of the tie-line length L, inserting these fits into Equation (4.35) gives us $\Delta\gamma$ as a function of L. By subtracting the calculated values of $\Delta\gamma$, which are always negative, from the measured interfacial tensions γ, we can assess the role of the interfacial electric double layers in the change of the interfacial tension. In a sense, this procedure provides us with the "intrinsic" tension γ_0 of the interface, as if it were uncharged.

The resulting intrinsic interfacial tensions $\gamma_0 = \gamma - \Delta\gamma$ are shown in Figure 4.8. The interfacial tensions for all three values of z appear to fall on a single curve, which scales with a power of 3.22 ± 0.08 with the tie-line length. The exponent is found by taking the logarithm of the tension and tie-line length and performing a linear least-squares fit. We can compare these interfacial tensions with those calculated from the blob model for a mixed solution of uncharged polymers, using Equation (4.9) and Table 3.1. The blob model shows very similar power-law scaling, with an exponent of 3.153 ± 0.005 for L in the range 2 to 10 %. Nevertheless, the tensions predicted by the blob model are approximately a factor of two higher than observed in the experiments.

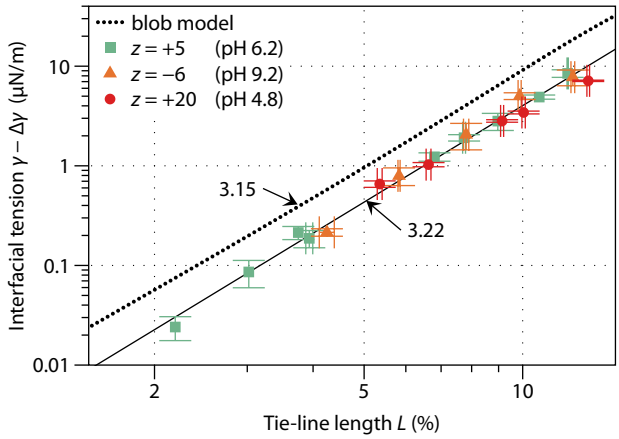

Figure 4.8: Measured interfacial tension γ, compensated for the decrease $\Delta\gamma$ due to the interfacial electric potential difference (Equation (4.35)), as a function of the tie-line length L. The solid line is a power-law fit to all compensated experimental values, with an exponent of 3.22 ± 0.08, and the dotted line is the interfacial tension as calculated using the blob model, with an exponent of 3.153 ± 0.005.

4.5 Discussion

Our detailed measurements of the Donnan potential and the interfacial tension presented in the previous section clearly show that an increase in the magnitude of the Donnan potential corresponds with a decrease in the interfacial tension at fixed tie-line length. The addition of salt suppresses the Donnan potential according to Equation (2.12) and, as observed experimentally, also suppresses the decrease of the interfacial tension. The decrease in tension is—according to Poisson–Boltzmann theory—expected to be caused by the negative free energy of spontaneously formed electric double layers. This free energy per unit area $\Delta\gamma$ may be calculated on the basis of measured electric potential differences and subtracted from the measured interfacial tensions, which gives us the intrinsic interfacial tensions $\gamma_0 = \gamma - \Delta\gamma$. When plotted in this way, all points collapse onto a master curve, supporting the predicted influence of the Donnan potential on the interfacial tension.

We have evaluated the interfacial tensions in our system as a function of the tie-line length, which is a measure of the degree of phase separation. If two samples (with a different polyelectrolyte charge z, critical point, and binodal) have the same tie-line length, the difference in concentration of the two polymers between the coexisting phases is on average the same. Therefore, the fact that the intrinsic interfacial tensions as a function of the tie-line length all collapse onto a single curve suggests that the

interfacial tension is set by the tie-line length and electric potential differences, and that other possible effects such as different chain statistics play a minor role, despite the polymers being present at substantially different concentrations. It also supports the experimentally measured Donnan potentials.

The interfacial tensions as calculated using the blob model are about twice as large as the measured interfacial tensions. It is to be expected that the calculated interfacial tensions are higher than those measured, since for instance monodisperse polymers are assumed in the calculations, whereas both dextran and gelatin are polydisperse. It is known that the interfacial tension of similar systems decreases with decreasing polymer molar mass, even if the same tie-line length is maintained [29, 30]. As such, the presence of low-molar mass material may reduce the interfacial tension. Additionally, in order to simplify the calculations, the interfacial profile of the blob volume fraction $\eta(z)$ was optimized assuming a constant total polymer concentration throughout the interface (i.e., $\bar{u}\epsilon(z) = 0$). Only after that, the profile $\bar{u}\epsilon(z)$ was optimized, assuming a fixed profile $\eta(z)$. Ideally, the two profiles would be optimized simultaneously, potentially yielding lower interfacial tensions.

A power-law scaling between the interfacial tension and tie-line length with an exponent equal to 3 may be expected from mean-field theory. When not taking into account solvent redistribution in our calculations, we find as expected an exponent 3.0451 ± 0.0014 (not shown) due to their mean-field nature. This exponent increases to 3.153 ± 0.005 when including solvent redistribution. This is similar to the exponent found experimentally (3.22 ± 0.08). Indeed, performing a t-test reveals that the experimental exponent is not significantly different from the calculated value[1]. The experimental exponent is however, using the same criteria, significantly different from the value calculated without solvent redistribution. This serves as an important indication that solvent redistribution also affects the scaling of the interfacial tension experimentally.

While interfacial tensions have been reported before for similar systems [7, 28], literature data on the scaling of the interfacial tension with the tie-line length (or sometimes density difference) in comparable systems remains scarce and a range of scaling exponents has been reported. For PEG–dextran, Forciniti *et al.* reported numerous exponents depending on molar mass and temperature, with a mean of 3.74 ± 0.78 [29], while Bamberger *et al.* reported values in the range of 3.5 to 4.1 [78] and Liu *et al.* found mean-field behavior far from the critical point [79]. Ding *et al.* reported a value of 2.4 for dextran–gelatin [30], and Scholten *et al.* found scaling with the density difference with an exponent of 2.7 ± 0.3 for the same system [31]. Antonov *et al.* found an exponent of 3.1 ± 0.3 with $\Delta\rho$ for caseinate–alginate [80],

[1]The t-test was performed using the 19 measurements resulting in 17 degrees of freedom, confidence level 95 %, neglecting the standard deviation in the exponent from theory.

whereas Simeone *et al.* reported linear correlation between γ and the tie-line length or the density difference [81]. Mean-field exponents have also been reported for complex coacervates [82, 83], which are formed by oppositely charged polymers in solution. The present results show that accurate information on the scaling behavior and magnitude of the interfacial tension can be obtained by analyzing the shape of the interfacial profile.

4.6 Conclusion

The presence of charge on one of the polymers in coexisting solutions of polyelectrolyte and neutral polymer leads to a Donnan equilibrium and the formation of an interfacial electric potential difference. It is due to this Donnan potential that the interfacial tension decreases when the absolute charge of the polyelectrolyte increases, and this decrease can be understood quantitatively on the basis of Poisson–Boltzmann theory. The magnitude and scaling behavior of the interfacial tension as calculated using the blob model compare favorably with experiments. Solvent accumulation at the water–water interface has an experimentally accessible effect on the scaling behavior of the interfacial tension and can explain the experimentally observed scaling behavior.

APPENDIX E

Profile of the Liquid–Liquid Interface near a Vertical Wall

In order to clarify the shape of an interface between two liquids in equilibrium with each other at a vertical wall (Equation (4.36)), we will expand on the very concise derivation by Batchelor [77]. In equilibrium, the shape is determined by the balance of pressures due to gravity and due to the curvature of the interface:

$$\Delta\rho g z(x,y) - \gamma\left[\frac{1}{R_1(x,y)} + \frac{1}{R_2(x,y)}\right] = \text{constant}. \tag{E.1}$$

Here, $\Delta\rho$ is the density difference between the two phases, g is the gravitational acceleration, $z(x,y)$ is the height of the interface at position (x,y), γ is the interfacial tension, and $R_1(x,y)$ and $R_2(x,y)$ are the radii of curvature. The constant on the right-hand side depends on the boundary conditions.

Assume that the two liquid phases form a macroscopically flat interface in the xy-plane at height $z = 0$. If a flat wall is placed in the zy-plane, the interface will deform locally in order to satisfy the contact angle θ between the interface and the wall, as shown in Figure 4.5. The interface will be curved in the direction x perpendicular to the wall, but not in the y-direction. The height of the interface is independent of y (i.e., $z(x,y) = z(x)$) and the curvatures are given by

$$\frac{1}{R_1} = \frac{z''(x)}{[1 + z'(x)^2]^{3/2}}, \tag{E.2}$$

$$\frac{1}{R_2} = 0. \tag{E.3}$$

Because the flat interface far away from the wall is located at $z = 0$, the right-hand side of Equation (E.1) is zero. Therefore, z is found to be

$$z = l_c^2 \frac{z''}{(1 + z'^2)^{3/2}}, \tag{E.4}$$

where the capillary length is given by Equation (4.37) and the explicit dependencies on x are omitted. Integrating both sides gives:

$$\frac{1}{2} z^2 = -l_c^2 \frac{1}{\sqrt{1 + z'^2}} + C. \tag{E.5}$$

For $z = 0$, z' should also be 0, thus the integration constant is $C = l_c^2$. Solving for z', one finds:

$$\frac{dz}{dx} = \pm \sqrt{\left(\frac{1}{1 - \frac{z^2}{2 l_c}} \right)^2 - 1}. \tag{E.6}$$

From now on, we will only keep the solution with the minus sign in front, because of the same constraint as before. Unfortunately, this expression cannot be integrated easily in order to yield an analytic function for $z(x)$. An analytic solution for $x(z)$, however, does exist.

First, Equation (E.6) is rewritten in terms of dx/dz:

$$\frac{dx}{dz} = -\left[\left(\frac{1}{1 - \frac{z^2}{2 l_c}} \right)^2 - 1 \right]^{-1/2}. \tag{E.7}$$

Then, we define a dimensionless $Z \equiv z/l_c$:

$$\frac{1}{l_c} \frac{dx}{dZ} = -\left[\left(\frac{1}{1 - \frac{1}{2} Z^2} \right)^2 - 1 \right]^{-1/2}. \tag{E.8}$$

Finally, integration yields:

$$\frac{x(Z)}{l_c} = \frac{1}{l_c} \int \frac{dx}{dZ} dZ + C \tag{E.9}$$

$$= -\int \left[\left(\frac{1}{1 - \frac{1}{2} Z^2} \right)^2 - 1 \right]^{-1/2} dZ + C \tag{E.10}$$

$$= -\ln\left[\frac{2}{Z} - \sqrt{\left(\frac{2}{Z} \right)^2 - 1} \right] - \sqrt{4 - Z^2} + C \tag{E.11}$$

$$= \operatorname{arccosh}\left(\frac{2}{Z} \right) - \sqrt{4 - Z^2} + C. \tag{E.12}$$

From the interface touching the wall (i.e., $x = 0$) at a contact height $H \equiv h/l_c$, the integration constant C can be found:

$$\frac{x(H)}{l_c} = \operatorname{arccosh}\left(\frac{2}{H}\right) - \sqrt{4 - H^2} + C = 0. \tag{E.13}$$

Thus, $C = -\operatorname{arccosh}(2/H) + \sqrt{4 - H^2}$ and we find for $x(z)$:

$$\frac{x(z)}{l_c} = \operatorname{arccosh}\left(\frac{2l_c}{z}\right) - \operatorname{arccosh}\left(\frac{2l_c}{h}\right) - \sqrt{4 - \frac{z^2}{l_c^2}} + \sqrt{4 - \frac{h^2}{l_c^2}}, \tag{E.14}$$

that is, Equation (4.36).

The relation between the contact height h and the contact angle θ is deduced from the slope at $x = 0$ and $z = h$:

$$\left(\frac{\mathrm{d}z}{\mathrm{d}x}\right)_{z=h} = \frac{1}{\tan\theta}. \tag{E.15}$$

Using Equation (E.6),

$$h^2 = 2l_c^2\left(1 \pm \frac{1}{\sqrt{\frac{1}{\tan^2\theta} + 1}}\right). \tag{E.16}$$

Here, we will now keep the minus sign as the only solution, because h should be zero for $\theta = 90°$. Since $0° < \theta < 180°$, this can be simplified using standard trigonometry to

$$h^2 = 2l_c^2(1 - \sin\theta), \tag{E.17}$$

which is Equation (4.38).

From analyzing the shape of experimentally observed interfaces, their tension can be found. Using the edge detection algorithms from the Mathematica software package (version 9), the profile can be extracted from micrographs such as Figure 4.5. In principle, fitting to Equation (E.14) directly gives the capillary length. Given a known density difference between the two phases, the interfacial tension follows from Equation (4.37). However, a better fit can be found by numerically inverting Equation (E.14) to give a function $z(x)$ and using this to perform a least squares fit to the experimental data, because this minimizes the error $[z_{\mathrm{exp}}(x) - z(x)]^2$ instead of $[x_{\mathrm{exp}}(z) - x(z)]^2$. It is experimentally difficult to capture the interfacial profile very close to the wall. This does not influence the capillary length, but it will lead to a different apparent contact angle θ and contact height h. As such, the interfacial tension can still be determined accurately from the analysis of a partial profile.

CHAPTER 5

Water-in-Water Emulsions Stabilized by Nanoplates

Abstract

Ultrathin plate-like colloidal particles are effective candidates for Pickering stabilization of water-in-water emulsions, a stabilization that is complicated by the thickness and ultralow tension of the water–water interface. Here we present experiments and theory for the effect of gibbsite nanoplates on phase-separated aqueous solutions of biopolymers dextran and nongelling fish gelatin. Plate-like particles have the advantage of blocking much of the interface while simultaneously having a low mass. Additionally, the amount of blocked interface is practically independent of the equilibrium angle θ at which the water–water interface contacts the nanoplates, as opposed to the wetting of spheres. As a result, the adsorption of nanoplates is stronger than for spheres with the same maximal cross section, except at $\theta = 90°$.

5.1 Introduction

Many food products consist of an emulsified mixture of water and oil, for instance mayonnaise, and because of the oil, they have a high caloric content. For the preparation of novel low calorie foods, the oil could be replaced by a second aqueous phase. Aqueous two-phase systems, formed by the phase separation of two incompatible polymers in aqueous solution, are potential candidates for the creation of such foods, provided there is a way to make stable water-in-water emulsions. These would consist of droplets rich in one polymer, suspended in a continuous phase rich in the other polymer, while both phases would still be 90 % water.

Various aspects of water–water interfaces are distinctly different from oil–water interfaces. As discussed in Chapters 2 to 4, water–water interfaces are much thicker [25, 26, 32], have an ultralow tension [7, 29–31, 80, 81], and are permeable to water and small ions [75, 84]. Nicolai and co-workers [85] argue that traditional surfactant molecules are incapable of stabilizing water-in-water emulsions, as the typical length scale of the water–water interface can be of the order of 10 nm, much more than the size of a typical surfactant molecule. As such, stabilization is only possible with much larger structures, for instance colloidal particles that provide Pickering stabilization. As a result of tensions in the range of 0.01 to 10 µN/m, irreversible adsorption of colloids to the water–water interface requires particles with a larger cross section than in the case of the oil–water interface. As demonstrated in Chapter 2, the permeability of the interface may result in an electric potential difference between the two phases [52, 84] due to the Donnan equilibrium [39, 40] if one of the polymers is charged. In Chapter 4 it was shown that this potential difference reduces the interfacial tension; additionally it may affect the interfacial adsorption of charged particles [86, 87].

Poortinga [88] studied the adsorption of microparticles at the water–water interface for various combinations of microparticles and polymers. The interfacial adsorption was accompanied by an increase in emulsion stability and could be used in the preparation of colloidosomes. Nicolai and co-workers also observed accumulation of latex particles at the water–water interface in solutions of dextran and poly(ethylene oxide) but they did not observe enhanced emulsion stability. They concluded that the adsorption was driven by the interfacial tension [89]. In contrast, Firoozmand *et al.* [90] also observed interfacial accumulation of similarly sized latex particles in mixtures of gelatin and oxidized starch, but concluded that the interfacial tension was not high enough to explain the accumulation, even though the interfacial tensions of the two systems should be similar. In later work, Nicolai and co-workers found increased emulsion stability using particles made from proteins [91] and hydrogels [85]. Buzza *et al.* [92] also created stable water-in-water emulsions for a solution of dextran and poly(ethylene oxide), but they used block copolymers instead.

Here, we focus on aqueous mixtures of dextran and nongelling fish gelatin. The interface of this model system has been studied in detail, crucial for understanding the physics of emulsification [26, 52, 86, 87]. A complication for the preparation of water-in-water Pickering emulsions with dextran–gelatin solutions is that gelatin spontaneously adsorbs onto a wide range of materials [93], such as polystyrene, glass, and metals. If gelatin fully covers the surface of the colloidal particles, they are expected to accumulate in the gelatin-rich phase, not at the dextran–gelatin interface. Another complication is that, because of the low interfacial tension, particles with a large cross section are needed, while the particles should not have a too large (buoyant) mass, as this may lead to rapid sedimentation of both the particles and the emulsion droplets, diminishing emulsion stability.

Our approach here is to stabilize water-in-water emulsions using thin plate-like particles, which have the advantage of combining a low mass with a large surface area. We use colloidal gibbsite platelets, an aluminum hydroxide with a well-defined hexagonal shape that can be prepared with a relatively low polydispersity in size. Colloidal gibbsite has been studied extensively in past decades as a synthetic clay, and its chemical and physical properties are well understood [94–99]. The adsorption of plate-like particles at liquid–liquid interfaces, however, has received less attention in literature than the adsorption of spherical particles. Therefore, we will start by describing a theoretical model for the adsorption of arbitrarily shaped particles at liquid–liquid interfaces. We will then detail our experimental investigation of aqueous two-phase emulsions stabilized by gibbsite platelets, ending with a few conclusions about the stability of such emulsions. The Appendices following this Chapter give results of additional experiments and calculations.

5.2 Theory

In this section, we treat two cases of theory by Soligno *et al.* [100] for the adsorption of arbitrarily shaped colloidal particles at the liquid–liquid interface: the well-known case of spheres and the less investigated case of plate-like particles. Given a fixed position and orientation of the particle, the three-dimensional equilibrium shape of the interface is calculated numerically by minimizing the total interfacial energy of the system. Details of the numerical methods, including an implementation of the algorithms, are described in Ref. 100.

The total interfacial energy of a particle adsorbed at a macroscopically flat interface between a bottom phase α and a top phase β is given by

$$E = A_{\alpha\beta}\gamma + A_{\alpha \mathrm{p}}\gamma_{\alpha \mathrm{p}} + A_{\beta \mathrm{p}}\gamma_{\beta \mathrm{p}} + E_{\mathrm{g}}, \tag{5.1}$$

where $A_{\alpha\beta}$ is the area of direct contact between the two phases, γ is the tension

between the two phases, $A_{\alpha p}$ is the area of phase α in contact with the particle, $\gamma_{\alpha p}$ is the tension of the α–particle interface, $A_{\beta p}$ is the area between β and particle, and $\gamma_{\beta p}$ is the tension of the β–particle interface. Local deformation of the α–β interface depends on the shape, position, and orientation of the colloidal particle, and on the contact angle of the α–β interface with the particle. The gravitational energy E_g of the liquid–liquid interface is given by

$$E_g = \Delta\rho g \int_{V_\beta} z \, dV + C, \tag{5.2}$$

where $\Delta\rho$ is the density difference between the two phases, g is the gravitational acceleration, z is the height above the reference level $z = 0$, i.e., the level of the interface far away from the particle, and $z > 0$ into the top phase. The constant C is chosen such that E_g is zero if no particle is adsorbed and the interface is completely flat.

Using the capillary length l_c from Equation (4.37), the gravitational energy E_g can be written as

$$E_g = \frac{\gamma}{l_c^2} \int_{V_\beta} z \, dV + C. \tag{5.3}$$

We use our method to study the adsorption of spheres and hexagonally-shaped platelike particles. The spheres have a diameter d. The platelets have a thickness l and an equivalent circular diameter d, given by the diameter of a circle with the same area. By defining the diameters in this way, the platelets and spheres both reduce the area of contact between phases α and β by the same amount for a contact angle of 90°.

In our numerical calculations we consider small and large particles. For the small particles, $d = 167\,\text{nm}$ and $l = 6.6\,\text{nm}$, while for the large particles $d = 694\,\text{nm}$ and $l = 33\,\text{nm}$, numbers corresponding to our experimental platelets. Strictly speaking, also the gravitational energy of the particle itself should be included in Equation (5.1). However, the gravitational energy is negligible compared to the other terms even for the largest particles that we study[1]. We will use the parameters $\gamma = 4\,\mu\text{N/m}$ and $l_c = 0.6\,\text{mm}$ in our calculations, on the basis of experimental data from Chapter 4 that will be reiterated in Section 5.4. Examples of the equilibrium shape of the interface for a small sphere and a large platelet at fixed position and orientation are given in Figure 5.1. By calculating the interface shape for various particle positions and

[1]The gravitational energy of the particle is $E_p = \Delta m g z_c$, with Δm the buoyant mass and z_c the height of the center of mass above $z = 0$. Assuming $z_c \sim d$, we find $E_p = (\pi\gamma\Delta\rho_p d^3 l)/(4\Delta\rho l_c^2)$ where $\Delta\rho_p$ is the density difference of the particle with the liquid (since $\Delta\rho_p \gg \Delta\rho$, the density difference between the two phases can be disregarded for E_p). The total interfacial energy is of the order of $E_{int} \sim \gamma(A_{\alpha p} + A_{\beta p}) = \gamma(\frac{\pi}{2}d^2 + \pi d l)$. Thus, $E_p/E_{int} \sim (\Delta\rho_p/\Delta\rho)(d^2 l)/[2l_c^2(d + 2l)]$. When taking $\Delta\rho_p = 1500\,\text{kg/m}^3$, $\Delta\rho = 1\,\text{kg/m}^3$, $l_c = 0.6\,\text{mm}$, and d and l from the large platelets, $E_p/E_{int} \sim 10^{-5}$.

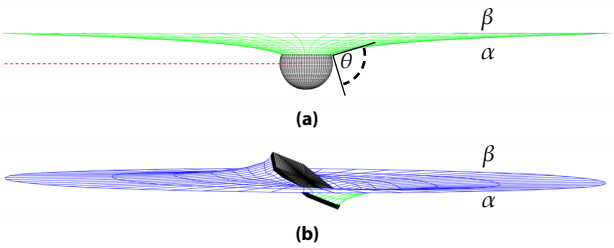

Figure 5.1: Examples of the equilibrium shape of the α–β liquid–liquid interface found by minimization of Equation (5.1), for a given non-equilibrium position and orientation of an adsorbed particle. (a) A small sphere ($d = 167$ nm, the center is indicated by a red dotted line) is positioned below the interface, which deforms to maintain the contact angle θ. (b) A large platelet ($d = 694$ nm and $l = 33$ nm) sits tilted at the interface at equilibrium height. In both cases the contact angle is 90°.

orientations, the equilibrium particle position and orientation is found as the one with minimum E (Equation (5.1)).

The adsorption energy ΔE_{ads} of a particle is defined as the change in energy when the particle goes from being fully immersed in one of the phases to being adsorbed at the interface in its equilibrium position and orientation. If the particle is preferentially wetted by the top phase β, then $\Delta E_{\text{ads}} = E - (A_{\alpha\text{p}} + A_{\beta\text{p}})\gamma_{\beta\text{p}} - A\gamma$, where $(A_{\alpha\text{p}} + A_{\beta\text{p}})\gamma_{\beta\text{p}}$ is the energy of a particle with total surface area $A_{\alpha\text{p}} + A_{\beta\text{p}}$ and which is fully immersed in phase β, and $A\gamma$ is the energy of the interface with area A when no particle is adsorbed. Therefore:

$$\Delta E_{\text{ads}} = -\gamma\left(A - A_{\alpha\beta} - A_{\alpha\text{p}}\frac{\gamma_{\alpha\text{p}} - \gamma_{\beta\text{p}}}{\gamma} - \frac{1}{l_{\text{c}}^2}\int_{V_\beta} z\,\mathrm{d}V\right) + C. \tag{5.4}$$

When θ is defined as the contact angle measured in phase α as indicated in Figure 5.1, $\theta = 0°$ if phase α fully wets the particle. Young's law states that $\cos\theta = -(\gamma_{\alpha\text{p}} - \gamma_{\beta\text{p}})/\gamma$, so that for $180° \geq \theta \geq 90°$

$$\Delta E_{\text{ads}} = -\gamma\left(A - A_{\alpha\beta} + A_{\alpha\text{p}}\cos\theta - \frac{1}{l_{\text{c}}^2}\int_{V_\beta} z\,\mathrm{d}V\right) + C. \tag{5.5a}$$

An analogous expression may be derived for ΔE_{ads} if phase α preferentially wets the particle, i.e., $90° \geq \theta \geq 0°$:

$$\Delta E_{\text{ads}} = -\gamma\left(A - A_{\alpha\beta} - A_{\beta\text{p}}\cos\theta - \frac{1}{l_{\text{c}}^2}\int_{V_\beta} z\,\mathrm{d}V\right) + C. \tag{5.5b}$$

Thus, the equilibrium shape of the interface can be found by numerical minimization of Equation (5.1) for a fixed particle position and orientation. By repeating

these calculations as a function of particle coordinates, the equilibrium position and orientation of the particle can be found and the adsorption energy can be calculated through Equation (5.5a) or (5.5b).

5.3 Experimental

5.3.1 Preparation of Samples

Preparation of the polymer solutions was detailed in Section 2.3.1. Samples consisted of dextran (100 kDa) and gelatin (gelling temperature 8 to 10 °C, 100 kDa) in a 1:1 or 3:1 (dextran to gelatin) mass ratio. The pH was 6.2 and the salt concentration approximately 5 mM, as deduced from conductivity measurements.

In the preparations of emulsions, a dispersion of colloidal gibbsite particles was added, so that the samples contained typically 1 % of gibbsite by mass. Normally samples were vortex mixed, although some (as will be indicated) were mixed with high shear using an IKA Ultra-Turrax. Colloidal gibbsite is composed of $Al(OH)_3$ and consists of hexagonally shaped, plate-like particles [94]. We used small and large gibbsite platelets that are colloidally stable due to their positive surface charge. The small particles had a diameter $d = 167 \pm 30$ nm and a thickness $l = 6.6 \pm 1.1$ nm. For the large gibbsite platelets the diameter was $d = 694 \pm 45$ nm, with l approximately 30 to 40 nm. The diameter of the platelets was measured using transmission electron microscopy on a Philips FEI Tecnai 10, see Figure 5.2, and it was defined as the diameter of a circle with the same area; the thickness was measured using atomic force microscopy on a Digital Instruments Multimode SPM MMAFM-2 operated in tapping mode. With the large platelets, aggregation upon drying complicated the determination of the thickness, so only an estimate is given. The particles were prepared from hydrothermal treatment of aluminum alkoxides in acidic environment using seeded growth [97, 101].

Emulsions prepared with the small platelets were imaged by confocal microscopy. The gelatin-rich phase could be visualized by the addition of a small amount of fluorescent dye, rhodamine B, as the dye resides preferentially in this phase. A small amount of fluorescein isothiocyanate–dextran (FITC–dextran, Sigma-Aldrich, 70 kDa) was added to some samples. FITC–dextran accumulates near the interface between dextran- and gelatin-rich phases, highlighting these interfaces [26]. A Nikon Eclipse TE2000-U confocal microscope was used with a 100× oil immersion objective and 488 and 543 nm lasers. Emulsions prepared with the large particles were imaged by optical microscopy to visualize particle attachment at the interface. We used a Nikon Eclipse Ti-E inverted microscope, equipped with a Nikon CFI Apo TIRF objective (100× magnification, N.A. 1.49) and a Hamamatsu ORCA-Flash4.0 V2 digital camera.

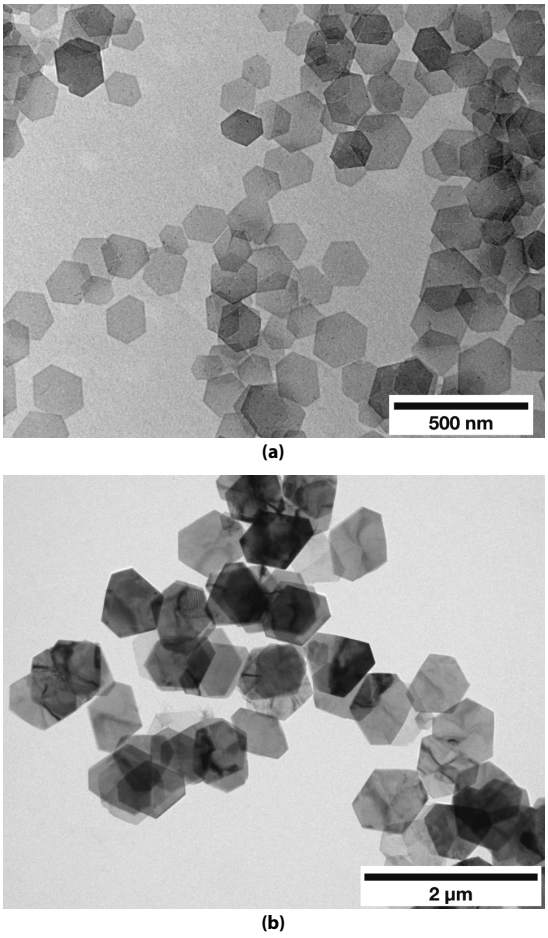

Figure 5.2: Transmission electron micrographs of (a) the "small" and (b) the "large" gibbsite platelets.

5.3.2 Determination of the Contact Angle

For spherical particles, the contact angle with the liquid–liquid interface may be determined from their position at the interface [89], but for our plate-like particles this is impossible due to their geometry. Therefore, we coated a glass slide with gibbsite using vertical deposition [102] and determined the macroscopic three-phase contact angle between the gelatin-rich phase, dextran-rich phase, and the gibbsite surface.

A microscope slide was cut to an appropriate size using a diamond pen. The glass was cleaned by immersion in a 1:1 mixture of methanol and fuming hydrochloric acid for an hour [103]. It was rinsed with Milli-Q water and dried under nitrogen flow. The slide was placed in a sample vial at an angle of, approximately, 30° and the vial was filled with a dilute dispersion of the small gibbsite platelets. The vial was placed on a heating plate of 100 °C and left overnight to evaporate, forming a hazy white multilayer of gibbsite platelets attached to the glass. Scanning electron micrographs of a coated glass slide, taken using a FEI XL30S FEG are shown in Appendix F. Prolonged immersion of such a slide in water did not appear to induce redispersion of the gibbsite platelets, indicating that the particles are aggregated in their primary minimum.

Phase-separated samples consisting of 5 % dextran and 5 % gelatin were prepared and their phases were isolated as described in the previous Chapters. A rectangular glass container was filled with the less dense dextran-rich phase and placed in a Dataphysics OCA 15 optical contact angle measuring setup. The glass slide was placed horizontally at the bottom of the container. A syringe, equipped with a needle with an outer diameter of 0.5 mm, was filled with the more dense gelatin-rich phase and placed in the dispense unit of the setup. The tip of the syringe was immersed in the dextran-rich phase and placed close to the gibbsite-coated glass. After dispensing a droplet of gelatin-rich phase of 1 µL at a rate of 1 µL/s, the tip was removed and the container was sealed with parafilm to prevent evaporation. After equilibration for several hours, the contact angle between the coated glass, dextran-rich continuous phase, and gelatin-rich droplet was determined from both the left and right sides of a cross section of the droplet. The process was repeated for several droplets and multiple gibbsite-covered glass plates. In total, the contact angles of ten different gelatin-rich droplets were analyzed. As a control, droplets were also placed on a glass surface that was cleaned in the same way but was not coated with gibbsite.

5.3.3 Characterization of Polymer Adsorption

The adsorption of dextran and gelatin onto gibbsite platelets was characterized by measuring the hydrodynamic (Stokes) diameters of gibbsite platelets in pure water, in dilute solutions of dextran, and dilute solutions of gelatin. Additionally, the hydrodynamic radii of the polymers dextran and gelatin were measured.

Samples used for dynamic light scattering (DLS) consisted for approximately 0.05 % of small gibbsite platelets by mass and optionally 0.1 % of either dextran or gelatin and were measured in a disposable polystyrene cuvette. A scattering angle of 173° was selected and the volume-averaged hydrodynamic radii were computed based on 8 measurements on the same sample and cuvette. A refractive index of 1.57 was assumed for the gibbsite [59]. The light scattering apparatus was a Malvern Zetasizer Nano ZS. The concentration of polymer was approximately a fourfold surplus for the formation of a monolayer on each platelet.

For measurement of the hydrodynamic radii of dextran and gelatin, a solution of 10 % dextran or 10 % gelatin was centrifuged briefly to sediment possible dust towards the bottom of the container. Part of the solution was diluted to approximately 1 % and transferred to a disposable polystyrene cuvette and measured as before.

The viscosities of solutions of dextran or gelatin were measured on an Anton Paar MCR-300 rheometer. The viscosities at 0.1 % were indistinguishable from that of water (1.0 mPa s), whereas those at approximately 1 % were 1.3 mPa s and 1.6 mPa s for dextran and gelatin, respectively. Data were processed using the "general purpose" method of the Malvern Zetasizer software, version 7.11.

5.4 Results

First, the macroscopic effects of adding colloidal gibbsite platelets to aqueous mixtures of dextran and gelatin are described. Subsequently, the microscopic structure is analyzed. To clarify the observed effects, we present measurements on the interfacial properties and on the triphasic contact angle between dextran-rich phase, gelatin-rich phase, and gibbsite. Finally, we analyze the adsorption of dextran and gelatin polymer chains onto gibbsite.

5.4.1 Macroscopic Effects

The macroscopic effect of adding gibbsite to an aqueous mixture of dextran and gelatin can be seen in Figure 5.3. For the samples with a 1:1 ratio of dextran and gelatin (Figures 5.3a and 5.3b), most of the macroscopic dextran-rich top phase disappears upon addition of small gibbsite platelets, while a highly turbid layer appears inside the bottom phase. This indicates that the top phase is partly emulsified into the bottom phase. For the 3:1 dextran to gelatin ratio (Figures 5.3c and 5.3d), the whole sample becomes turbid, indicating that small platelets emulsify the complete gelatin-rich bottom phase into the top phase. For large platelets (Figure 5.3e), a small amount of top phase is emulsified in the bottom phase, indicating that the large platelets are less effective for the stabilization of water-in-water emulsions. For all of these samples, an

increase or decrease in the amount of gibbsite by 50 % did not significantly change the amount of emulsified phase. It should be noted that a dispersion of the small gibbsite platelets at this concentration in pure water is only slightly opaque. As such, the turbidity of the samples points to the formation of water-in-water structures on length scales larger than the size of the platelets. The samples still flowed when the tubes were tilted and appeared to remain unchanged for weeks.

5.4.2 Microscopy of Emulsion Droplets

The microscopic structure of the samples was investigated by confocal and optical microscopy. Figures 5.4a to 5.4c show confocal micrographs of dextran–gelatin mixtures with small gibbsite platelets, where the gelatin-rich phase has been stained red with rhodamine B. In Figures 5.4a and 5.4c the interface is highlighted in green due to the addition of FITC–dextran, which accumulates at the interface [26]. At low gibbsite concentrations, large spherical gelatin-rich droplets of approximately 40 µm are visible together with some smaller droplets (Figure 5.4a). Increasing the gibbsite concentration by a factor of two leads to irregularly shaped droplets with a size in the range of 10 to 20 µm, which suggests that the interface is densely covered with platelets (Figure 5.4b). The use of high-shear mixing makes the droplets more spherical (Figure 5.4c), see also Movie H.1 (weblink in Appendix H).

While the large gibbsite platelets seem less efficient at emulsion stabilization than their smaller counterparts, they have the advantage of being observable under an

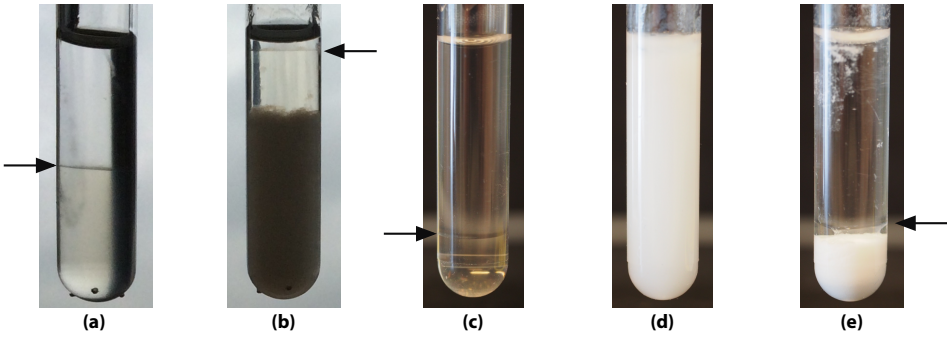

Figure 5.3: Effect of colloidal gibbsite on the macroscopic phase separation of aqueous mixtures of dextran and gelatin into a dextran-rich top phase and gelatin-rich bottom phase. The mixtures consist of (a, b) 6.0 % dextran and 6.0 % gelatin, and (c–e) 9.0 % dextran and 3.0 % gelatin. The mixtures contain (a, c) no gibbsite, (b, d) approximately 1 % of small gibbsite, and (e) 1 % of large gibbsite. The macroscopic water–water interface—if present—is indicated by a black arrow. The tubes have an outer diameter of 1.2 cm.

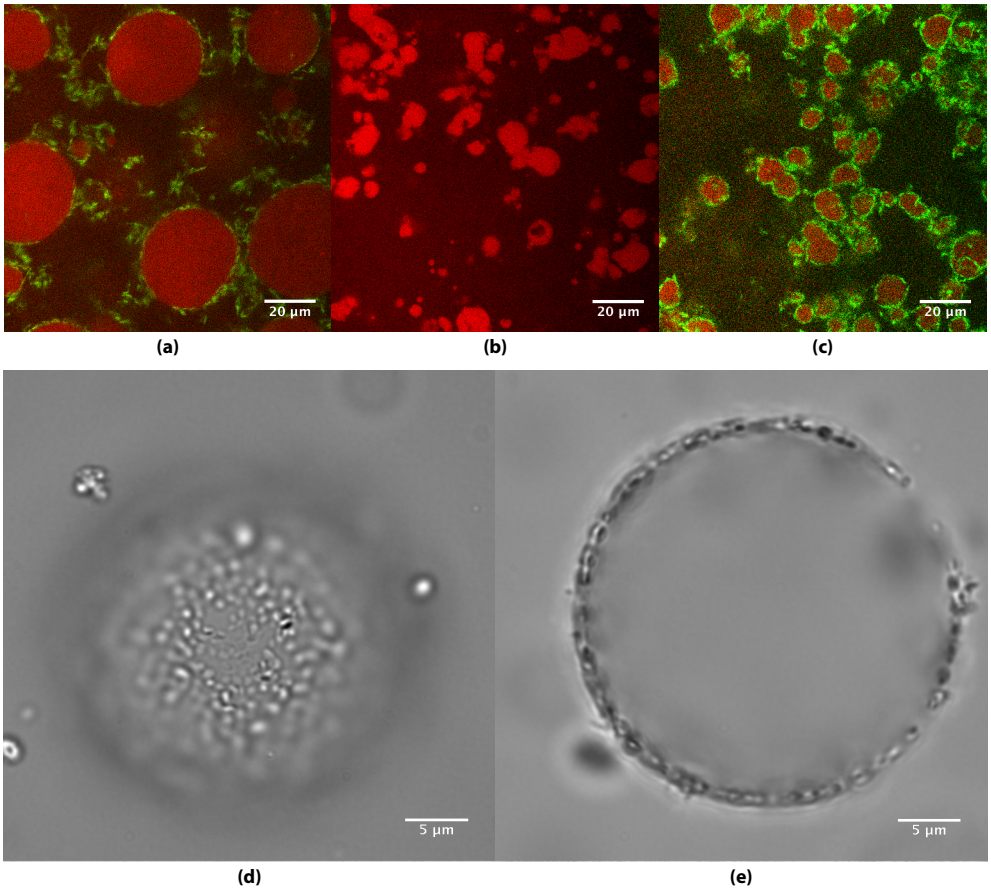

Figure 5.4: Water-in-water emulsions stabilized by colloidal gibbsite imaged using microscopy. (a–c) Confocal micrographs of a mixture of 9 % dextran, 3 % gelatin, and (a) 0.4 % and (b, c) 1 % small gibbsite. The droplets are gelatin-rich (dyed with rhodamine B, red) and are immersed in a continuous dextran-rich phase. The samples were also dyed (a, c) with FITC–dextran (green), which locates preferentially at the droplet edges. The samples were prepared (a, b) using vortex mixing and (c) using high shear mixing. (d, e) Optical micrographs of 5 % dextran and 5 % gelatin and large gibbsite platelets; the droplet is dextran-rich and is immersed in a continuous gelatin-rich phase. The droplet is imaged (d) at the bottom and (e) in the middle (cross section). The gibbsite platelets still exhibit Brownian motion while adsorbed at the interface (see Appendix H).

optical microscope. Figures 5.4d and 5.4e show the bottom and cross section of a droplet in an aqueous dextran–gelatin mixture in the presence of large platelets; Movie H.2 shows the droplet imaged at different heights. The platelets are clearly adsorbed at the water–water interface, forming a dense layer stabilizing the droplet, except near the top of the droplet, where fewer particles are present. Most of the particles appear to be adsorbed parallel to the interface and they still show Brownian motion, as can be seen in Movies H.3 to H.5.

5.4.3 Interfacial Tension

Since the tension of water–water interfaces is generally ultralow, one may wonder whether the interfacial tension alone is high enough to expect the adsorption of particles. Figure 5.5 reiterates the interfacial tension measurements from Chapter 4, but now presented as a function of the total polymer mass fraction at a 1:1 dextran to gelatin mass ratio, in addition to the capillary length l_c and density difference $\Delta\rho$. For a typical total mass fraction of polymer of 10 %, the interfacial tension is $4.85 \pm 0.24\,\mu N/m$. We will discuss the magnitude of the interfacial tension with regards to particle adsorption in the discussion section.

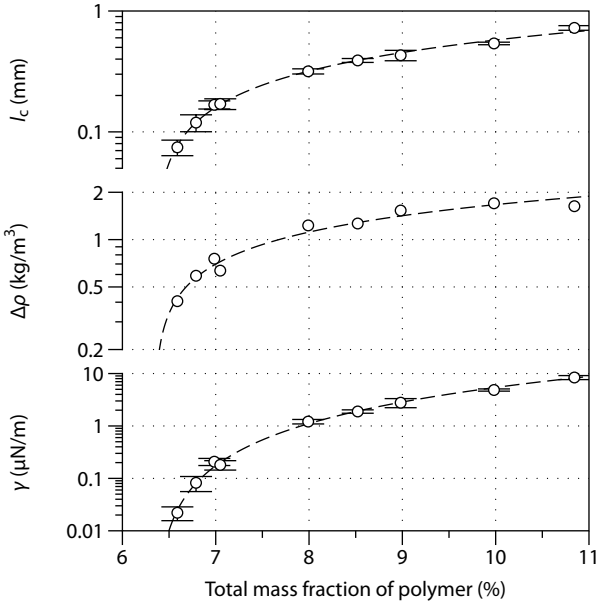

Figure 5.5: Interfacial properties of coexisting aqueous solutions of dextran and gelatin. Capillary length l_c, density difference $\Delta\rho$, and interfacial tension γ are presented as a function of total mass fraction of polymer. Dextran and gelatin are present in a global 1:1 mass ratio.

5.4.4 Contact Angle

For determination of the contact angle, a gibbsite-coated glass slide was immersed into an isolated dextran-rich phase, and gelatin-rich droplets were placed on it, as shown in Figure 5.6a. Scanning electron micrographs of a gibbsite-coated glass slide are given in Figure F.1 and the equilibration of a droplet is shown in Movie H.6. We found a contact angle of, on average, $89 \pm 15°$. In order to investigate possible pinning of the droplet, we increased the volume of a droplet stepwise and allowed for equilibration of the contact angle after each step. With this method we also consistently found a contact angle of approximately 90° after each step (Movie H.7). When droplets were placed instead on a clean, uncoated glass slide, (nearly) full wetting was observed as shown in Figure 5.6b. Note that this image was taken well before the droplet stopped spreading: otherwise it would have become so flat that it would be practically invisible; for examples see Movies H.8 and H.9. Therefore, the contact angle is in this case even smaller than depicted. Full wetting was also observed on many other surfaces, such as the wall of the polystyrene cuvette used for the determination of the interfacial tension or the metal needle of the syringe used to dispense the droplets.

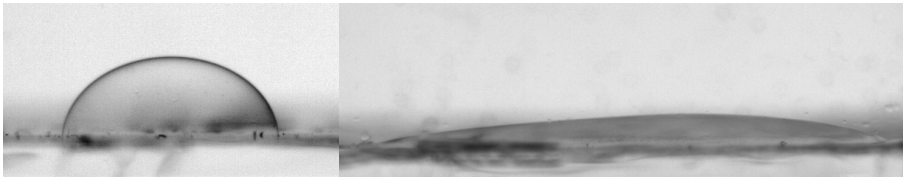

Figure 5.6: Water-in-water droplets showing the contact angle on (a) gibbsite-covered glass and (b) plain glass. The continuous phase is dextran-rich while the droplet is gelatin-rich. The two phases were formed from an aqueous mixture of 5 % dextran and 5 % gelatin. In both cases the droplet has a volume of 1 µL. The contact angle on gibbsite covered glass, averaged over many such droplets, is $89 \pm 15°$, whereas nearly full wetting is observed on plain glass ($\theta \lesssim 10°$, the droplet continues to spread out much more than shown here, see Appendix H).

5.4.5 Adsorption of Dextran and Gelatin onto Gibbsite

It is well known that gelatin polymer chains adsorb readily onto a wide range of surfaces [93]. An adsorbed layer of gelatin would likely induce full wetting of a surface by a gelatin-rich droplet. The observation of a contact angle close to 90° with gibbsite points either to the absence of adsorption of both dextran and gelatin on this material, or to the adsorption of both polymers to roughly the same degree. We characterized the adsorption of dextran and gelatin onto the small gibbsite platelets by measuring the hydrodynamic diameter D_h of the gibbsite platelets using DLS in pure

water, in a dilute solution of dextran, and in a dilute solution of gelatin. Additionally, we also determined the hydrodynamic diameters of the dextran and gelatin polymer chains.

The hydrodynamic diameter of a cylinder or disk with diameter d and thickness l can be calculated from [104]:

$$D_\mathrm{h} = \frac{3}{2} d \left[\sqrt{1 + \left(\frac{l}{d}\right)^2} + \frac{d}{l} \operatorname{arcsinh}\left(\frac{l}{d}\right) - \frac{l}{d} \right]^{-1} . \tag{5.6}$$

When a monolayer of polymer adsorbs to the gibbsite platelets and this polymer remains approximately spherical, d and l increase by twice the hydrodynamic diameter of the polymer, as sketched in Figure 5.7.

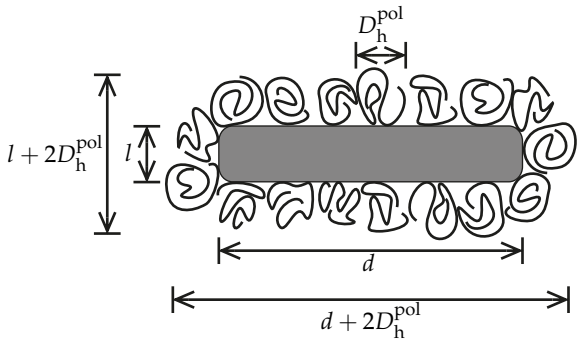

Figure 5.7: Schematic representation of polymer adsorption on a disk-like particle. The bare platelet has a diameter d and thickness l. Upon adsorption of a monolayer of polymer with hydrodynamic diameter $D_\mathrm{h}^\mathrm{pol}$, both the diameter and thickness of the platelet are increased by $2D_\mathrm{h}^\mathrm{pol}$.

The measured and calculated hydrodynamic diameters are shown in Table 5.1. For gibbsite in water, there is excellent agreement between the measured and calculated values, showing the aptness of Equation (5.6). For gibbsite in a solution of dextran, we observe a significant increase of the hydrodynamic diameter, which conforms very well to the calculated value. The increase in D_h translates to a dextran layer thickness of approximately 8.4 nm. This indicates that indeed a monolayer of dextran is adsorbed onto the gibbsite. For gibbsite with gelatin, an even larger increase in the hydrodynamic diameter is observed, which is not reproduced by the calculations. This increase implies a gelatin layer thickness of 34 nm, 3.5 times the D_h of gelatin in solution, a similar thickness as observed by others [93]. This either points to the adsorption of a multilayer of gelatin, or to the formation of a relatively densely packed monolayer where the gelatin chains are extended into solution. From our

data, it is impossible to distinguish between the two scenarios. It should be noted that such severely extended chains cannot be formed by dextran, as it is a branched polymer. Since we carried out our experiments using approximately a fourfold excess of polymer—compared to the formation of a monolayer of adsorbed polymer—this means that a large fraction of all gelatin is adsorbed onto the particles, whereas three quarters of the dextran remains in solution. Nevertheless, our measurements do indicate that both dextran and gelatin adsorb to gibbsite, in line with the observed contact angle close to 90°.

Table 5.1: Adsorption of dextran and gelatin on colloidal gibbsite platelets as determined from DLS. The hydrodynamic diameter D_h of gibbsite platelets was measured in water, in aqueous solutions of dextran, and in aqueous solutions of gelatin. The hydrodynamic diameter of aqueous dextran and aqueous gelatin was also measured. The values are the average and standard deviation of eight measurements. The hydrodynamic diameters of the gibbsite platelets in water were calculated using Equation (5.6), assuming dimensions of $d = 167$ nm and $l = 6.6$ nm. To calculate D_h for platelets in polymer solutions, the hydrodynamic diameter of the polymer was added twice to the diameter and thickness of the platelet.

	hydrodynamic diameter D_h (nm)	
	measured	calculated
dextran in water	8.2 ± 1.1	–
gelatin in water	9.8 ± 0.8	–
gibbsite in water	128.1 ± 1.3	127.4
gibbsite in dextran solution	146.5 ± 0.7	146.1
gibbsite in gelatin solution	205 ± 3	149.6

5.5 Discussion

Due to the peculiar properties of the water–water interface, it is a challenge to create kinetically stable water-in-water Pickering emulsions. The ultralow interfacial tension necessitates the use of particles with a large surface area, but the weight of such particles may prohibit stabilization, e.g., because the gravitational length of the particles is too small with respect to the size of the emulsion droplets or because the emulsion droplets become too heavy. An aspect specific to dextran–gelatin aqueous two-phase systems is that one of the polymers adsorbs strongly onto many materials, which might have been expected to lead to a contact angle close to zero diminishing the adsorption energy of particles at the interface. In the following, we discuss the use of plate-like particles to stabilize water-in-water emulsions, examining the effects

of the wetting angle, the size of the platelets, and the finite width of the water–water interface.

Using our numerical approach outlined in the theory section, the adsorption energy for plate-like-particles can be calculated for various orientations, to find the optimal orientation. Examples of the equilibrium shape of the interface for various platelet orientations are given in Figure 5.8a for a contact angle of 90°. As expected, the adsorption energy of the platelet is the highest when the particle is oriented parallel to the interface, since in this orientation it screens the largest amount of interfacial area between α and β, while at the same time minimizing the deformation of the interface (see also Figures G.3 to G.7 of Appendix G). This is in line with the experimental observations that the majority of the platelets appear to lie parallel to the interface.

The adsorption energy also depends on the contact angle θ of the interface with the particle. For spheres, the amount of blocked interface depends strongly on the contact angle. However, for platelets the amount of blocked interface is practically independent of the contact angle θ, because the rim of a platelet can accommodate almost any contact angle, as sketched in Figure 5.8b. The adsorption energy is still a function of the contact angle, because a change in the contact angle entails different tensions of the solid–liquid interfaces. This is reflected in our numerical calculations of the adsorption energy (in units of the thermal energy kT) for small platelets and spheres, displayed in Figure 5.8c. For these calculations we used the equilibrium particle position and orientation, i.e., parallel to the interface, and we assumed a tension of 4 μN/m. While for $\theta = 90°$ the adsorption energy of platelets is equal to that of spheres (approximately $-21kT$), the adsorption energy of platelets becomes higher than that of spheres when the contact angle deviates from 90°. Analogous calculations for large platelets and spheres show the same trend, with ΔE_{ads} about $-370kT$ for $\theta = 90°$. The results of these calculations and the ratio between the adsorption energies of platelets and spheres are given in Figures G.1 and G.2, respectively. The hexagonal shape of the platelets is not essential for these results and disk-like particles will behave similarly.

To gain further insight, we consider an approximation of the adsorption energy given by Equation (5.5), assuming an undeformed interface. The change in the amount of liquid–liquid interface when a colloidal particle adsorbs, $A - A_{\alpha\beta}$, is then the interfacial area blocked by the particle and the gravitational energy, E_{g}, is zero. For spheres, $A - A_{\alpha\beta}$ depends on the contact angle and is given by $(\pi/4)d^2 \sin^2\theta$. The amount of solid–liquid interface created due to the adsorption of the sphere is given by $(\pi/2)d^2(1 \pm \cos\theta)$, for $A_{\alpha\text{p}}$ (plus sign) or $A_{\beta\text{p}}$ (minus sign). Thus,

$$\Delta E_{\text{ads}}^{\text{sphere}} \approx -\frac{\pi}{4} d^2 \gamma (1 - |\cos\theta|)^2, \tag{5.7}$$

which is the well-known Pieranski equation [105]. On the other hand, the rim of our

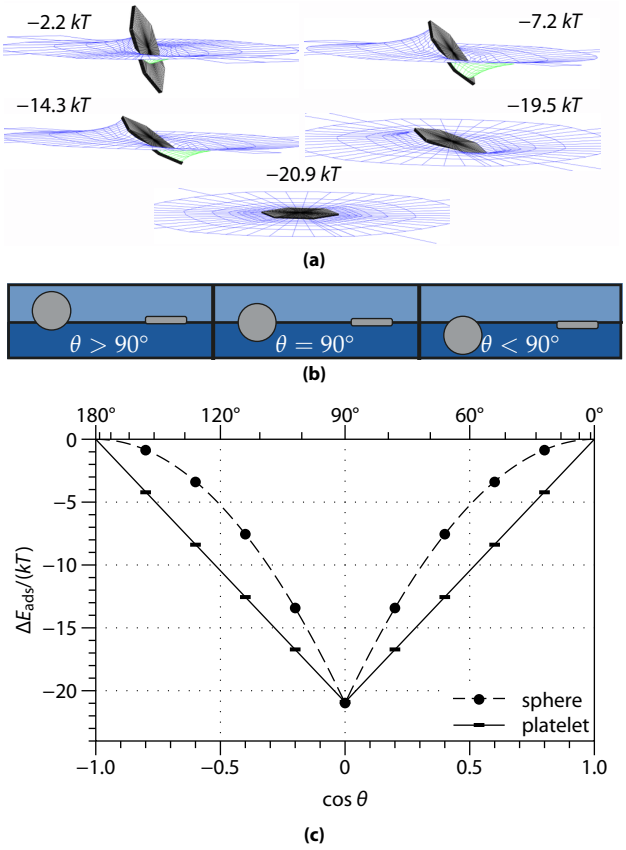

Figure 5.8: (a) Equilibrium shape of the interface for a small platelet adsorbed at the interface calculated under various orientations for a contact angle of 90°. The configuration with the lowest energy is when the particle is adsorbed parallel to the interface: the amount of blocked interfacial area is maximized and the interfacial deformation is minimized. (b, c) Comparison between the adsorption of small platelets and spheres of equal cross section at the liquid–liquid interface. (b) Schematic representation and (c) comparison of the adsorption energies in units of kT. The interfacial area covered by a platelet is practically independent of the contact angle θ, which for $\theta \neq 90°$ leads to higher adsorption energies for platelets than for spheres. Varying θ for platelets does however imply a change in tension of the solid–liquid interfaces and therefore a change in ΔE_{ads}. The points are the results of numerical calculations (see Section 5.2), the dashed line is a fit to Equation (5.7), and the solid line is a fit to Equation (5.8).

ultrathin plate-like particles can accommodate almost any contact angle. Therefore, $A - A_{\alpha\beta}$ is constant regardless of θ and equal to the area of the platelet, $(\pi/4)d^2$. Neglecting the thickness of the platelets, $A_{\alpha \mathrm{p}}$ and $A_{\beta \mathrm{p}}$ are also given by $(\pi/4)d^2$. It follows that

$$\Delta E_{\mathrm{ads}}^{\mathrm{platelet}} \approx -\frac{\pi}{4} d^2 \gamma (1 - |\cos\theta|). \tag{5.8}$$

For spheres the adsorption energy scales quadratically with $1 - |\cos\theta|$, whereas for platelets it scales linearly, in line with the numerical calculations of Figure 5.8c. Compared to spheres, the linear scaling of the adsorption energy of platelets leads to higher adsorption energies in situations where the contact angle is not 90°.

In the experiments, the small platelets appear to stabilize emulsions better than the large platelets, even though the latter have an adsorption energy that is an order of magnitude higher. The adsorption energy of the small platelets is already enough for practically irreversible adsorption, so the stronger adsorption of the larger platelets is expected neither to help nor to harm stabilization. However, the gravitational length of the two sizes of platelets is very different, as defined by $l_{\mathrm{g}} = kT/(\Delta m g)$, with Δm the buoyant mass of the particle and g the gravitational acceleration. The small platelets have a gravitational length of 2 mm, whereas for the large platelets it is less than 20 µm. Since the latter is comparable to the size of emulsion droplets, this visibly leads to an inhomogeneous coverage of the emulsion droplets, which may impair effective emulsion stabilization. On the other hand, the irregularly shaped emulsion droplets obtained with the small platelets imply a dense coverage and stabilization of the emulsion droplets due to crowding. Although a dense coverage alone not necessarily guarantees a stable emulsion [106], the emulsions obtained here appear stable for weeks.

The water–water interface has other unusual characteristics besides an ultralow tension. It can carry an electric potential difference due to the Donnan effect [39, 40] and has a typical width comparable to the size of the polymer coils, roughly 10 nm. The electric potential difference reduces the interfacial tension [86] and may impact the adsorption of charged colloidal particles. However, under the present pH and salt concentration, we have shown in Chapter 2 that this Donnan potential is less than 1 mV [52], which we consider negligible here. The thickness of the interface is comparable to the thickness of our platelets, but current knowledge as to how this affects their adsorption appears to be very limited and future research into this area is warranted. From that point of view it is interesting to observe that adsorption at a water–water interface is actually possible for such thin particles.

There is current interest in the preparation of kinetically stable water-in-water emulsions as a novel way of structuring water for next-generation low-fat food products. Even though not all ingredients of the particular system that we studied are

food-grade, incompatible combinations of food-grade biopolymers do exist. The development of suitable food-grade plate-like particles [107] will be a major part of the challenge to formulate novel food-grade water-in-water Pickering emulsions.

5.6 Conclusions

We have shown that colloidal gibbsite platelets stabilize water-in-water emulsions formed by aqueous mixtures of dextran and gelatin. While the tension of water–water interfaces is generally regarded as ultralow, it is high enough for the irreversible adsorption of gibbsite nanoplates. The use of larger gibbsite platelets is beneficial for optical investigations, but their increased weight ultimately leads to less effective stabilization of water-in-water emulsions. The contact angle of our gibbsite platelets is close to 90°, yielding the highest possible adsorption energies. For contact angles different from 90°, numerical calculations predict that platelets are more strongly adsorbed to the interface than spheres with an equivalent diameter, because the amount of screened interfacial area by platelets remains constant regardless of the contact angle. In addition, ultrathin platelets add much less mass to the stabilized emulsion droplets than comparable spheres, reducing gravity-driven coalescence. Our results show that plate-like colloidal particles have the potential to stabilize prospective food-grade water-in-water emulsions.

APPENDIX F

Scanning Electron Micrographs of Coated Glass Slides

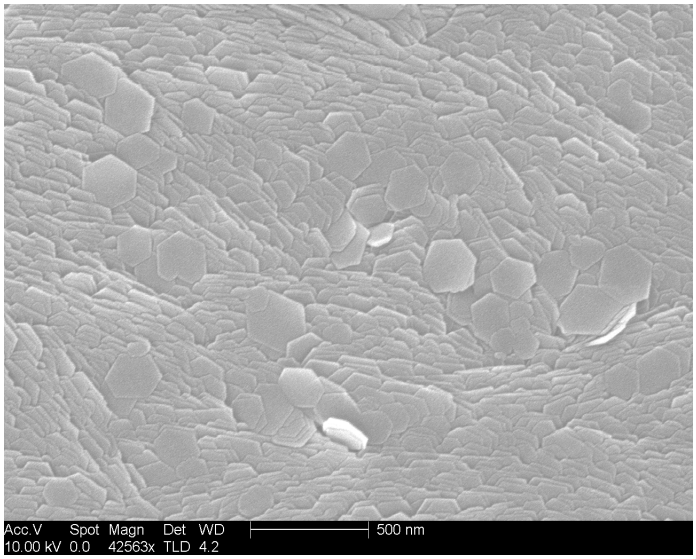

(a)

Figure F.1: Scanning electron micrographs of a glass substrate coated with small gibbsite platelets using vertical deposition [102].

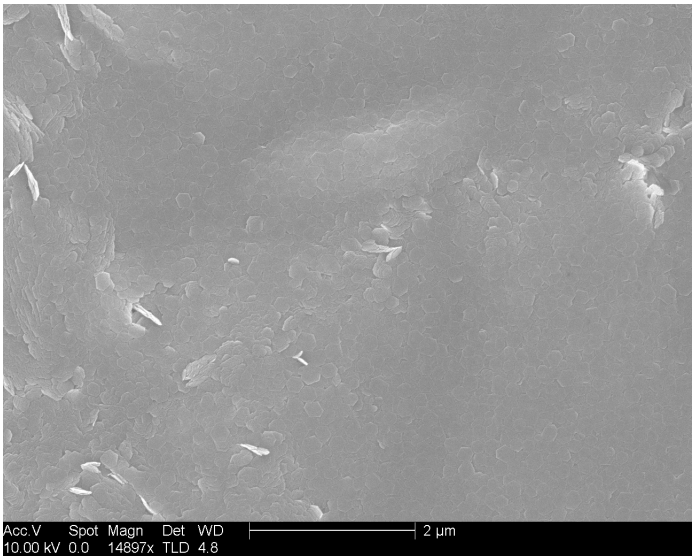

(b)

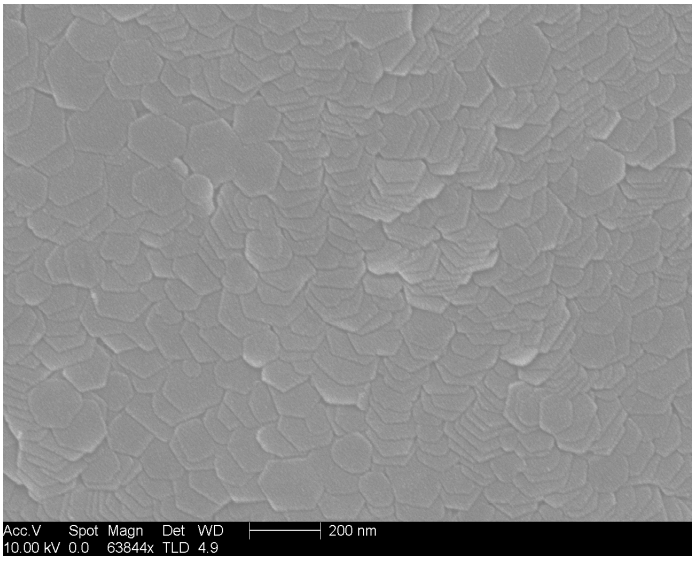

(c)

Figure F.1: Scanning electron micrographs of a glass substrate coated with small gibbsite platelets using vertical deposition [102] (continued).

APPENDIX G

Adsorption Energies of Spheres and Platelets

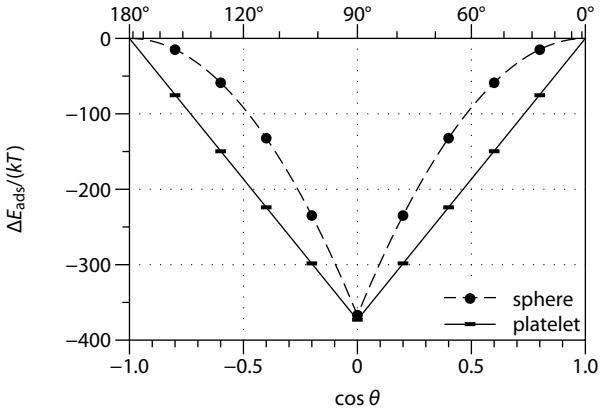

Figure G.1: Adsorption energy of the large platelets and large spheres with the same cross section as a function of the contact angle θ.

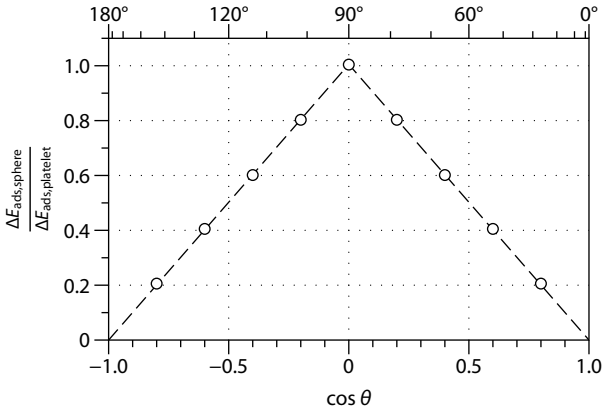

Figure G.2: Ratio between the adsorption energy of the small platelets and small spheres with the same cross section as a function of the contact angle θ. The equivalent graph for the *large* platelets and spheres is indistinguishable.

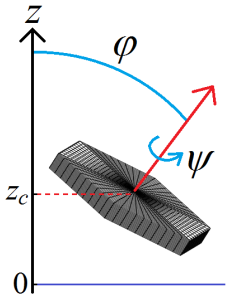

Figure G.3: Sketch of the geometrical configuration of a single colloidal particle adsorbed at a fluid–fluid interface. Here z_c is the height of the particle center of mass on the interface reference level, that is the interface level far from the particle (where $z = 0$). The polar angle of the particle vertical axis with respect to the normal of the unperturbed interface is φ. The internal Euler angle of the particle around its vertical axis is ψ.

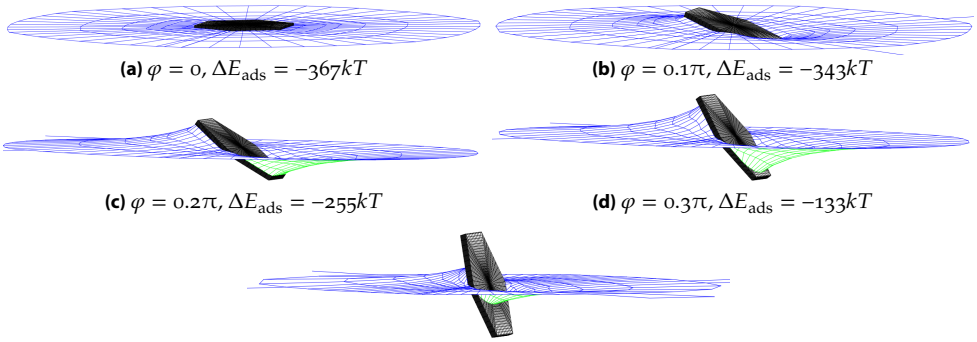

(a) $\varphi = 0$, $\Delta E_{\text{ads}} = -367kT$

(b) $\varphi = 0.1\pi$, $\Delta E_{\text{ads}} = -343kT$

(c) $\varphi = 0.2\pi$, $\Delta E_{\text{ads}} = -255kT$

(d) $\varphi = 0.3\pi$, $\Delta E_{\text{ads}} = -133kT$

(e) $\varphi = 0.4\pi$, $\Delta E_{\text{ads}} = -50kT$

Figure G.4: Adsorption energy of a large platelet under various angles φ for $\psi = 0$ and a contact angle of $\theta = 90°$.

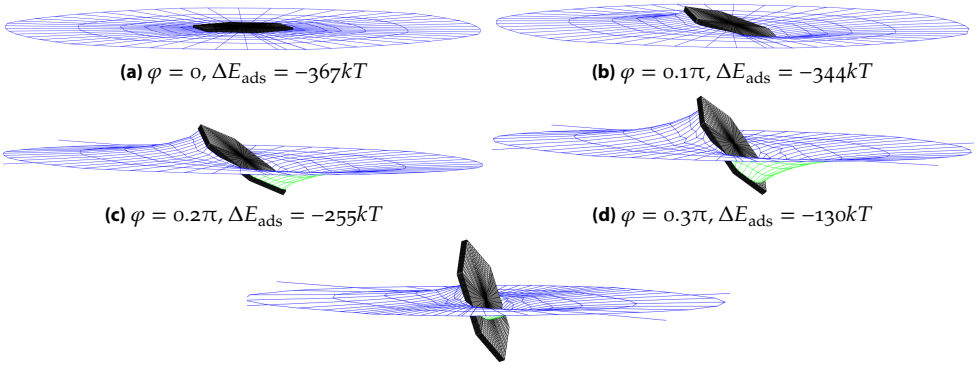

(a) $\varphi = 0$, $\Delta E_{\text{ads}} = -367kT$

(b) $\varphi = 0.1\pi$, $\Delta E_{\text{ads}} = -344kT$

(c) $\varphi = 0.2\pi$, $\Delta E_{\text{ads}} = -255kT$

(d) $\varphi = 0.3\pi$, $\Delta E_{\text{ads}} = -130kT$

(e) $\varphi = 0.4\pi$, $\Delta E_{\text{ads}} = -42kT$

Figure G.5: Adsorption energy of a large platelet under various angles φ for $\psi = \pi/6$ and a contact angle of $\theta = 90°$.

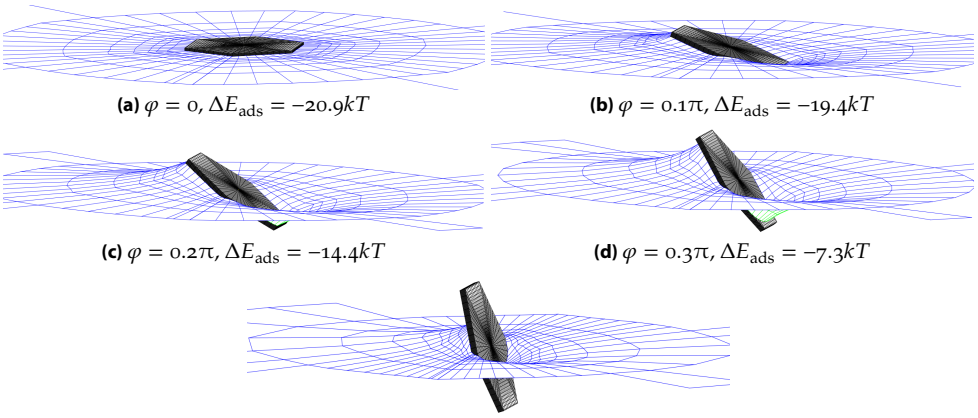

(a) $\varphi = 0$, $\Delta E_{\text{ads}} = -20.9kT$

(b) $\varphi = 0.1\pi$, $\Delta E_{\text{ads}} = -19.4kT$

(c) $\varphi = 0.2\pi$, $\Delta E_{\text{ads}} = -14.4kT$

(d) $\varphi = 0.3\pi$, $\Delta E_{\text{ads}} = -7.3kT$

(e) $\varphi = 0.4\pi$, $\Delta E_{\text{ads}} = -2.6kT$

Figure G.6: Adsorption energy of a small platelet under various angles φ for $\psi = 0$ and a contact angle of $\theta = 90°$.

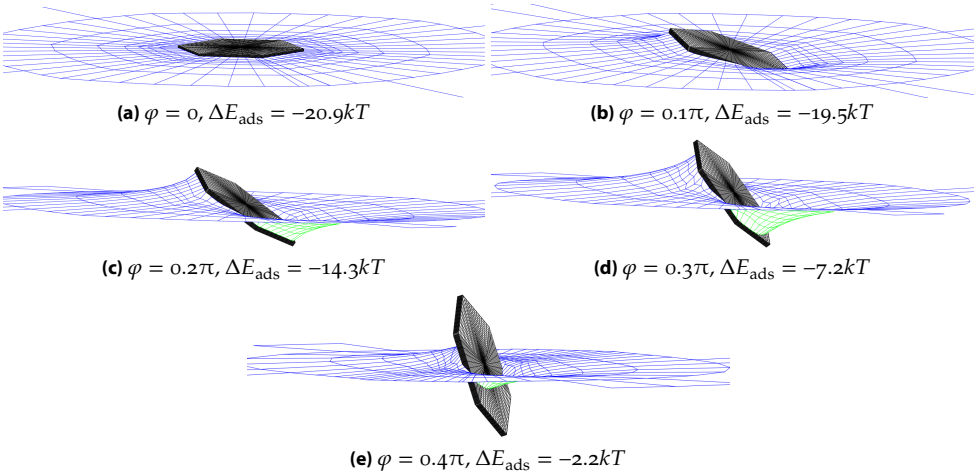

(a) $\varphi = 0$, $\Delta E_{\text{ads}} = -20.9kT$

(b) $\varphi = 0.1\pi$, $\Delta E_{\text{ads}} = -19.5kT$

(c) $\varphi = 0.2\pi$, $\Delta E_{\text{ads}} = -14.3kT$

(d) $\varphi = 0.3\pi$, $\Delta E_{\text{ads}} = -7.2kT$

(e) $\varphi = 0.4\pi$, $\Delta E_{\text{ads}} = -2.2kT$

Figure G.7: Adsorption energy of a small platelet under various angles φ for $\psi = \pi/6$ and a contact angle of $\theta = 90°$.

APPENDIX H

Supplementary Movies

The movies below are available at http://dx.doi.org/10.17026/dans-zt2-66a4.

Movie H.1: Confocal micrographs of a water-in-water emulsion with small gibbsite platelets at different heights. The total z-range is 70 µm.

Movie H.2: Optical micrographs of a water-in-water droplet with large gibbsite platelets, focussed at different heights. The total z-range is 38.4 µm.

Movie H.3: Optical micrographs of Brownian motion of large gibbsite platelets at the interface at the bottom of a water-in-water droplet. The movie is real time.

Movie H.4: Optical micrographs of Brownian motion of large gibbsite platelets at the interface at the center of a water-in-water droplet. The movie is real time.

Movie H.5: Optical micrographs of Brownian motion of large gibbsite platelets at the interface in-between the bottom and center of a water-in-water droplet. The movie is real time.

Movie H.6: Formation and equilibration of a 1 µL gelatin-rich droplet in a dextran-rich continuous phase on a gibbsite-coated glass substrate. The movie is accelerated 250×.

Movie H.7: Formation and equilibration of a 1 µL gelatin-rich droplet in a dextran-rich continuous phase on a gibbsite-coated glass substrate. The volume of the gelatin-rich droplet is increased in successive steps of 1 µL. The movie is accelerated 250×.

Movie H.8: Formation and equilibration (spreading) of a 1 µL gelatin-rich droplet in a dextran-rich continuous phase on a clean glass substrate. The movie is accelerated 750×.

Movie H.9: Formation and equilibration (spreading) of a different 1 µL gelatin-rich droplet in a dextran-rich continuous phase on a clean glass substrate. The movie is accelerated 750×.

Summary

Phase separation is commonly observed when two different polymers are present in aqueous solution, forming aqueous two-phase systems which typically consist for 90 % of water. Understanding these mixtures is essential to develop technological applications, for instance to isolate sensitive biological compounds using aqueous two-phase systems, or to prevent the phase separation of polysaccharides and proteins in food products, or to create novel oil-free water-in-water emulsions. For solutions of two uncharged polymers, phase separation generally occurs due to the combination of a positive mixing enthalpy and a relatively low mixing entropy. Segregative phase separation results, with each phase enriched in one of the polymers. For solutions of two oppositely charged polyelectrolytes, the attractive electrostatic interactions typically result in complex coacervation, a form of associative phase separation where one phase has a higher concentration of both polymers and the other phase a lower concentration.

This thesis focuses on the scenario where only one polymer carries electric charge. This situation often occurs for aqueous mixtures of polysaccharides (neutral polymer) and proteins (polyelectrolyte) but has received little attention in literature. The water–water interface that is formed upon phase separation is the main subject of this thesis, but the phase behavior and the formation of water-in-water emulsions are also explored. The system under investigation consists of the biopolymers dextran and gelatin in aqueous solution. Dextran is a branched polysaccharide and gelatin a protein with a pH-adjustable charge. In order to avoid gelation, a special nongelling type of gelatin is used, produced from the collagen of coldwater fish. Both polymers have a molar mass of approximately 100 kDa.

In Chapter 2 it is demonstrated that the presence of charge on one of the polymers results in an electric potential difference between the two phases. Upon phase separation, the polyelectrolyte is confined in majority to one of the phases. Although

small ions can equilibrate freely between the phases, the restriction of macroscopic charge neutrality in each phase dictates that the ion concentrations of the two phases must be different when the system is in thermodynamic equilibrium. This is the so-called Donnan equilibrium, and the ensuing electric potential difference is called the Donnan potential. Its magnitude is proportional to the number of charges of the polyelectrolyte and to the concentration difference of polyelectrolyte between the two phases, and it is inversely proportional to the concentration of background salt. Chapter 2 additionally reveals that the critical demixing concentration of the polymers increases with polyelectrolyte charge and decreases with background salt.

The effect of polyelectrolyte charge and background salt on the critical demixing concentration is explored in more detail in Chapter 3, where the phase behavior is studied experimentally and theoretically. The theory extends the blob model, normally used to describe solutions of two neutral polymers, to incorporate the effects of charge. The charge of one of the polymers is modeled by including the free energy of ions, which are assumed to behave ideally. The differences in the concentrations of ions that result from phase separation are not only responsible for the Donnan potential, but are also entropically unfavorable. A higher polyelectrolyte charge leads to a greater entropic penalty for the ions upon phase separation, which leads to a higher critical demixing concentration. Conversely, addition of salt reduces the relative differences in ion concentrations, which leads to demixing at lower concentrations. An increased polyelectrolyte charge also leads to a higher concentration of solvent in the polyelectrolyte-rich phase.

A consequence of the electric potential difference between the two phases is the formation of an electric double layer at the water–water interface. The influence of the Donnan potential on the interfacial tension, through the electric double layer, is the subject of Chapter 4. Comparisons between the interfacial tension at different polyelectrolyte charges are made for systems with the same degree of phase separation (equal tie-line length). Otherwise, if one would simply compare systems at the same overall polymer concentrations, any change in the tension would be obscured by the different critical demixing concentrations. The interfacial electric double layer forms spontaneously, and its negative free energy represents a negative contribution to the tension of the water–water interface. In experiments, the interfacial tension—in the range of 0.01 to 10 μN/m—is found to decrease up to 50 % on increasing polyelectrolyte charge.

Poisson–Boltzmann theory is used to derive an expression for the decrease in the interfacial tension as a function of the Donnan potential. The theory allows the electrostatic contribution to be deducted from the experimentally measured interfacial tensions, yielding an "intrinsic" interfacial tension that is independent of polyelec-

trolyte charge and set only by the degree of phase separation, despite different overall polymer concentrations. The intrinsic interfacial tension scales with a power of ~3 with the degree of phase separation. Both the magnitude and the scaling of the intrinsic interfacial tension are in agreement with mean-field calculations using the blob model. The calculations also shed light on the structure of the water–water interface, which is shown to be enriched in solvent and to have a typical width of the order of 10 nm.

The physics of the water–water interface is key to the formulation of water-in-water emulsions, the topic of Chapter 5. Because of the width of the interface, surfactant molecules do not straddle the whole interfacial zone and are considered to be unsuitable for stabilizing water-in-water emulsions. Another method, referred to as Pickering stabilization, is to stabilize emulsions through the adsorption of colloidal particles, preventing droplet coalescence. Colloidal adsorption is driven by the tension of the water–water interface, but since this tension is lower by a factor of 10^3 to 10^6 compared to a typical oil–water interface, the adsorption of colloidal particles is also weaker by the same factor. This can be compensated through the use of larger particles, but their higher buoyant mass may lead to rapid sedimentation of the emulsion droplets. To circumvent this, water-in-water emulsions are stabilized here using gibbsite nanoplates, which are thin, light weight, and have a relatively large gravitational length, but still block a large area of water–water interface. An additional advantage of plate-like particles is that the blocked interfacial area is insensitive to the contact angle of the interface with the colloidal particle. This results in stronger adsorption of plate-like particles than spherical particles of the same cross section if the contact angle is not exactly 90°.

The work described in this thesis shows that the presence of charge on one polymer in an aqueous solution of two polymers profoundly affects the phase separation and interface between the coexisting phases. These effects are understood from general theory that is also applicable to other mixtures of charged and uncharged polymer. The gathered insight may well help to guide the development of novel technological applications of aqueous demixed polymer solutions.

Samenvatting

Wanneer twee verschillende polymeren samen in water zijn opgelost, treedt er vaak fasescheiding op. Hierbij ontstaat een tweefasensysteem dat typisch voor zo'n 90 % uit water bestaat. Voor het ontwikkelen van diverse technologische toepassingen is het belangrijk dergelijke mengsels beter te begrijpen. Voorbeelden zijn het isoleren van gevoelige biologische materie met behulp van waterige tweefasensystemen, het tegengaan van fasescheiding in mengsels van polysachariden en eiwitten, en het ontwikkelen van emulsies die geen olie bevatten, zogeheten water-in-wateremulsies. Twee polymeren zonder elektrische lading fasescheiden meestal omdat de positieve mengenthalpie niet gecompenseerd wordt door de relatief kleine mengentropie. De fasescheiding die optreedt is segregatief, wat wil zeggen dat de twee fasen elk zijn verrijkt met één van de twee polymeren. Wanneer de twee opgeloste polymeren een tegengestelde elektrische lading hebben, treedt er complex-coarcervatie op vanwege de attractieve elektrostatische interacties. Dit is een vorm van associatieve fasescheiding: de ene fase bevat een hoge concentratie van beide polymeren en de andere fase een lage concentratie.

In dit proefschrift wordt een ander scenario onderzocht, namelijk oplossingen van één elektrisch geladen polymeer en één ongeladen polymeer. Deze situatie komt vaak voor in het geval van mengsels van polysachariden (neutraal polymeer) en eiwitten (polyelektrolyt), maar is weinig bestudeerd. De belangrijkste focus ligt op het water-watergrensvlak dat zich vormt bij het ontmengen, maar ook het fasegedrag en het vormen van water-in-wateremulsies worden verkend. Het systeem dat wordt onderzocht bestaat uit een oplossing van de biopolymeren dextraan en gelatine in water. Dextraan is een vertakte polysacharide; gelatine een eiwit met een lading die van de pH afhangt. Er wordt een speciaal soort gelatine gebruikt die niet geleert; het wordt verkregen uit het collageen van koudwatervissen. Beide polymeren hebben een molaire massa van ongeveer 100 kDa.

In Hoofdstuk 2 wordt aangetoond dat een lading op een van de polymeren als gevolg heeft dat er een elektrisch potentiaalverschil tussen de twee coëxisterende fasen ontstaat. Fasescheiding zorgt er namelijk voor dat het grootste deel van het polyelektrolyt "opgesloten" zit in een van de fasen. Kleine ionen kunnen zich weliswaar vrij tussen de twee fasen bewegen, maar omdat beide fasen elektrisch neutraal moeten zijn en omdat de fasen met elkaar in thermodynamisch evenwicht moeten zijn, is de ionenconcentratie van beide fasen niet gelijk. Het evenwicht dat zich instelt heet het Donnanevenwicht en veroorzaakt een elektrisch potentiaalverschil, genaamd de Donnanpotentiaal. De grootte van deze potentiaal is evenredig met het aantal ladingen op het polyelektrolyt en het concentratieverschil van het polyelektrolyt tussen de twee fasen; het is omgekeerd evenredig met de zoutconcentratie. Het wordt in Hoofdstuk 2 ook duidelijk dat de kritische ontmengconcentratie hoger wordt naarmate het polyelektrolyt meer lading heeft en lager wordt naarmate er zout wordt toegevoegd.

Het fasegedrag wordt in meer detail bestudeerd in Hoofdstuk 3 met experimenten en theorie. Als uitgangspunt voor de theorie wordt het blobmodel gebruikt, dat oplossingen van twee ongeladen polymeren beschrijft. Het effect van lading op een van de polymeren wordt toegevoegd via de vrije energie van de ionen in het systeem, waarvan ideaal gedrag wordt verondersteld. Uit de berekeningen blijkt dat de verschillen in de ionenconcentraties niet alleen verantwoordelijk zijn voor de Donnanpotentiaal, maar dat ze ook entropisch ongunstig zijn. Een hogere polyelektrolytlading maakt deze concentratieverschillen groter, wat entropisch ongunstiger is en zorgt dat het fasescheiden pas bij hogere polymeerconcentraties optreedt. Het toevoegen van zout verlaagt juist de verschillen in de ionenconcentratie en zorgt voor een lagere kritische ontmengconcentratie. Een hogere polyelektrolytlading leidt ook tot een hogere concentratie van het oplosmiddel in de polyelektrolytrijke fase.

Als gevolg van het elektrisch potentiaalverschil tussen de twee fasen vormt zich een elektrische dubbellaag rond het water-watergrensvlak. Wat het effect is van deze elektrische dubbellaag op de grensvlakspanning wordt onderzocht in Hoofdstuk 4. Dit gebeurt door de grensvlakspanning bij verschillende polyelektrolytladingen te vergelijken voor systemen die in dezelfde mate zijn fasegescheiden (gelijk verschil in polymeerconcentratie tussen de coëxisterende fasen). Zou men daarentegen de vergelijking maken bij gelijke globale polymeerconcentraties, dan zou een verandering van de grensvlakspanning lastig waar te nemen zijn vanwege de verschillende kritische ontmengconcentraties. Omdat de elektrische dubbellaag aan het water-watergrensvlak spontaan ontstaat, heeft deze dubbellaag een negatieve vrije energie die geïnterpreteerd kan worden als een negatieve bijdrage aan de grensvlakspanning. In experimenten blijkt dat de grensvlakspanning – die 0,01 tot 10 µN/m bedraagt – met wel 50 % kan afnemen wanneer de lading van het polyelektrolyt wordt verhoogd.

Een uitdrukking voor de afname van de grensvlakspanning als functie van de Donnanpotentiaal wordt afgeleid op basis van Poisson-Boltzmanntheorie. Met behulp van de theorie kan de elektrostatische bijdrage worden afgetrokken van de experimenteel gemeten grensvlakspanning, zodat er een "intrinsieke" grensvlakspanning overblijft die gecompenseerd is voor de vrije energie van de elektrische dubbellaag. Deze intrinsieke grensvlakspanning blijkt onafhankelijk te zijn van de lading van het polyelektrolyt en volledig te worden bepaald door de mate van fasescheiding, ondanks verschillende polymeerconcentraties. De intrinsieke grensvlakspanning schaalt met een macht van ongeveer 3 met de mate waarin het systeem fasegescheiden is. Zowel de grootte als het schaalgedrag van de intrinsieke grensvlakspanning zijn in overeenstemming met berekeningen met het blobmodel. De berekeningen verschaffen ook inzicht in de structuur van het water-watergrensvlak. In het grensvlak blijkt de totale polymeerconcentratie lager te zijn; bovendien blijkt het grensvlak een dikte te hebben van circa 10 nm.

Het begrijpen van de fysica van het water-watergrensvlak is essentieel voor het realiseren van water-in-wateremulsies, het onderwerp van Hoofdstuk 5. Oppervlakte-actieve moleculen zijn in de regel te kort om het water-watergrensvlak geheel te doorkruisen en daardoor ongeschikt voor het stabiliseren van water-in-wateremulsies. Emulsies kunnen ook gestabiliseerd worden door colloïdale deeltjes aan het grensvlak te laten adsorberen waardoor de coalescentie van druppels voorkomen wordt, zogeheten Pickeringstabilisatie. De grensvlakspanning, de drijvende kracht achter deeltjesadsorptie, is bij water-watergrensvlakken 10^3 tot 10^6 keer kleiner dan bij olie-watergrensvlakken; de adsorptie van deeltjes is daardoor evenzoveel zwakker. Dit kan gecompenseerd worden door gebruik van grotere colloïdale deeltjes, maar hun grotere massa kan leiden tot snelle sedimentatie van de emulsiedruppels. Door gebruik te maken van plaatvormige gibbsietdeeltjes kan dit probleem worden omzeild, omdat deze dunne en lichte deeltjes een grote gravitatielengte hebben, maar toch veel water-watergrensvlak afschermen. Een ander voordeel van plaatvormige deeltjes is dat de grootte van het afgeschermde grensvlak niet afhangt van de contacthoek van het grensvlak met het deeltje. Hierdoor is de adsorptie van plaatvormige deeltjes sterker dan van bolvormige deeltjes wanneer de contacthoek niet precies 90° is.

Het onderzoek dat beschreven is in dit proefschrift laat zien dat de elektrische lading van een polymeer in een oplossing van twee polymeren in water een grote invloed heeft op het fasegedrag en het grensvlak tussen de coëxisterende fasen. De effecten zijn te begrijpen met algemene theorie die ook toepasbaar is op andere mengsels van geladen en ongeladen polymeren. Dit is essentieel voor het ontwikkelen van nieuwe technologische toepassingen van ontmengde polymeeroplossingen.

List of Symbols

Modifiers

$x^{\mathrm{p}}, x^{\mathrm{u}}$	x for polyelectrolyte (p) or uncharged polymer (u)
x^{+}, x^{-}	x for cations (+) or anions (−)
x_{α}, x_{β}	x in phase α (polyelectrolyte-rich) or β (neutral polymer-rich)
x_0	global value or optimal profile of x
$\langle x \rangle$	average value of x
$\bar{x}$	bulk value of x

Thermodynamics

F	free energy
f	free energy per volume V in units of $kT, f = F/(VkT)$
p	pressure
S	entropy
s	entropy per $Vk, s = S/(Vk)$
T	absolute temperature
μ_{ϵ}	exchange chemical potential

Constants

F	Faraday constant
g	gravitational acceleration
k	Boltzmann constant
N_{A}	Avogadro constant
R	gas constant

Optical Rotation

l	optical path length

α^{λ_i}	optical rotation at wavelength λ_i
$[\alpha]_k^{\lambda_i}$	specific rotation at wavelength λ_i for compound k
λ	wavelength

Concentrations

c	total monomer concentration (number per unit volume)
c_j	total monomer concentration in j (number per unit volume)
c_j^k	number of chains of polymer k per unit volume in j
Δc^{P}	difference in number of polyelectrolyte chains per unit volume between α and β, $\Delta c^{\mathrm{P}} = c_\alpha^{\mathrm{P}} - c_\beta^{\mathrm{P}}$
c^*	overlap concentration of polymers
c_{crit}	critical monomer concentration, calculated from w_{crit}
$c_j^{\pm}$	concentration of + or − ions in j
c_{s}	background salt concentration
c_{ex}	number of ion pairs transferred from phase α to β divided by total volume

Mass Fractions and Mass Densities

L	tie-line length, $L = \sqrt{(w_\alpha^{\mathrm{P}} - w_\beta^{\mathrm{P}})^2 + (w_\alpha^{\mathrm{u}} - w_\beta^{\mathrm{u}})^2}$
w	mass fraction
w_j	total polymer mass fraction in j, calculated using Equation (C.2) from c_j
w_j^k	mass fraction of polymer k in j, calculated as $w_j x_j$
w_{crit}	experimental critical mass fraction of phase separation close to the isoelectric point ($z \approx 0$)
Δw	$w_\alpha - w_\beta$, difference in total polymer mass fractions between α and β
$\Delta\rho$	mass density difference between the two coexisting phases
ρ_{polymer}	mass density of polymer (mass per unit volume)
ρ_{solvent}	mass density of solvent (mass per unit volume)

Amount of Substance

N_j^i	number of ions of type i in j
n^k	total number of moles of polymer chains k
n_j^k	number of moles of polymer chains k in j
x_j	mole fraction of polyelectrolyte in j, $x_j = n_j^{\mathrm{P}}/(n_j^{\mathrm{P}} + n_j^{\mathrm{u}})$
η^{P}	fraction of total amount of polyelectrolyte residing in phase α, $\eta^{\mathrm{P}} = n_\alpha^{\mathrm{P}}/n^{\mathrm{P}}$

Polymeric Properties

$M_{\mathrm{w,monomer}}$	molar mass of monomer
$M_{\mathrm{w,polymer}}$	molar mass of polymer
N	degree of polymerization
R_{g}	radius of gyration

Blob Model

K	constant related to free energy of mixing within a blob [56]
N_{b}	number of blobs per polymer chain
u	interaction parameter between polyelectrolyte and neutral polymer in units of kT
u_{crit}	interaction parameter at c_{crit}; fit parameter
ϵ	measure for deviation of local monomer concentration $c(z)$ from bulk concentration $\bar{c}$, $c(z) \equiv \bar{c}[1 + \bar{u}\epsilon(z)]$
η	composition variable, $\phi(z) \equiv [1 + \eta(z)]/2$
θ	relative volume of polyelectrolyte-rich phase, $\theta = V_\alpha/V$
ν	scaling parameter [56]
ξ	blob size
ϕ	volume fraction of polyelectrolyte blobs
χ	scaling parameter [56]
ω	rescaled interaction parameter, $\omega \equiv \bar{N}_{\mathrm{b}}\bar{u}$

Length, Area, and Volume

A	area
D_{h}	hydrodynamic (Stokes) diameter
D_∞	thickness of the interface for infinite N in absence of solvent, $D_\infty \equiv \bar{\xi}/\sqrt{6\bar{u}}$
d	spherical particle: diameter; plate-like particle: equivalent circular diameter
l	thickness
V	volume
x, y, z	cartesian coordinates
x	dimensionless distance to interface, $x \equiv z/D_\infty$
Z	dimensionless distance to interface, $Z = \kappa z$

Interfacial Tension

E	total interfacial energy of a liquid–liquid interface with an adsorbed particle

E_g	gravitational energy of the liquid–liquid interface
ΔE_{ads}	adsorption energy of a particle at a liquid–liquid interface
f_j	free energy of electric double layer in phase j per unit area
h	contact height of interface at wall with respect to flat interface far from wall
l_c	capillary length, $l_c \equiv \sqrt{\gamma/(\Delta\rho g)}$
Γ	relative change of interfacial tension due to solvent accumulation, $\Gamma \equiv (1-\Delta_1-\bar{u}\Delta_2)/(1-\Delta_1)$
γ	interfacial tension
$\Delta\gamma$	change in interfacial tension due to interfacial electric potential difference
Δ_1	contribution to interfacial tension due to compositional profile (i.e., $\phi(z)$)
Δ_2	contribution to interfacial tension due to concentration profile (i.e., $c(z)$)
θ	contact angle

Electrostatics

e	positive elementary charge
y	reduced electric potential, $y = \exp\Psi$
z	number of charges on polyelectrolyte chain
ϵ	relative permittivity
ϵ_0	permittivity of vacuum
κ^{-1}	Debye screening length, $\kappa \equiv \sqrt{8\pi\lambda_B c_s}$
λ_B	Bjerrum length, $\lambda_B \equiv e^2/(4\pi\epsilon\epsilon_0 kT)$
ρ	local charge density, $\rho(z) \equiv e[c^+(z)-c^-(z)]$
σ	number of charges per unit area in double layer, $\sigma = \int \rho(z)\,\mathrm{d}z$
Ψ	dimensionless electric potential, $\Psi = e\psi/(kT)$
Ψ^∞, Ψ^0	dimensionless electric potential far from the interface and at the interface
Ψ_D	dimensionless Donnan potential difference between two phases, $\Psi_D = \Psi_\alpha - \Psi_\beta$
ψ	electric potential
ω	relative difference in salt concentration and permittivity between two phases, $\omega \equiv \sqrt{(c_{s,\alpha}\epsilon_\alpha)/(c_{s,\beta}\epsilon_\beta)}$

Bibliography

1. M. W. Beijerinck, *Zentralbl. Bakteriol., Parasitenkd. Infektionskrankh.* **22**, 697–699 (1896).
2. P. J. Flory, *Principles of Polymer Chemistry* (Cornell University Press, Ithaca, NY, 1953).
3. V. Y. Grinberg, V. B. Tolstoguzov, G. L. Slonimskii, *Vysokomol. Soedin., Ser. A* **12**, 1593–1599 (1970).
4. R. H. Tromp, A. R. Rennie, R. A. L. Jones, *Macromolecules* **28**, 4129–4138 (1995).
5. M. W. Edelman, E. van der Linden, E. H. A. de Hoog, R. H. Tromp, *Biomacromolecules* **2**, 1148–1154 (2001).
6. M. W. Edelman, R. H. Tromp, E. van der Linden, *Phys. Rev. E* **67**, 021404 (2003).
7. J. Ryden, P.-Å. Albertsson, *J. Colloid Interface Sci.* **37**, 219–222 (1971).
8. D. Forciniti, C. K. Hall, M. R. Kula, *Fluid Phase Equilib.* **61**, 243–262 (1991).
9. M. W. Edelman, E. van der Linden, R. H. Tromp, *Macromolecules* **36**, 7783–7790 (2003).
10. S. Guido, M. Simeone, A. Alfani, *Carbohydr. Polym.* **48**, 143–152 (2002).
11. K. Bergfeldt, L. Piculell, F. Tjerneld, *Macromolecules* **28**, 3360–3370 (1995).
12. P.-Å. Albertsson, *Nature* **182**, 709–711 (1958).
13. V. Y. Grinberg, V. B. Tolstoguzov, *Carbohyd. Res.* **25**, 313–321 (1972).
14. C. M. Durrani, D. A. Prystupa, A. M. Donald, A. H. Clark, *Macromolecules* **26**, 981–987 (1993).

15. V. Y. Grinberg, V. B. Tolstoguzov, *Food Hydrocolloid.* **11**, 145–158 (1997).
16. L. Piculell, B. Lindman, *Adv. Colloid Interfac.* **41**, 149–178 (1992).
17. K. Bergfeldt, L. Piculell, P. Linse, *J. Phys. Chem.* **100**, 3680–3687 (1996).
18. H. G. Bungenberg de Jong, H. R. Kruyt, *Proc. K. Ned. Akad. Wet.* **32**, 849–856 (1929).
19. V. B. Tolstoguzov, *Food Hydrocolloid.* **17**, 1–23 (2003).
20. Y. Song, H. C. Shum, *Langmuir* **28**, 12054–12059 (2012).
21. S. Hardt, T. Hahn, *Lab Chip* **12**, 434–442 (2012).
22. I. Ziemecka, V. van Steijn, G. J. M. Koper, M. T. Kreutzer, J. H. van Esch, *Soft Matter* **7**, 9878 (2011).
23. S. D. Geschiere, I. Ziemecka, V. van Steijn, G. J. M. Koper, J. H. van Esch, M. T. Kreutzer, *Biomicrofluidics* **6**, 022007 (2012).
24. I. Ziemecka, V. van Steijn, G. J. M. Koper, M. Rosso, A. M. Brizard, J. H. van Esch, M. T. Kreutzer, *Lab Chip* **11**, 620–624 (2011).
25. D. Broseta, L. Leibler, L. O. Kaddour, C. Strazielle, *J. Chem. Phys.* **87**, 7248 (1987).
26. R. H. Tromp, M. Vis, B. H. Erné, E. M. Blokhuis, *J. Phys.: Condens. Matter* **26**, 464101 (2014).
27. L. De Ruiter, H. G. Bungenberg de Jong, *Proc. K. Ned. Akad. Wet.* **50**, 836–848 (1947).
28. V. G. Langhammer, L. Nestler, *Makromol. Chem.* **88**, 179–187 (1965).
29. D. Forciniti, C. K. Hall, M. R. Kula, *J. Biotechnol.* **16**, 279–296 (1990).
30. P. Ding, B. Wolf, W. J. Frith, A. H. Clark, I. T. Norton, A. W. Pacek, *J. Colloid Interface Sci.* **253**, 367–376 (2002).
31. E. Scholten, R. Tuinier, R. H. Tromp, H. N. W. Lekkerkerker, *Langmuir* **18**, 2234–2238 (2002).
32. R. H. Tromp, E. M. Blokhuis, *Macromolecules* **46**, 3639–3647 (2013).
33. W. Ramsden, *Proc. R. Soc. London* **72**, 156–164 (1903).
34. S. U. Pickering, *J. Chem. Soc. Trans.* **91**, 2001–2021 (1907).
35. R. Reitherman, S. D. Flanagan, S. H. Barondes, *Biochim. Biophys. Acta* **297**, 193–202 (1973).
36. D. E. Brooks, K. A. Sharp, S. Bamberger, C. H. Tamblyn, G. V. F. Seaman, H. Walter, *J. Colloid Interface Sci.* **102**, 1–13 (1984).

37. C. A. Haynes, J. Carson, H. W. Blanch, J. M. Prausnitz, *AIChE J.* **37**, 1401–1409 (1991).
38. A. Pfennig, A. Schwerin, *Fluid Phase Equilib.* **108**, 305–315 (1995).
39. F. G. Donnan, *Z. Elektrochem. Angew. Phys. Chem.* **17**, 572–581 (1911).
40. F. G. Donnan, *Chem. Rev.* **1**, 73–90 (1924).
41. A. P. Philipse, A. Vrij, *J. Phys.: Condens. Matter* **23**, 194106 (2011).
42. M. B. Perrau, I. Iliopoulos, R. Audebert, *Polymer* **30**, 2112–2117 (1989).
43. K. Bergfeldt, L. Piculell, *J. Phys. Chem.* **100**, 5935–5940 (1996).
44. D. J. Burgess, J. E. Carless, *J. Colloid Interface Sci.* **98**, 1–8 (1984).
45. J. T. G. Overbeek, *J. Colloid Sci.* **8**, 593–605 (1953).
46. J. T. G. Overbeek, *Prog. Biophys. Biophys. Chem.* **6**, 58–84 (1956).
47. M. Djabourov, J. Leblond, P. Papon, *J. Phys. France* **49**, 319–332 (1988).
48. S. Kasapis, E. R. Morris, I. T. Norton, M. J. Gidley, *Carbohydr. Polym.* **21**, 249–259 (1993).
49. L. G. Longsworth, *J. Am. Chem. Soc.* **54**, 2741–2758 (1932).
50. P. H. Barry, J. W. Lynch, *J. Membr. Biol.* **121**, 101–117 (1991).
51. M. Rasa, B. H. Erné, B. Zoetekouw, R. van Roij, A. P. Philipse, *J. Phys.: Condens. Matter* **17**, 2293–2314 (2005).
52. M. Vis, V. F. D. Peters, R. H. Tromp, B. H. Erné, *Langmuir* **30**, 5755–5762 (2014).
53. J. T. G. Overbeek, M. J. Voorn, *J. Cell Compar. Physiol.* **49**, 7–26 (1957).
54. I. Michaeli, M. J. Voorn, J. T. G. Overbeek, *J. Polym. Sci.* **23**, 443–450 (1957).
55. D. J. Burgess, *J. Colloid Interface Sci.* **140**, 227–238 (1990).
56. D. Broseta, L. Leibler, J. F. Joanny, *Macromolecules* **20**, 1935–1943 (1987).
57. D. Broseta, L. Leibler, A. Lapp, C. Strazielle, *Europhys. Lett.* **2**, 733–737 (1986).
58. K. A. Granath, *J. Colloid Sci.* **13**, 308–328 (1958).
59. D. R. Lide, Ed., *CRC Handbook of Chemistry and Physics* (CRC Press/Taylor and Francis, Boca Raton, FL, 90th Edition, 2009).
60. R. H. Tromp, E. ten Grotenhuis, C. Olieman, *Food Hydrocolloid.* **16**, 235–239 (2002).
61. Gelatin Manufacturers Institute of America, *Gelatin Handbook*, `http://www.gelatin-gmia.com/images/GMIA_Gelatin_Manual_2012.pdf`.
62. B.-S. Chiou, R. J. Avena-Bustillos, J. Shey, E. Yee, P. J. Bechtel, S. H. Imam, G. M. Glenn, W. J. Orts, *Polymer* **47**, 6379–6386 (2006).

63. M. Gordon, H. A. G. Chermin, R. Koningsveld, *Macromolecules* **2**, 207–210 (1969).
64. T. Odijk, A. C. Houwaart, *J. Polym. Sci. Polym. Phys.* **16**, 627–639 (1978).
65. V. Y. Borue, I. Y. Erukhimovich, *Macromolecules* **21**, 3240–3249 (1988).
66. J. F. Joanny, L. Leibler, *J. Phys. France* **51**, 545–557 (1990).
67. I. A. Nyrkova, A. R. Khokhlov, M. Doi, *Macromolecules* **27**, 4220–4230 (1994).
68. B. Widom, J. S. Rowlinson, *Molecular Theory of Capillarity* (Oxford University Press, Oxford, U.K., 1984).
69. E. J. W. Verwey, J. T. G. Overbeek, *Theory of the Stability of Lyophobic Colloids* (Dover Publications, New York, 1999).
70. J. Frenkel, *Kinetic Theory of Liquids* (Dover Publications, New York, 1955).
71. E. Ruckenstein, R. Krishnan, *J. Colloid Interface Sci.* **76**, 201–211 (1980).
72. H. Ohshima, S. Ohki, *J. Colloid Interface Sci.* **103**, 85–94 (1985).
73. A. G. Volkov, D. W. Deamer, D. L. Tanelian, V. S. Markin, *Prog. Surf. Sci.* **53**, 1–134 (1996).
74. D. G. A. L. Aarts, J. H. van der Wiel, H. N. W. Lekkerkerker, *J. Phys.: Condens. Matter* **15**, S245–S250 (2003).
75. E. Scholten, L. M. C. Sagis, E. van der Linden, *Biomacromolecules* **7**, 2224–2229 (2006).
76. Y. A. Antonov, P. Van Puyvelde, P. Moldenaers, *Biomacromolecules* **5**, 276–283 (2004).
77. G. K. Batchelor, *An Introduction to Fluid Dynamics* (Cambridge University Press, Cambridge, U.K., 2002).
78. S. Bamberger, G. V. F. Seaman, K. A. Sharp, D. E. Brooks, *J. Colloid Interface Sci.* **99**, 194–200 (1984).
79. Y. Liu, R. Lipowsky, R. Dimova, *Langmuir* **28**, 3831–3839 (2012).
80. Y. A. Antonov, P. Van Puyvelde, P. Moldenaers, *Int. J. Biol. Macromol.* **34**, 29–35 (2004).
81. M. Simeone, A. Alfani, S. Guido, *Food Hydrocolloid.* **18**, 463–470 (2004).
82. E. Spruijt, J. Sprakel, M. A. Cohen Stuart, J. van der Gucht, *Soft Matter* **6**, 172–178 (2010).
83. J. Qin, D. Priftis, R. Farina, S. L. Perry, L. Leon, J. Whitmer, K. Hoffmann, M. Tirrell, J. J. de Pablo, *ACS Macro Lett.* **3**, 565–568 (2014).

84. M. Vis, V. F. D. Peters, B. H. Erné, R. H. Tromp, *Macromolecules* **48**, 2819–2828 (2015).

85. B. T. Nguyen, W. Wang, B. R. Saunders, L. Benyahia, T. Nicolai, *Langmuir* **31**, 3605–3611 (2015).

86. M. Vis, V. F. D. Peters, E. M. Blokhuis, H. N. W. Lekkerkerker, B. H. Erné, R. H. Tromp, *Phys. Rev. Lett.* **115**, 078303 (2015).

87. M. Vis, V. F. D. Peters, E. M. Blokhuis, H. N. W. Lekkerkerker, B. H. Erné, R. H. Tromp, *Macromolecules* **48**, 7335–7345 (2015).

88. A. T. Poortinga, *Langmuir* **24**, 1644–1647 (2008).

89. G. Balakrishnan, T. Nicolai, L. Benyahia, D. Durand, *Langmuir* **28**, 5921–5926 (2012).

90. H. Firoozmand, B. S. Murray, E. Dickinson, *Langmuir* **25**, 1300–1305 (2009).

91. B. T. Nguyen, T. Nicolai, L. Benyahia, *Langmuir* **29**, 10658–10664 (2013).

92. D. M. A. Buzza, P. D. I. Fletcher, T. K. Georgiou, N. Ghasdian, *Langmuir* **29**, 14804–14814 (2013).

93. K. A. Vaynberg, N. J. Wagner, R. Sharma, *Biomacromolecules* **1**, 466–472 (2000).

94. A. M. Wierenga, T. A. J. Lenstra, A. P. Philipse, *Colloid. Surface. A* **134**, 359–371 (1998).

95. F. M. van der Kooij, K. Kassapidou, H. N. W. Lekkerkerker, *Nature* **406**, 868–871 (2000).

96. D. van der Beek, H. N. W. Lekkerkerker, *Langmuir* **20**, 8582–8586 (2004).

97. J. E. G. J. Wijnhoven, *J. Colloid Interface Sci.* **292**, 403–409 (2005).

98. A. A. Verhoeff, R. P. Brand, H. N. W. Lekkerkerker, *Mol. Phys.* **109**, 1363–1371 (2011).

99. M. Vis, H. H. Wensink, H. N. W. Lekkerkerker, D. Kleshchanok, *Mol. Phys.* **113**, 1053–1060 (2015).

100. G. Soligno, M. Dijkstra, R. van Roij, *J. Chem. Phys.* **141**, 244702 (2014).

101. E. J. van Harten, M.Sc. Thesis, Utrecht University, 2013, `http://dspace.library.uu.nl/handle/1874/286860`.

102. J.-M. Meijer, F. Hagemans, L. Rossi, D. V. Byelov, S. I. R. Castillo, A. Snigirev, I. Snigireva, A. P. Philipse, A. V. Petukhov, *Langmuir* **28**, 7631–7638 (2012).

103. J. J. Cras, C. A. Rowe-Taitt, D. A. Nivens, F. S. Ligler, *Biosens. Bioelectron.* **14**, 683–688 (1999).

104. N. A. Mazer, G. B. Benedek, M. C. Carey, *Biochemistry* **19**, 601–615 (1980).

105. P. Pieranski, *Phys. Rev. Lett.* **45**, 569–572 (1980).

106. E. Vignati, R. Piazza, T. P. Lockhart, *Langmuir* **19**, 6650–6656 (2003).

107. C. C. Berton-Carabin, K. Schroën, *Annu. Rev. Food Sci. Technol.* **6**, 263–297 (2015).

List of Publications

This thesis is based on the following publications:

- M. Vis, V. F. D. Peters, R. H. Tromp, B. H. Erné, *Langmuir* **30**, 5755–5762 (2014). (Chapter 2.)
- R. H. Tromp, M. Vis, B. H. Erné, E. M. Blokhuis, *J. Phys.: Condens. Matter* **26**, 464101 (2014). (Chapters 2 to 4.)
- M. Vis, V. F. D. Peters, B. H. Erné, R. H. Tromp, *Macromolecules* **48**, 2819–2828 (2015). (Chapter 3.)
- M. Vis, V. F. D. Peters, E. M. Blokhuis, H. N. W. Lekkerkerker, B. H. Erné, R. H. Tromp, *Phys. Rev. Lett.* **115**, 078303 (2015). (Chapter 4.)
- M. Vis, V. F. D. Peters, E. M. Blokhuis, H. N. W. Lekkerkerker, B. H. Erné, R. H. Tromp, *Macromolecules* **48**, 7335–7345 (2015). (Chapter 4.)
- M. Vis, J. Opdam, I. S. J. van 't Oor, G. Soligno, R. van Roij, R. H. Tromp, B. H. Erné, *ACS Macro Lett.* **4**, 965–968 (2015)—ACS Editor's Choice. (Chapter 5.)

Other publications by the author:

- A. A. Verhoeff, H. H. Wensink, M. Vis, G. Jackson, H. N. W. Lekkerkerker, *J. Phys. Chem. B* **113**, 13476–13484 (2009).
- N. M. G. Franssen, B. Ensing, M. Hegde, T. J. Dingemans, B. Norder, S. J. Picken, G. O. R. Alberda van Ekenstein, E. R. H. van Eck, J. A. A. W. Elemans, M. Vis, J. N. H. Reek, B. de Bruin, *Chem. Eur. J.* **19**, 11577–11589 (2013).
- M. Vis, H. H. Wensink, H. N. W. Lekkerkerker, D. Kleshchanok, *Mol. Phys.* **113**, 1053–1060 (2015).

Curriculum Vitae

Mark Vis was born on June 28, 1988, in Zeist, The Netherlands. He graduated from Montessori Lyceum Herman Jordan in 2006 and studied Chemistry at Utrecht University. He performed his bachelor's thesis research under supervision of prof. dr. Andries Meijerink and dr. Celso de Mello-Donegá and received his bachelor's degree cum laude in 2009. He conducted his master's thesis research under supervision of dr. Dzina Kleshchanok and prof. dr. Henk Lekkerkerker on the synthesis and phase behavior of silica-coated gibbsite platelets at the Van 't Hoff Laboratory for Physical and Colloid Chemistry. For six months, he did an internship at the University of Gothenburg, Sweden, with prof. dr. Johan Bergenholtz. Mark received his master's degree cum laude at the end of 2011 and was awarded the 2012 Unilever Research Prize.

In 2012, Mark started his PhD studies under supervision of dr. Ben Erné and dr. Hans Tromp, the results of which are described in this thesis. This work was published in several peer-reviewed papers and presented at national and international conferences such as FOM Physics and ECIS. Mark was a member of the Debye PhD committee, representing PhD students and postdocs from the six research groups within the Debye Institute for Nanomaterials Science. Mark cofounded the popular Dutch chemistry weblog Scheikundejongens.nl in 2009 with his classmate Aldo Brinkman and made several appearances on national television with programs such as De Rekenkamer and Kassa.